

國立臺灣大學工學院土木工程學系



碩士論文

Department of Civil Engineering

College of Engineering

National Taiwan University

Master Thesis

利用改良式小波轉換技術進行結構損傷評估

Application of Modified Wavelet Transform for

Damage Assessment of Civil Structure

Using Vibration Measurements

薛 汶

Wen Hsueh

指導教授：羅俊雄 博士

Advisor: Chin-Hsiung Loh, Ph.D.

中華民國 106 年 6 月

June, 2017

國立臺灣大學碩士學位論文
口試委員會審定書

利用改良式小波轉換技術進行結構損傷評估
Application of Modified Wavelet Transform for
Damage Assessment of Civil Structure
Using Vibration Measurements

本論文係薛 汶君 (R04521225) 在國立臺灣大學土木工程學系
碩士班完成之碩士學位論文，於民國 106 年 6 月 14 日承下列考試委員
審查通過及口試及格，特此證明

口試委員：

羅 俊 雄

(指導教授)

呂 良 正

周 中 哲

張 國 鎮

謝 尚 賢

羅俊雄

呂良正

周中哲

張國鎮

謝尚賢

(簽名)

系主任

ACKNOWLEDGEMENT



本研究得以順利完成，首先要感謝恩師 羅俊雄教授的指導與教誨。在研究過程中，老師悉心指導並給予無數的建議、方向與諮詢，提供豐富的學習資源與環境，在學期間更提供機會讓學生到國外參與研討會，和學者交流開拓國際視野，非常感謝恩師的付出與提攜。此外還要感謝呂良正教授、周中哲教授、張國鎮教授在口試期間的指導與建議，使本研究更加完整。

在研究期間，感謝學長黃謝恭、李宗憲、葉乃睿、學姊黃昱婷、學妹郭采蓉、吳瑀心、學弟余以諾、李全富在實驗以及研究上提供協助與解惑。此外感謝同學林佳樺、涂雅瀨以及陳俊達，在這兩年中的鼓勵與扶持，互相幫助並解決學習與研究上的問題。另外感謝同學夏瑄、葉柔伶以及其他同學的陪伴，讓我的研究所生活增添許多歡笑。有了各位學長姐、同學、學弟妹的互相幫助與學習，讓我的研生活趨於豐富完整。

最後萬分感謝一直陪伴著我的家人，父親 薛公堯、母親 邱真鳳以及弟弟薛皓尹，您們的支持與體貼，讓我能無後顧之憂地專心學習與研究。謹以此文獻給您們，願您們與我一同分享這份喜悅與榮耀。

ABSTRACT (IN CHINESE)



對於時變系統的結構健康監測，小波轉換已被廣泛應用於取得局部時間的特徵相關訊息。本研究提出改良式小波轉換技術搭配可調式複數莫萊小波進行結構損傷評估，同時也提供較佳的時頻圖表示及簡化訊號重組。基於小波轉換得到的小波係數，本文介紹七種損傷指標包含：(1) Marginal spectrum, (2) Central frequency, (3) Pseudo-instantaneous frequency, (4) Unwrapped phase, (5) Novelty index, (6) Correlation, (7) Normalized component energy。本研究使用兩組振動台試驗的試體（雙塔鋼構架、三層樓鋼構架）以及兩棟實際結構（花蓮明禮國小、台中中興大學）來進行驗證，由分析結果顯示，本文提出之方法能夠取得結構物全域與局部特徵並有效進行結構損傷評估。

關鍵詞： 結構健康監測、小波轉換、可調式複數莫萊小波、結構損傷評估、結構損傷部位識別

ABSTRACT (IN ENGLISH)



For detecting transient signals and time-varying systems, wavelet transform has been used as a signal pattern recognition method for feature extraction. In this study, dynamic response data of structure using modified complex Morlet wavelet with variable central frequency (MCMW+VCF) is used to establish a time-frequency representation of measurement for modal parameter estimation and system damage identification. The proposed wavelet transform (WT) provides a better representation in generating scalogram than using general wavelet transform, besides, the proposed WT can simplify the choice of wavelet parameters and signal reconstruction. Based on the wavelet coefficients, several damage assessment algorithms will be described, which include: (1) Marginal spectrum, (2) Central frequency, (3) Pseudo-instantaneous frequency, (4) Unwrapped phase, (5) Novelty index, (6) Correlation, and (7) Normalized component energy. Seismic response data collected from two lab experiments, a twin tower steel structure and two 3-story steel structures, under a series of both white noise as well as earthquake excitation back to back will be used to demonstrate the proposed algorithms. Also, two field experiments, seismic response of Mingli elementary school and NCHU Civil & Environmental Engineering Building, will be used for the verification, too. The performance of the proposed algorithms is capable for damage detection and localization.

Keywords: structural health monitoring, wavelet transform, modified complex Morlet wavelet, damage detection, damage localization



CONTENTS



口試委員會審定書	i
ACKNOWLEDGEMENT	ii
ABSTRACT (IN CHINESE)	iii
ABSTRACT (IN ENGLISH)	iv
LIST OF TABLES.....	ix
LIST OF FIGURES.....	x
Chapter 1. Introduction	1
1.1 Background.....	1
1.2 Research objectives.....	4
Chapter 2. Signal Analysis Methodology.....	6
2.1 The Continuous Wavelet Transform.....	6
2.1.1 The Continuous Wavelet Transform	6
2.1.2 The Mother Wavelets	7
2.1.3 Variable Central Frequency.....	9
2.1.4 Edge effect melioration: Signal padding	10
2.1.5 The Parseval Equality and Computation of Wavelet Transform via FFT	11
2.1.6 Example 1 (Simulation).....	11
2.1.7 Example 2 (Experiment).....	12
2.2 The Discrete Wavelet Transform.....	13
2.3 The Wavelet Packet Transform	15
2.4 Hilbert Transform	16



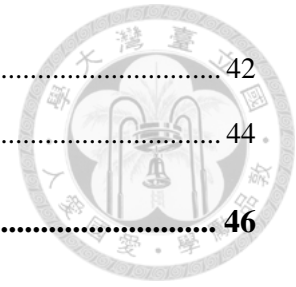
Chapter 3. Damage Assessment Algorithms -Ambient Vibration Data 18

3.1	Damage assessment algorithms	18
3.1.1	Marginal Spectrum	18
3.1.2	Central Frequency	19
3.1.3	Novelty Index (reference-based index)	19
3.1.4	Correlation (reference-based index)	20
3.1.5	Normalized Component Energy	21
3.2	Application to Twin-tower Structure with Weak Bracing System	21
3.2.1	Set-up of monitoring system	21
3.2.2	Pre-processing procedure	23
3.2.3	The Results of Damage Assessment.....	24
3.3	Application to Two Three-story steel frames	27
3.3.1	Set-up of monitoring system	27
3.3.2	Pre-processing procedure	29
3.3.3	The Results of Damage Assessment.....	30
3.4	Chapter Summary	31

Chapter 4. Damage Assessment Algorithms -Earthquake Response Data 34

4.1	Damage assessment algorithms	34
4.1.1	Pseudo-instantaneous Frequency.....	34
4.1.2	Unwrapped Phase	37
4.2	Application to Twin-tower Structure with Weak Bracing System	38
4.2.1	Set-up of monitoring system	38
4.2.2	Pre-processing procedure	38
4.2.3	The Results of Damage Assessment.....	39
4.3	Application to Two Three-story steel frames	41
4.3.1	Set-up of monitoring system	41
4.3.2	Pre-processing procedure	41

4.3.3	The Results of Damage Assessment.....	42
4.4	Chapter Summary	44
Chapter 5. Field Application		46
5.1	Application to Mingli Elementary School	46
5.1.1	Set-up of monitoring system	46
5.1.2	Pre-processing procedure	46
5.1.3	The Results of Damage Assessment.....	47
5.2	Application to NCHU Civil & Environmental Engineering Building	48
5.2.1	Set-up of monitoring system	48
5.2.2	Pre-processing procedure	49
5.2.3	The Results of Damage Assessment.....	50
Chapter 6. Conclusion		52
6.1	Research conclusions.....	53
6.2	Future work.....	56
References		58
Tables		62
Figures		63
Appendix I		112
Appendix II		124
Appendix III.....		136
Appendix IIII		138



LIST OF TABLES



Table 3-1	Test protocol of twin-tower steel structure	62
Table 3-2	Test protocol of two three-story steel frames	62

LIST OF FIGURES



Figure 1-1 The flowchart of the pattern-level feature extraction technique..... 63

Figure 2-1 The shapes of Shannon, Complex Morlet, and Mexican Hat wavelets in time and frequency domain (All the wavelets have the same analysis frequency of 5 Hz) 64

Figure 2-2 The shape of complex Morlet wavelet in different parameters a and b (fixed $\omega_0 = 1$ Hz) with $\sigma = 1$ (top) and $\sigma = 2$ (bottom) in time and frequency domain 64

Figure 2-3 The shape of complex Morlet wavelet in different central frequency (fixed $a = 1$) with $\sigma = 1$ (top) and $\sigma = 1$ (bottom) in time and frequency domain 65

Figure 2-4 The relationship between σ , time duration (top left) and frequency bandwidth (top right). The definition of time duration is $0.95|\psi(t)|$ (bottom left) and frequency bandwidth is $\max(|\psi(\omega)|)/\sqrt{2}$ (bottom right)..... 65

Figure 2-5 Signal padding operation for using $\sigma = 2$ 66

Figure 2-6 The wave form of the simulated nonlinear time functions..... 66

Figure 2-7 Plot time-frequency analysis of the test signal $s(t)$; (a) using general CWT, (b) using MCMW+VCF, (c) the instantaneous frequency using Hilbert transform of original signal $s_1(t)$, $s_2(t)$, and $s_3(t)$ 67



Figure 2-8	One-story two-bay reinforced concrete frame.....	67
Figure 2-9	Dimension of RC frame.....	68
Figure 2-10	The scalogram of RC frame (a) using general CWT, (b) using MCMW+VCF with $\sigma = 1$, (c) using MCMW+VCF with $\sigma = 2$	68
Figure 2-11	The acceleration of RC frame (top) and the ridge calculated from different wavelet transform (bottom)	69
Figure 2-12	Discrete wavelet transform tree.....	69
Figure 2-13	Wavelet packet transform tree	70
Figure 2-14	Wavelet packet transform tree (in Paley order).....	70
Figure 3-1	The twin-tower steel structure	71
Figure 3-2	Damage scenario-1, 2, and 3 of the twin-tower steel structure	71
Figure 3-3	Sensor instrumentations for the twin-tower steel structure	72
Figure 3-4	The maximum interstory drift ratio for twin-tower steel structure.....	72
Figure 3-5	The central frequencies for twin-tower steel structure (w.r.t. frequency band: 0~6 Hz).....	73
Figure 3-6	The central frequencies for twin-tower steel structure (w.r.t. frequency band: 0~10 Hz).....	73
Figure 3-7	The Novelty index for twin-tower steel structure (w.r.t. frequency band: 0~6 Hz)	74



Figure 3-8	The Novelty index for twin-tower steel structure (w.r.t. frequency band: 0~10 Hz)	74
Figure 3-9	The correlation for twin-tower steel structure (w.r.t. frequency band: 0~6 Hz)	75
Figure 3-10	The correlation for twin-tower steel structure (w.r.t. frequency band: 0~10 Hz)	75
Figure 3-11	The normalized CE for twin-tower steel structure (w.r.t. frequency band: 0~6 Hz)	76
Figure 3-12	The normalized CE for twin-tower steel structure (w.r.t. frequency band: 0~10 Hz)	76
Figure 3-13	Two three-story steel frames.....	77
Figure 3-14	Components of each floor for two three-story steel frames	77
Figure 3-15	Configuration of the two three-story steel frames.....	78
Figure 3-16	Sensor instrumentations for the two three-story steel frames.....	78
Figure 3-17	Hysteresis loop of specimen-1	79
Figure 3-18	Hysteresis loop of specimen-2.....	80
Figure 3-19	The maximum interstory drift ratio for two three-story steel frames	81
Figure 3-20	The maximum story drift for specimen-2.....	81

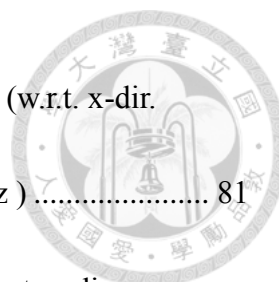


Figure 3-21 The central frequency for two three-story steel frames (w.r.t. x-dir. frequency band: 0~5 Hz, torsional dir. frequency band 25~40 Hz) 81

Figure 3-22 The Novelty index for two three-story steel frames (w.r.t. x-dir. frequency band: 0~5 Hz, torsional dir. frequency band 25~40 Hz) 82

Figure 3-23 The correlation for two three-story steel frames (w.r.t. x-dir. frequency band: 0~5 Hz, torsional dir. frequency band 25~40 Hz) 82

Figure 3-24 The normalized CE for two three-story steel frames (w.r.t. x-dir. frequency band: 0~5 Hz, torsional dir. frequency band 25~40 Hz) 83

Figure 4-1 The analysis frequency band of complex Morlet wavelet..... 84

Figure 4-2 The hysteresis loop for RC frame..... 84

Figure 4-3 The pseudo-IF using different extraction methods..... 85

Figure 4-4 The time history of the simulated nonlinear SDOF system..... 86

Figure 4-5 The hysteresis loop of the simulated nonlinear SDOF system..... 86

Figure 4-6 The pseudo-IF of the simulated nonlinear SDOF system 86

Figure 4-7 The central frequencies for twin-tower steel structure (w.r.t. frequency band: 0~6 Hz) 87

Figure 4-8 The central frequencies for twin-tower steel structure (w.r.t. frequency band: 0~10 Hz) 87

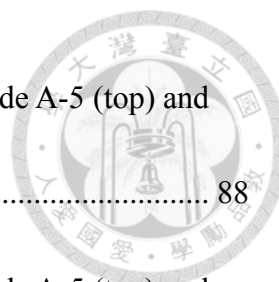


Figure 4-9 The pseudo-IF for damage scenario-1 with sensing node A-5 (top) and sensing node B-4 (bottom) 88

Figure 4-10 The pseudo-IF for damage scenario-2 with sensing node A-5 (top) and sensing node B-4 (bottom) 89

Figure 4-11 The pseudo-IF for damage scenario-3 with sensing node A-5 (top) and sensing node B-4 (bottom) 90

Figure 4-12 The unwrapped phase for damage scenario-1 (w.r.t. frequency band: 0~10 Hz) 91

Figure 4-13 The unwrapped phase for damage scenario-2 (w.r.t. frequency band: 0~10 Hz) 91

Figure 4-14 The unwrapped phase for damage scenario-3 (w.r.t. frequency band: 0~10 Hz) 92

Figure 4-15 The central frequency for two three-story steel frames (w.r.t. x-dir. frequency band: 0~5 Hz, torsional dir. frequency band 0~50 Hz) 92

Figure 4-16 The pseudo-IF for two three-story steel frames in x-dir. with specimen-1 (top) and specimen-2 (bottom) (w.r.t. x-dir. frequency band: 0~5 Hz) 93

Figure 4-17 The pseudo-IF for two three-story steel frames in torsion direction with specimen-1 (top) and specimen-2 (bottom) (w.r.t. torsional dir. frequency band: 25~40 Hz) 93



Figure 4-18 The unwrapped phase for two three-story steel frames in x-dir. with specimen-1 (1st and 3rd row) and specimen-2 (2nd and 4th row) (w.r.t. x-dir. frequency band: 0~5 Hz) 94

Figure 4-19 The unwrapped phase for two three-story steel frames in torsional dir. with specimen-1 (1st and 3rd row) and specimen-2 (2nd and 4th row) (w.r.t. torsional dir. frequency band: 0~50 Hz)..... 95

Figure 5-1 Sensor instrumentations for the Mingli Elementary School..... 96

Figure 5-2 The peak acceleration (PA) of every recorded earthquake event 96

Figure 5-3 The recorded accelerations of basement in y-dir. (top) and x-dir. (bottom) 97

Figure 5-4 The central frequency for the Mingli Elementary School (w.r.t. y-dir. frequency band: 1.5~5 Hz, x-dir. frequency band 1~4 Hz) 98

Figure 5-5 The unwrapped phase for the Mingli Elementary School (w.r.t. y-dir. frequency band: 1.5~5 Hz, x-dir. frequency band 1~4 Hz) 98

Figure 5-6 The pseudo-IF for EV04 (1996/09/05) (w.r.t. frequency band: 0.5~6 Hz for both directions) 99

Figure 5-7 The pseudo-IF for EV05 (1999/09/20) using relative acceleration (w.r.t. frequency band: 0.5~6 Hz for both directions)..... 100

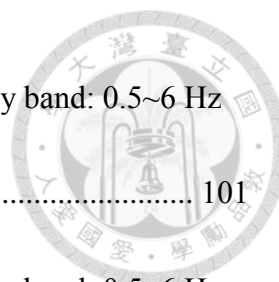


Figure 5-8 The pseudo-IF for EV06 (1999/09/20) (w.r.t. frequency band: 0.5~6 Hz for both directions) 101

Figure 5-9 The pseudo-IF for EV05 (2006/12/26) (w.r.t. frequency band: 0.5~6 Hz for both directions) 102

Figure 5-10 The pseudo-IF for EV05 (2010/10/02) (w.r.t. frequency band: 0.5~6 Hz for both directions) 103

Figure 5-11 Sensor instrumentations for the NCHU Civil & Environmental Engineering Building..... 104

Figure 5-12 The peak ground acceleration (PGA) of every recorded earthquake event 104

Figure 5-13 The recorded accelerations of 1F in x-dir. (top) and y-dir. (bottom).... 105

Figure 5-14 The central frequency for the NCHU Civil & Environmental Engineering Building (w.r.t. frequency band: 1~4 Hz for both direction)..... 106

Figure 5-15 The unwrapped phase for the NCHU Civil & Environmental Engineering Building (w.r.t. frequency band: 1~4 Hz for both direction)..... 106

Figure 5-16 The pseudo-IF for EV09 (1996/03/05) (w.r.t. frequency band: 0.5~6 Hz for both directions) 107

Figure 5-17 The pseudo-IF for EV13 (1999/09/20) using relative acceleration (w.r.t. frequency band: 0.5~6 Hz for both directions)..... 108

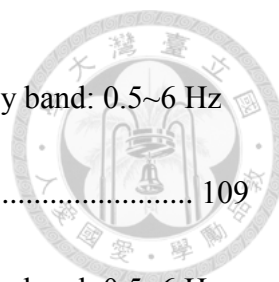


Figure 5-18 The pseudo-IF for EV27 (1999/09/24) (w.r.t. frequency band: 0.5~6 Hz
for both directions) 109

Figure 5-19 The pseudo-IF for EV59 (2006/03/09) (w.r.t. frequency band: 0.5~6 Hz
for both directions) 110

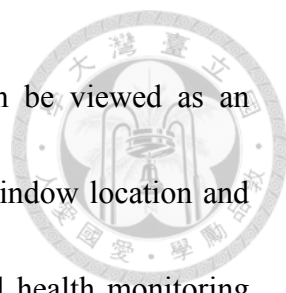
Figure 5-20 The pseudo-IF for EV94 (2009/11/05) (w.r.t. frequency band: 0.5~6 Hz
for both directions) 111

Chapter 1. Introduction




1.1 Background

Structural system identification and damage detection have received more and more attention in the field of civil engineering. Through monitoring data on structures, a quantity of information can be obtained. A well-known classification for damage identification methods can be defined as four levels: (Level-1) Determination or detection that damage is present in the structure; (Level-2) Determination of the geometric location of the damage; (Level-3) Quantification of the severity of the damage; (Level-4) Prediction of the remaining service life of the structure. One of the efficient and accurate damage detection techniques applicable to all types of structural systems is the vibration-based damage detection (VBDD). The vibration characteristics of a structure can be considered to be a global response signature that can be used as the basis for assessing its condition because they contain embedded information about the structure's inherent properties. Changes in the structural condition will be reflected in the vibration signature, which make it possible to identify the presence of damage by tracking changes to that signature. Fourier-based analysis has been used as a means of translating vibration signals from time domain into the frequency domain to detect the vibration signatures. But the Fourier transform is not able to present the time dependency of signals and it cannot capture the time-varying characteristics that are commonly observed in the signals



measured from the vibration of structures. Wavelet transform can be viewed as an extension of the traditional Fourier transform with the adjustable window location and size, which has recently emerged as a promising tool for structural health monitoring (SHM) and damage detection due to its inherent properties. Its widespread use is also due to its availability of fast and accurate computational algorithms for signal transformation and reconstruction.

Early work using wavelet analysis for SHM has been carried out from several perspectives. From a system identification perspective, Basu and Gupta (1997) applied wavelet analysis to obtain the spectral moments and peak structural responses of multi-degree-of-freedom (MDOF) systems subjected to nonstationary seismic excitations. Staszewski (1997) used time-scale decomposition to identify the damping in MDOF systems. Todorovska (2001) used the continuous wavelet transform to estimate the instantaneous frequency of signals. Kijewski and Kareem (2003) used wavelet analysis for system identification. Lardies and Ta (2005) used a wavelet-based approach to estimate the instantaneous frequency, damping, and envelope of the system. Li and Liang (2012) proposed a generalized synchrosqueezing transform to enhance the signal time-frequency representation. Tarinejad and Damadipour (2014) used modified Morlet wavelet to estimate damping. Klepka and Uhl (2014) identified the modal parameters of non-stationary systems with the recursive method based on the wavelet adaptive filter.



Chen et al (2014) detected the sudden stiffness reduction in acceleration time history using discrete wavelet transform. Guo and Kareem (2015) utilized the transformed singular value decomposition in tandem to automate the identification of analysis regions in the time-frequency domain. Subsequently, Laplace wavelet filtering is adopted to extract impulse-type signals from the WT coefficients to estimate the damping from transient nonstationary data. From a signal processing perspective, Robertson et al (2003) used Holder exponent based on the wavelet transform to detect the presence of damage and determine when the damage occurred. Goggins et al (2007) divided wavelet coefficients into several frequency bands and the degree of correlation between coefficients of ground and response acceleration was evaluated and allowed yielding and buckling events to be detected. Nair and Kiremidjian (2009) use a wavelet energy based approach to detect the damage. Noh et al (2011) use wavelet-based damage-sensitive features (DSFs) extracted from structural responses recorded during earthquakes to diagnose structural damage. Lee et al (2014) proposed a continuous relative wavelet entropy-based reference-free damage detection algorithm for truss bridge structures and showed that it was sensitive to slight damage extent for the tested damage type (i.e. loosening of bolts). Balafas and Kiremidjian (2015) developed and validated a novel earthquake damage estimation scheme based on the continuous wavelet transform of input and output acceleration measurements. Amezcuita-Sanchez and Adeli (2015) used

the synchrosqueezed wavelet transform fractality model to detect, locate, and quantify the damage in smart high-rise building structures.



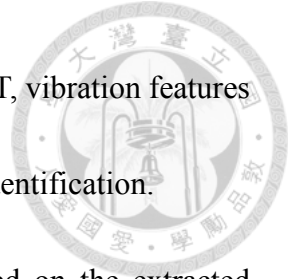
1.2 Research objectives

The objective of this study is to utilize the pattern-level feature extraction technique through the continuous wavelet transform (CWT) with the proposed modified complex Morlet wavelet with variable central frequency (MCMW+VCF) to decompose the vibration responses into wavelet coefficient distribution as a joint function of time and frequency. The flowchart of the pattern-level feature extraction technique is shown in **Figure 1-1**. Different from centralized feature extraction, pattern-level feature extraction technique uses response measurement from individual sensing node. Then based on the extracted features, several damage assessment techniques can be implemented using the pattern-level fusion techniques.

The organization of this study is briefly described as follows:

Chapter 1: A brief description of the research background and the literature survey on the existing identification techniques based on the wavelet transform is presented. Then a general introduce to the objective and scope of this research.

Chapter 2: Introduce the wavelet analysis including the continuous wavelet transform (CWT), discrete wavelet transform (DWT), and wavelet packet transform (WPT). More



details of the CWT will also be described. By making use of the CWT, vibration features of structure can be extracted and then applied to structural damage identification.

Chapter 3: In this chapter, 5 damage assessment algorithms based on the extracted features will be described, which include: (1) Marginal spectrum, (2) Central frequency, (3) Novelty index, (4) Correlation and (5) Normalized component energy. Response measurement from two lab experiments will be firstly introduced then used to validate the proposed methods.

Chapter 4: Based on the features extracted from earthquake response data, 4 algorithms can be used to identify the damage, which include: (1) Marginal spectrum, (2) Central frequency, (3) Pseudo-instantaneous frequency, and (4) Unwrapped phase. Also, the same two experiments from shaking table tests that have been introduced in chapter 3 will be utilized to verify the algorithms.

Chapter. 5: The earthquake response data collected from two building structures under earthquake excitation will be used to verify the proposed methods.

Chapter. 6: Discussion and conclusion for the use of the proposed methods will be given. The future work of this topic will also be indicated.

Chapter 2. Signal Analysis Methodology



2.1 The Continuous Wavelet Transform

2.1.1 The Continuous Wavelet Transform

The continuous wavelet transform (CWT) is a linear transformation, represents the signal $x(t)$ as a sum of dilated and time-shifted wavelets in the form:

$$W_{\psi}[x](b, a) = \int_{-\infty}^{\infty} x(t)\psi_{(b,a)}^*(t)dt \quad (2.1.1)$$

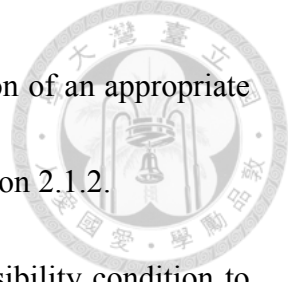
$$\psi_{(b,a)}^*(t) = \frac{1}{\sqrt{a}}\psi^*\left(\frac{t-b}{a}\right) \quad (2.1.2)$$

in which $\psi(t) \in L^2(\mathfrak{R})$ is called the mother wavelet and $*$ represents a complex conjugate.

The mother wavelet $\psi(t)$ is dilated by various a , which are the scale parameters defining the analysis window stretching, and shifted parameters b , which localize the wavelet function in the time domain. The factor $a^{-1/2}$ is used to ensure energy preservation.

These basic functions are convoluted with $x(t)$ to compute the wavelet coefficients $W_{\psi}[x](b, a)$. By this approach, one can examine the signal at different time window and frequency band by controlling the wavelet's translation and dilatation. The higher the value of wavelet coefficient, the more similar the wavelet basis is to the original signal.

One can observe the variation of wavelet coefficients from the scalogram, which take the modulus of wavelet coefficients and show in time-scale plane with different color patterns to represent different intensities of the modulus. It should be mention that different mother



wavelet will provide different result of CWT. Therefore, the selection of an appropriate mother wavelet is an important issue which will be discussed in section 2.1.2.

The mother wavelet $\psi(t)$ should satisfied the following admissibility condition to ensure existence of the inverse wavelet transform such as

$$W_{\psi} = \int_0^{\infty} \frac{|\hat{\psi}(\omega)|^2}{|\omega|} d\omega < +\infty \quad (2.1.3)$$

where $\hat{\psi}(\omega)$ is the Fourier transform of $\psi(t)$. The existence of the integral in equation (2.1.3) requires that

$$\hat{\psi}(0) = 0 \quad , \text{ i.e., } \int_{-\infty}^{\infty} \psi(t) dt = 0 \quad (2.1.4)$$

The signal $x(t)$ can be reconstructed by an inverse wavelet transform of $W_{\psi}[x](b, a)$ as defined by

$$x(t) = \frac{1}{W_{\psi}} \int_{a=-\infty}^{\infty} \int_{b=0}^{\infty} W_{\psi}[x](b, a) \psi_{(b,a)}(t) \frac{1}{a^2} db da \quad (2.1.5)$$

2.1.2 The Mother Wavelets

There are countless mother wavelets used in practice for CWT. The wavelet analysis with real wavelet function like Mexican Hat unveils discontinuities or isolated peaks in the signal. For those who want to observe the phase variation, an analytical wavelet like the complex Morlet and Shannon can satisfy such requirement [6]. The scaling function does not exist in this class of wavelet so the DWT and fast algorithm is not available. But



the infinite regularity permits an exact reconstruction.

Figure 2-1 shows the comparison between these three wavelets. All the wavelets have the same center frequency of 5 Hz. The result reveals that the Mexican Hat is simple zero phase wavelet, the complex Morlet wavelet has side lobes on both sides, and the Shannon wavelet is a leggy wavelet with a number of side lobes that die out on both sides. One might suspect that the Morlet and Shannon wavelets will have somewhat lower temporal resolution due to their side lobes, in contrast to the Mexican Hat wavelet which should exhibit higher temporal resolution. But in Fourier Transform, Mexican Hat shows worse frequency resolution than other two's and the complex Morlet wavelet shows best shape which matches the sharp peaks of signal in frequency domain. Therefore, for this data processing, the modified complex Morlet wavelet (MCMW) is used as the mother wavelet. The MCMW is defined as:

$$\psi(t) = e^{i\omega_0 t} e^{-(t^2/2\sigma^2)} \quad (2.1.6)$$

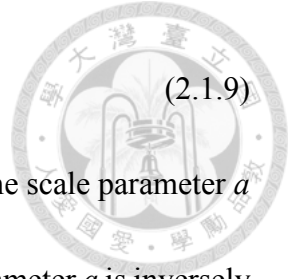
which is essentially a complex exponential modulated by a Gaussian envelope and σ is a measure of the spread in time.

The MCMW has Fourier transform

$$\hat{\psi}(\omega) = \sqrt{2\pi}\sigma e^{-\frac{1}{2}(\omega-\omega_0)^2\sigma^2} \quad (2.1.7)$$

The scaled wavelet and its Fourier Transform are

$$\psi_{(b,a)}^*(t) = \frac{1}{\sqrt{a}} e^{i\omega_0(\frac{t-b}{a})} e^{-\frac{(\frac{t-b}{a})^2}{2\sigma^2}} \quad (2.1.8)$$



$$\psi_{(b,a)}^*(\omega) = e^{-i\omega b} \hat{\psi}(a\omega) \quad (2.1.9)$$

For the Morlet wavelet, there is a unique relationship between the scale parameter a and Fourier frequency ω , at which the wavelet is focus. The scale parameter a is inversely proportional to frequency ω

$$a = \frac{\omega_0}{\omega} \quad (2.1.10)$$

Figure 2-2 shows the relationship between scale parameters a and analysis frequencies ω for using central frequency $\omega_0 = 1$ Hz and also take into consider the σ term for choosing $\sigma = 1$ and 2. From the Figure, we can see the uncertainty principle of signal processing. As the scale parameter $a < 1$ ($\omega > \omega_0$), it shows that an increase in time resolution results in a decrease in frequency resolution, and vice versa. For the modified Morlet wavelet ($\sigma = 2$), it enhances the frequency resolution at the expense of time resolution.

2.1.3 Variable Central Frequency

Facing the uncertainty principle of signal processing, we change the general way of choosing different scales ($\omega_0 = \text{const.}$) but to choose different central frequency ($a = \text{const.}$) through the analysis frequencies.

$$a = \frac{\omega_0}{\omega} = 1 \quad (2.1.11)$$

Using this method, we can keep the resolution the same and change the coefficients

from time-scale analysis to time-frequency analysis:

$$W_{\psi}[x](b, \omega = \omega_0) = \int_{-\infty}^{\infty} x(t) \psi_{(b, \omega)}^*(t) dt \quad (2.1.12)$$



Figure 2-3 shows the proposed variable central frequencies under $\sigma = 1$ and 2. Compare with **Figure 2-2**, the resolution remain the same through the analysis frequency for using proposed variable central frequency. And **Figure 2-4** shows the relationship between σ , time duration and frequency bandwidth under $a = 1$. We can see that if we choose larger σ , the time duration gets longer and the frequency bandwidth becomes narrower which will provide smoother wavelet spectrum in time-axis and sharper spectrum in frequency-axis, and vice versa. It is optional for the user to choose proper σ , for example, if we care more about the frequency domain than time domain like white noise data, we can choose larger sigma.

2.1.4 Edge effect melioration: Signal padding

The loss of considerable regions of a signal is the unfortunate consequence of edge effects. One possible solution to this problem is padding the beginning and end of the signal with real signal and leaving these values at the both sides to be corrupted by edge effect. Using this method, the characteristics of the signal can be preserved [11]. **Figure 2-5** shows an example of signal padding operation for using $\sigma = 2$. From **Figure 2-4**, we know the time duration of the Morlet wavelet is 9.8 seconds under $\sigma = 2$, so we



reflect a portion of the signal (4.9 seconds) about its beginning and end to compute the wavelet coefficients.

2.1.5 The Parseval Equality and Computation of Wavelet Transform via FFT

The Parseval equality for the inner product of two functions f and g is [22]

$$\int_{-\infty}^{\infty} f(t)g(t)dt = \frac{1}{2\pi} \int_{-\infty}^{\infty} \hat{f}(\omega)\hat{g}(\omega)d\omega \quad (2.1.13)$$

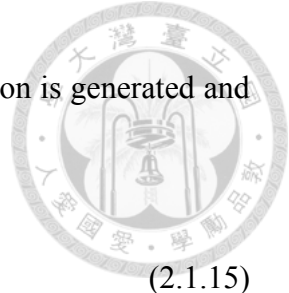
and it implies

$$\begin{aligned} W_{\psi}[x](b, a) &= \int_{-\infty}^{\infty} x(t)\psi_{(b,a)}^*(t)dt \\ &= \frac{1}{2\pi} \int_{-\infty}^{\infty} \hat{f}(\omega)\hat{\psi}_{(b,a)}^*(\omega)d\omega \\ &= \frac{1}{2\pi} \int_{-\infty}^{\infty} \hat{f}(\omega)\hat{\psi}^*(a\omega)e^{i\omega b}d\omega \\ &= FT^{-1}\{\hat{f}(\omega)\hat{\psi}^*(a\omega)\} \end{aligned} \quad (2.1.14)$$

Then general $W_{\psi}[x](b, a)$ can be computed efficiently using Fourier Transform by first computing $\hat{f}(\omega)$ and $\hat{\psi}^*(a\omega)$, and then computing the inverse transform of the product $\hat{f}(\omega)\hat{\psi}^*(a\omega)$. The proposed $W_{\psi}[x](b, \omega)$ can also be computed via the same approach.

2.1.6 Example 1 (Simulation)

To verify the successful implementation of modified complex Morlet wavelet with



variable central frequencies (MCMW+VCF), a nonlinear time function is generated and shown in **Figure 2-6** [21]:

$$s(t) = s_1(t) + s_2(t) + s_3(t) \quad (2.1.15)$$

where

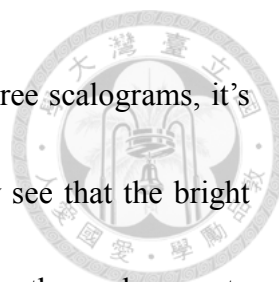
$$\begin{aligned} s_1(t) &= (1 + 0.2 \cos(2t)) \cos(2\pi(2t + 0.3 \cos(t))) \\ s_2(t) &= (1 + 0.3 \cos(2t)) e^{-t/15} \cos(2\pi(2.4t + 0.5t^{1.2} + 0.3 \sin(t))) \\ s_3(t) &= \cos(2\pi(5.3t + 0.2t^{1.3})) \end{aligned}$$

Application of the general CWT and the proposed MCMW+VCF to the nonlinear time function, **Figure 2-7** shows the modulus of wavelet coefficients from these two methods in scalogram and the instantaneous frequency (IF) using Hilbert transform of the signals is also shown. We can see that using general CWT, the time resolutions are poor in lower frequencies, but using variable central frequencies, we can fix the resolution and provide better time-frequency representation.

2.1.7 Example 2 (Experiment)

The proposed method is also applied to the shaking table test of a SDOF RC frame [4]. The test specimen was a one-story two-bay frame (**Figure 2-8**) with overall height of 2 m and an approximate weight of 6454 kg, the dimension of the frame is shown in **Figure 2-9**. Take the average of the measurements from accelerometers A1, A4, and A7.

The results of the acceleration using general CWT and the proposed method using



different sigma ($\sigma = 1, 2$) are shown in **Figure 2-10**. From these three scalograms, it's hard to compare the pros and cons of the two methods, it can only see that the bright regions under $\sigma = 2$ are sharper and longer than other two. Using the scalogram to extract the ridge as instantaneous frequency (**Figure 2-11**), which will be describe in section 4.1.1, we can see that the general CWT provide poorer instantaneous frequency in the initial small amplitude data because the energy preservation factor $a^{-1/2}$ provides larger weight for the analysis frequencies which are smaller than central frequency, it may also enlarge the frequency given by earthquake. And the difference between using sigma equals to 1 and 2 is that $\sigma = 2$ provides more stable instantaneous frequency though the time of frequency shift is earlier than $\sigma = 1$ due to its longer time duration.

2.2 The Discrete Wavelet Transform

The calculating wavelet coefficients at every possible scale will generate a lot of redundant data which is not desirable since more computations and more memory are necessary to process a signal with redundancy. Therefore, a discrete version of the wavelet is utilized by discretizing the dilation parameter a and the translation parameter b in signal processing. The procedure becomes much more efficient if dyadic values of a and b are used. That is,

$$a = 2^j; \quad b = 2^k \quad j, k \in Z \quad (2.2.1)$$



where Z is a set of integers, j is referred to as the level, and k is the shifting coefficient.

DWT can be viewed as the filtering process which decompose signal into two parts, the detail and approximate part. For the detail part, which using the high-pass filter $\psi(t)$, is defined as:

$$cD_{j,k} = 2^{-j/2} \int_{-\infty}^{\infty} x(t)\psi^*(2^{-j}t - k)dt \quad (2.2.2)$$

For the approximate part derived from the low-pass filter $\phi(t)$:

$$cA_{j,k} = 2^{-j/2} \int_{-\infty}^{\infty} x(t)\phi^*(2^{-j}t - k)dt \quad (2.2.3)$$

where $\phi(t)$ is the scaling function derived from the mother wavelet. Note that not every wavelet function has scaling function and the algorithm is only available for orthogonal wavelet function which has scaling function and permits the fast algorithm. Due to the orthogonal property, a signal can be represented by its details and approximates. The detail and approximate at level j are defined as

$$D_j = \sum_{k=-\infty}^{\infty} cD_{j,k}\psi_{j,k}(t) \quad (2.2.4)$$

$$A_j = \sum_{k=-\infty}^{\infty} cA_{j,k}\phi_{j,k}(t) \quad (2.2.5)$$

It becomes obvious that

$$A_{j-1} = A_j + D_j \quad (2.2.6)$$

$$x(t) = A_j + \sum_{j \leq J} D_j \quad (2.2.7)$$

The DWT decomposition procedure can be shown as a DWT tree (**Figure 2-12**).



2.3 The Wavelet Packet Transform

Since the DWT only decompose the approximation part in lower frequency, the high frequency resolution remains the same. As a result, there might be the problem that the important information exists in the higher frequency. Therefore, to provide a better resolution, the wavelet packet transform (WPT) is developed to further decompose the detail components. The concept of WPT is shown as the WPT tree in **Figure 2-13**. The WPT is a function with three parameters:

$$\psi_{j,k}^i(t) = 2^{j/2} \psi^i(2^j t - k), \quad i=0, 1, 2, \dots, (2^j - 1) \quad (2.2.8)$$

where i, j and k refer to the modulation, scale and translation, respectively. The wavelet ψ^i is obtain from the recursive relationships:

$$\psi^{2i}(t) = \sqrt{2} \sum_{k=-\infty}^{\infty} h(k) \psi^i(2t - k) \quad (2.2.9)$$

$$\psi^{2i+1}(t) = \sqrt{2} \sum_{k=-\infty}^{\infty} g(k) \psi^i(2t - k) \quad (2.2.10)$$

where $h(k)$ and $g(k)$ are quadrature mirror filters associated with the scaling function and mother wavelet function. Note that ψ^0 is the scaling function ϕ and ψ^1 is the mother wavelet. Similar to DWT, the signal can be reconstructed by linear combination of decomposed components of WPT:

$$x(t) = \sum_{i=0}^{2^j-1} x_j^i(t) \quad (2.2.11)$$

The decomposed part of $x_j^i(t)$ is represent by a linear combination of wavelet packet function $\psi_j^i(t)$:



$$x_j^i(t) = \sum_{k=-\infty}^{\infty} c_{j,k}^i \psi_{j,k}^i(t) \quad (2.2.12)$$

where the wavelet packet coefficient $c_{j,k}^i$ can be obtained from:

$$c_{j,k}^i = \int_{-\infty}^{\infty} x(t) \psi_{j,k}^i(t) dt \quad (2.2.13)$$

Providing that the wavelet packet functions are orthogonal

$$\psi_{j,k}^m(t) \psi_{j,k}^n(t) = 0, \text{ if } m \neq n \quad (2.2.14)$$

In WPT, the central frequency of wavelet component is not in ascending order resulted from the aliasing, instead, it's a Paley order. Therefore, the ordering process need to be considered if the WPT technique is implemented. The Paley ordering process is illustrated in **Figure 2-14**.

2.4 Hilbert Transform

The Hilbert transform of a real-valued function $x(t)$ extended over the range $-\infty < t < \infty$ is a real-valued function $\tilde{x}(t)$ defined by [7]

$$\tilde{x}(t) = H[x(t)] = \int_{-\infty}^{\infty} \frac{x(u)}{\pi(t-u)} du \quad (2.3.1)$$

Thus $\tilde{x}(t)$ is the convolution integral of $x(t)$ and $1/\pi t$, written as

$$\tilde{x}(t) = x(t) * (1/\pi t) \quad (2.3.2)$$

The Hilbert transform is simply a 90 degrees rotation in the phase angle of the original signal. And the analytic signal $z(t)$ associated with $x(t)$ can be defined as:

$$z(t) = x(t) + i\tilde{x}(t) \quad (2.3.3)$$

One can also write

$$z(t) = A(t)e^{i\theta(t)} \quad (2.3.4)$$

where $A(t)$ is the Hilbert amplitude/ envelope signal of $x(t)$ and $\theta(t)$ is the instantaneous phase signal of $x(t)$.

$$A(t) = \sqrt{x^2(t) + \tilde{x}^2(t)} \quad (2.3.5)$$

$$\theta(t) = \tan^{-1} \left[\frac{\tilde{x}(t)}{x(t)} \right] = 2\pi f_0 t \quad (2.3.6)$$

The “instantaneous frequency” f_0 is given by

$$f_0 = \left(\frac{1}{2\pi} \right) \frac{d\theta(t)}{dt} \quad (2.3.7)$$



Chapter 3. Damage Assessment Algorithms

-Ambient Vibration Data



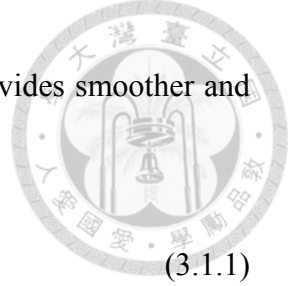
In the damage assessment technology, the most commonly used indicator can be divided into two parts: physical features and damage indices. In this chapter, 5 algorithms will be introduced and applied to the ambient vibration data, which include: (1) Marginal spectrum, (2) Central frequency, (3) Novelty index, (4) Correlation, and (5) Normalized component energy. The first two are physical features and the others are damage indices. These algorithms can provide the information about the healthy or damage state of the structure. Two experimental data will be utilized to verify these algorithms.

Because the wavelet parameter b has the meaning of time t , and $\omega = 2\pi f$, therefore, in the following discussion, we change the notation of wavelet coefficients from $W_\psi[x](b, \omega)$ to $W_\psi[x](t, f)$.

3.1 Damage assessment algorithms

3.1.1 Marginal Spectrum

A traditional way to investigate signals includes the spectral analysis through Fourier transform. The modal frequency of the structure will induce a peak in the Fourier spectrum, but sometimes it's hard to find the modal frequency because of the high resolution of fast Fourier transform and the noise of the signal might cause several peaks



near that position. The marginal spectrum of the MCMW+VCF provides smoother and lower-resolution spectrum which can be defined as:

$$H_{At}(f) = \sum_t |W_\psi[x](t, f)| \quad (3.1.1)$$

Based on the marginal spectrum, the frequency band can be chosen to calculate the following damage assessment algorithms.

3.1.2 Central Frequency

An easy way to observe the global behavior of the structure under the excitation is central frequency, which is defined as:

$$f = \frac{\sum_j H_{At}^2(f_j) f_j}{\sum_j H_{At}^2(f_j)} \quad (3.1.2)$$

where f_j is the selected frequency band from the marginal spectrum. The structural stiffness degradation will cause the change of system dominant frequency. Hence, the identification of central frequency can provide the dominant frequency of the structure and also a rough assessment of damage severity by only analyzing the output signal.

3.1.3 Novelty Index (reference-based index)

The shapes of the wavelet coefficients time-frequency plots can be compared by visual inspection, or alternatively, Novelty index. Novelty detection aims to establish



simply whether or not a new pattern is significantly different from a previous pattern.

Consider the white noise response measurement, based on the MCMW+VCF, the Novelty

index (NIn) is defined as:

$$NIn_i = \frac{\sum_t \sum_j |H_A^i(t, f_j) - H_A^{ref}(t, f_j)|}{\sum_t \sum_j |H_A^{ref}(t, f_j)|}, \quad i: \text{for test case } i \quad (3.1.3)$$

$$H_A(t, f) = |W_\psi[x](t, f)| \quad (3.1.4)$$

where $H_A(t, f)$ is the modulus of wavelet coefficients, $H_A^{ref}(t, f)$ is refer to as the undamaged reference data, and f_j is the selected frequency band from the marginal spectrum. Novelty index can compare not only the frequency shift but also energy change due to the damage.

3.1.4 Correlation (reference-based index)

Another comparison of scalograms of the wavelet coefficients is by correlating both sets of data for the selected frequency band [13]. The correlation coefficient is defined as

$$Corr_i = \frac{\sum_t \sum_j (H_A^i(t, f_j) - \overline{H_A^i(t, f_j)}) (H_A^{ref}(t, f_j) - \overline{H_A^{ref}(t, f_j)})}{\sqrt{\sum_t \sum_j (H_A^i(t, f_j) - \overline{H_A^i(t, f_j)})^2 \sum_t \sum_j (H_A^{ref}(t, f_j) - \overline{H_A^{ref}(t, f_j)})^2}} \quad (3.1.5)$$

where the bar denotes the mean of the wavelet coefficients and f_j is the selected frequency band from the marginal spectrum.



3.1.5 Normalized Component Energy

For the small ambient vibration and white noise, the response signal can be normalized by input signal. It is shown that the energy of the wavelet coefficients are functions of the physical parameters of the system and loading functions. Therefore, the normalized component energy (normalized CE) can be used as a damage assessment index, which is defined as:


$$\text{Normalized CE} = \frac{\sum_t \sum_j |H_E^i(t, f_j)|}{\sum_t \sum_j |H_E^{\text{input}}(t, f_j)|}, \quad i: \text{ for } i^{\text{th}} \text{ floor} \quad (3.1.6)$$

where $H_E(t, f) = |W_\psi[x](t, f)|^2$ is the component energy and f_j is the selected frequency band from the marginal spectrum.

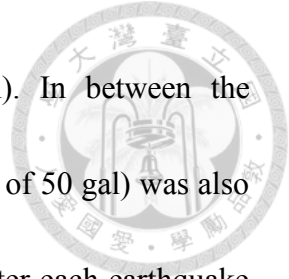
3.2 Application to Twin-tower Structure with Weak Bracing System

3.2.1 Set-up of monitoring system

The first model used for the experimental verification is the twin-tower structure. A steel structure with two towers (tower-A: 5 story and tower-B: 4 story) connected at basement as well as the 1st floor (**Figure 3-1**) was constructed and tested on the shaking table in National Center of Research on Earthquake Engineering (NCREE), Taipei, Taiwan. Each story with height of 1.17 m and 500 kg was added to each floor to simulate floor weight. The dimension of the plate was 1.1 m × 1.5 m × 0.02 m. The H-type



column with the dimension of 0.1 m × 0.03 m × 1.1 m was used for all floor. In EW-direction, the bracing system using L-shape angle steel with the dimension of 65 mm × 65 mm × 6 mm was designed with large buckling load to prevent transverse motion during the test, and in NS-direction, the bracing system was designed with smaller buckling load as compare to the EW-direction. Two types of braces were used in NS-direction. The dimension of Brace1 was 19 mm × 1.2 mm to simulate the weak location and Brace2 with dimension of 21.3 mm × 2 mm was used as normal condition. Three different damage scenarios were created. Damage scenrario-1 was to create buckling in the 1st floor of tower-A, damage scenario-2 was to create buckling in the 2nd floor of tower-A, and damage scenario-3 was to create buckling in the 2nd floor of tower-B. The buckling of three cases was setup by installing weak bracing members (Brace1) in that floor. The configuration of the structure is shown in **Figure 3-2**. There were in total 22 accelerometers, 22 LVDTs instrumented in this experiment. For tower-A, 12 accelerometers and 12 LVDTs in x-direction for all floors and tower-B had the same instrumentation as tower-A with 10 accelerometers and 10 LVDTs in x-direction for all floors. The distribution of accelerometer and the LVDT is shown in **Figure 3-3**. The sampling rate of all the sensor devices is 200 Hz. The spectrum compatible acceleration record (from Chi-Chi earthquake station TCU071) was used as the desired base excitation of the shaking table. The base excitation was arranged back to back with different input



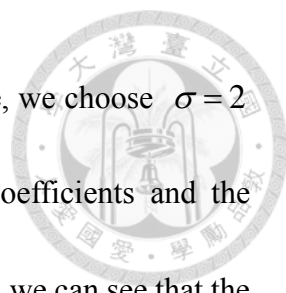
intensity level and applied in x-direction only (North direction). In between the earthquake excitation, white noise excitation (with peak acceleration of 50 gal) was also applied to serve as the reference state of the structure before and after each earthquake excitation. The test protocol for damage scenario-1, 2, and 3 are shown in **Table 3-1**. Take average of the LVDT records ($(Disp_{X-Right} + Disp_{X-Left}) / 2$) collected from earthquake for each floor to calculate the maximum interstory drift ratio (IDR) (**Figure 3-4**). For damage scenario-1, the 1st floor of two towers both show the increasing IDR with test cases because of the connection in that floor. For damage scenario-2, the increasing IDR in 2nd floor of tower-A matches the setup of weak location. And there is also the slight changes of IDR in tower-B. For damage scenario-3, though the setup of weak location is in the 2nd floor of tower-B, there is apparent interstory drift ratio happened in the 2nd floor of tower-A after test case 4. This implies that there is also damage occurred in that floor.

3.2.2 Pre-processing procedure

Data collected from white noise will be used in this chapter. Take average of the absolute acceleration in x-direction ($(Acc_{X-Right} + Acc_{X-Left}) / 2$) for each floor as the motion in longitudinal direction.

White Noise Response Data

Applying the proposed MCMW+VCF to the white noise acceleration response. Here

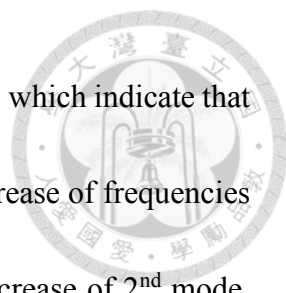


we focus more on the frequency domain than time domain, therefore, we choose $\sigma = 2$ to enhance the frequency resolution. The scalogram of wavelet coefficients and the marginal spectrum are shown in **Appendix I**. For damage scenario-1, we can see that the dominant change of frequency happened in the 1st mode for both tower-A and tower-B. There's almost no frequency shift from WN1 to WN4 and apparent frequency shift shows in WN5, after that, WN6 and WN7 show the frequency shift, too. For damage scenario-2, the dominant frequency for 1st floor of tower-A and all floor of tower-B occurs in 2nd mode, but the dominant frequency of 2nd to 5th floor of tower-A is 1st mode. For damage scenario-3, the dominant frequency changes from 2nd mode to 1st mode with the increase of test cases. Therefore, the frequency ranges of 0~6 Hz, which cover the 1st mode, and 0~10 Hz, which cover the 1st and 2nd mode, will be used for the feature extraction.

3.2.3 The Results of Damage Assessment

Central Frequency

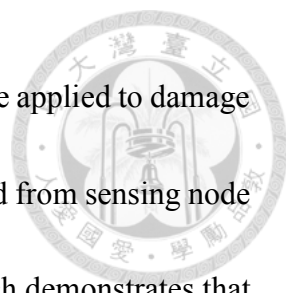
The results of central frequency are plotted in **Figure 3-5** (w.r.t. frequency band: 0~6 Hz) and **Figure 3-6** (w.r.t. frequency band: 0~10 Hz). For damage scenario-1, the central frequencies of two frequency bands both show the decrease with test cases and converge to the lowest floor, which indicate that the damage occurs in the lowest floor. For damage scenario-2, the central frequencies calculated from two bands both show the frequencies



from 2nd to 5th floor of tower-A decrease and converge to the 2nd floor, which indicate that the damage happens in the 2nd floor. On the other hand, the small increase of frequencies in 1st floor of tower-A and all floor in tower-B may cause by the decrease of 2nd mode, which can be seen in marginal spectrum (**Appendix I**) and may also imply the damage occurrence. For damage scenario-3, the clearer change of central frequencies from 2nd to 5th floor of tower-B demonstrate that the damage locates in 2nd floor of tower-B. From the observation, the frequencies decrease in WN4 w.r.t. frequency band: 0~6 Hz, but show earlier drop in WN3 w.r.t. frequency band: 0~10 Hz. The reason resulting in this case is because the 2nd mode in WN3 is close to the 1st mode in WN1, therefore, the frequencies w.r.t. frequency band: 0~6 Hz do not show the changes in WN3, but reflect w.r.t. frequency band: 0~10 Hz. The frequency changes in all floors of tower-A may imply the damage occurs in lower floor.

Novelty Index (NIn)

For each floor, using equation (3.1.3) to compare difference test cases with reference (WN1). The results of *NIn* w.r.t. two frequency bands are plotted in **Figure 3-7** and **Figure 3-8**. For damage scenario-1, the *NIn* increases with test cases, which means the difference of scalogram between reference and test case is getting large, and indicates the damage extent is getting severer, too. Besides, the *NIn* from different sensing node are very similar. This indicates that each floor has similar response and explains the



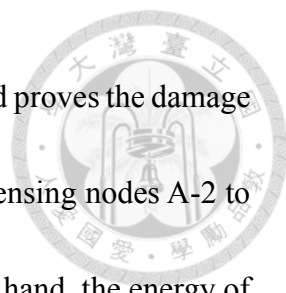
possibility for damage locates in the 1st floor. Similar approach also be applied to damage scenario-2 and 3. For damage scenario-2, the values of NIn calculated from sensing node A-2 to A-5 are very similar and larger than other sensing nodes, which demonstrates that the damage locates in the 2nd floor of tower-A. And for damage scenario-3, the increase of NIn above 2nd floor of tower-B are larger than others, which implies the severest damage occurs in 2nd floor of tower-B. It has to mention that for damage scenario-2, the values of NIn in last test case does not show the apparent growth while the marginal spectrum shows the decrease of modal frequency. This brings out the disadvantage of NIn that the index cannot reflect the distance if the frequency shifts far away from the reference.

Correlation

For each floor, using equation (3.1.5) to compare difference test cases with reference (WN1). The results of correlation w.r.t. two frequency bands are plotted in **Figure 3-9** and **Figure 3-10**. From the observation, this index can also can be used to detect and locate the damage, but same as the Novelty index, the correlation cannot reflect the distance if the frequency shifts far away from the reference.

Normalized Component Energy (Normalized CE)

The results of normalized CE w.r.t. two frequency bands are plotted in **Figure 3-11** and **Figure 3-12**. For damage scenario-1, all the normalized CE converged to the lowest

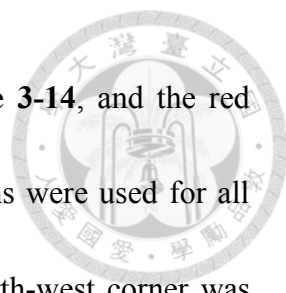


floor, which indicates that the energy of all sensors are very similar and proves the damage location is in the 1st floor. For damage scenario-2, the energy from sensing nodes A-2 to A-5 all converge together as the case number increases. On the other hand, the energy of other sensing nodes remain the same. This implies the damage location is at 2nd floor of tower-A. For damage scenario-3, the normalized CE above 2nd floor for two towers both show the changes while the 1st floors remain stable. This implies the damage may occur in the 2nd floor. But in this case, the trend is not consistent with the other two damage scenarios, therefore, it cannot show the degree of damage.

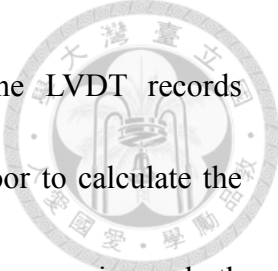
3.3 Application to Two Three-story steel frames

3.3.1 Set-up of monitoring system

The second model used for the experimental verification is the two three-story steel frames, specimen-1 and specimen-2 respectively (**Figure 3-13**). This experiment was also conducted in NCREE. The frames with an overall height of 3.51 m and an approximate total weight of each structure was 2.94 ton (include additional 0.5 ton on each floor). The dimension of the plate was 1.1 m × 1.5m × 0.02 m. Two types of rectangular columns were used in the steel frame test. The dimension of type-1 column was 0.15 m × 0.025 m × 1.1 m and in type-2 column, there was a reduction of thickness with dimension of 0.15 m × 0.015 m × 1.1 m to simulate a weaker column in comparison with type-1



column. The components of the steel frames are shown in **Figure 3-14**, and the red column denotes the type-2 column. For specimen-1, type-1 columns were used for all floors while for specimen-2, one column in the 1st floor at the north-west corner was replaced with type-2 column. Therefore, specimen-1 was a symmetric structure while specimen-2 was an anti-symmetric structure. The configuration of the steel frame test is shown in **Figure 3-15**. There were in total 18 accelerometers, 19 LVDTs instrumented in this experiment. For specimen-1, 6 accelerometers and 6 LVDTs in x-direction for all floors and specimen 2 had the same instrumentation as specimen 1 with additional 6 accelerometers and 6 LVDTs in y-direction for all floors. The distribution of accelerometer and the LVDT is shown in **Figure 3-16**. The sampling rate of all the sensor devices is 200 Hz. The spectrum compatible acceleration record (from Chi-Chi earthquake station TCU071) was used as the desired base excitation of the shaking table. The base excitation was arranged back to back with different input intensity level and applied in x-direction only (North direction). In between the earthquake excitation, white noise excitation (with peak acceleration of 50 gal) was also applied to serve as the reference state of the structure before and after each earthquake excitation. The test protocol is shown in **Table 3-2**. With an increasing excitation level, the nonlinearity of the steel frame exhibits and the damage of the structure becomes more severe. The hysteresis loop in **Figure 3-17** and **Figure 3-18** both show that the nonlinearity become




significant after the case EQ 6 (850 gal). Take average of the LVDT records $((Disp_{X-Right} + Disp_{X-Left})/2)$ collected from earthquake for each floor to calculate the maximum interstory drift ratio (IDR) (**Figure 3-19**). The result of two specimens both show the slight increasing trend with test cases. And take the LVDT records in y-direction of specimen-2 to check the torsion motion (**Figure 3-20**). From the result, we can find the increasing maximum story drift, which matches the unsymmetrical setup.

3.3.2 Pre-processing procedure

Data collected from white noise will be used in this chapter. Take average of the absolute acceleration in x-direction $((Acc_{X-Right} + Acc_{X-Left})/2)$ for each floor as the motion in longitudinal direction and take average of $(Acc_{X-Right} - Acc_{X-Left})/2$ for each floor as torsion motion.

White Noise Response Data

Applying the proposed MCMW+VCF to the white noise acceleration response. Here we focus more on the frequency domain than time domain, therefore, we choose $\sigma = 2$ to enhance the frequency resolution. The scalogram of wavelet coefficients and the marginal spectrum are shown in **Appendix II**. According to the results, the specimen-1 has torsional mode and hence the unsymmetrical behavior exists. The clearer scalogram and higher value of marginal spectrum for torsion motion of specimen-2 demonstrates the



unsymmetrical setup. With the increase of test cases, there's almost no frequency shift in x-direction and only small change of frequency in torsion motion. For the feature extraction, based on the marginal spectrum, 0~5 Hz is chosen as the frequency band for x-direction with the covered of 1st mode, and 25~40 Hz is chosen for torsional direction with the covered of dominant frequency.

3.3.3 The Results of Damage Assessment

Central Frequency

For the white noise response data, we focus on the 1st mode of x-direction and dominant mode of torsion motion. The results are plotted in **Figure 3-21**. The central frequencies for all floors and test cases remain the same in x-direction and there's slight frequency shift in torsion motion for both specimen-1 and 2. Therefore, central frequency cannot be used to detect the stronger unsymmetrical behavior in specimen-2.

Novelty Index (NIn)

The *NIn* calculated from x-direction (frequency band: 0.0~5.0 Hz) for both specimen-1 and 2 didn't show significant change through test cases, but the slightly grows of *NIn* after test case 6 reflects the energy change, as plotted in **Figure 3-22**. While the calculated *NIn* from torsion responses (frequency band: 25.0~40.0 Hz) for 2 specimens is getting larger from event to event, which indicates that the changes of response in

comparison with reference become larger through test cases. Besides, the higher value of NIn in specimen-2 confirms that the anti-symmetric behavior of specimen-2 is stronger than specimen-1.



Correlation

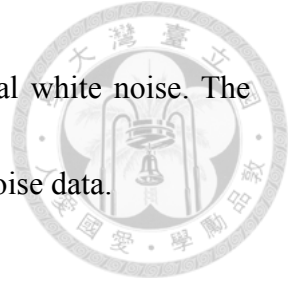
The calculated correlation for two directions are plotted in **Figure 3-23**. Similar to the results of NIn , the correlation can also be used to explain the unsymmetrical setup of specimen-2, but the performance of the energy change in x-direction is not clearly. This reflects that the correlation cannot compare two sets of data with same distribution, but different values.

Normalized Component Energy

The application of normalized CE in two 3-story structures doesn't show the damage increase with the test cases (**Figure 3-24**). It only shows that the response in x-direction and torsional direction of specimen-2 are larger than specimen-1's. This can only confirm the anti-symmetric of specimen-2, but cannot detect the extent of damage.

3.4 Chapter Summary

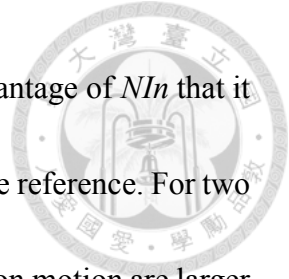
In this chapter, 5 algorithms were introduced and two types of structures (a twin-tower structure: damage in lower mode and two 3-story steel frames: nonlinear behavior) were tested and discussed. Both experiments with ascending excitation levels were



conducted on the shake table in NCREE and in between with 50gal white noise. The proposed damage assessment algorithms were applied to the white noise data.

A brief discussion of the proposed methods is given:

1. The time-frequency scalogram of the MCMW+VCF successively present the frequency shift among different test cases of the twin-tower structure. For two 3-story steel frames, the frequency in x-direction does not change for each case though the structure shows high nonlinearity under strong excitation. On the other hand, the slightly changed torsional mode for both specimen 1 and specimen 2 can be observed. The torsional mode for specimen 2 is clearer than specimen 1 because of the unsymmetrical setup.
2. The marginal spectrum and central frequency both show the frequency content of the structure. The marginal spectrum provides us to choose the frequency bandwidth to calculate the damage index and central frequency is consistent with the stiffness and strength degradation. For twin-tower structure, based on the selected frequency bandwidth, the decrease of the central frequency shows the damage severity and also the damage location. For two 3-story steel frames, the frequency has no significant difference between test cases, but the higher amplitude of marginal spectrum in torsional direction of specimen-2 demonstrates the significant torsion motion.
3. The application of Nln to twin-tower structure can detect and locate the damage for



three damage scenarios. Besides, in this case, it shows the disadvantage of NIn that it cannot reflect the distance if the frequency shifts far away from the reference. For two 3-story steel frames, the NIn of 2 specimens calculated from torsion motion are larger than x-direction and specimen-2 have larger NIn than specimen-1. It confirmed the stronger unsymmetrical behavior of specimen-2.

4. The correlation can also be used to identify the damage for both experiments, but same as NIn , it cannot reflect the distance if the frequency shifts far away from the reference, besides, it cannot compare two sets of data with same distribution, but different values.
5. The application of normalized component energy to twin-tower structure can also detect and locate the damage for both damage scenario-1 damage scenario-2. For two 3-story steel frames, the normalized CE can only show the response of specimen-2 in both directions are larger than specimen-1.

Chapter 4. Damage Assessment Algorithms

-Earthquake Response Data



In this chapter, 4 algorithms will be applied to the earthquake response data, which include: (1) Marginal spectrum, (2) Central frequency, (3) Pseudo-instantaneous frequency, and (4) Unwrapped phase. These four indices are physical features and the first two have introduced in Chapter 3. Also, the two experiments that have introduced and used in the previous chapter will be utilized to verify the algorithms, too.

4.1 Damage assessment algorithms

4.1.1 Pseudo-instantaneous Frequency

The instantaneous frequency can provide the information of frequency varies with time, a tendency to identify the system nonlinearity, a rough assessment of damage severity, and also a clearer representation for scalogram because it is unapparent in comparatively small amplitude data. The most straight forward method to extract the instantaneous frequency is determining the ridge of the CWT of a signal. The ridge is the line of frequency f which the amplitude of the transform is maximum for each time t . This method is based on the energy of the signal which concentrate near its instantaneous frequency in a narrow time interval. But this method is easily affected by noise and results in a fluctuant instantaneous frequency, therefore, a smoothed method using a time-varying

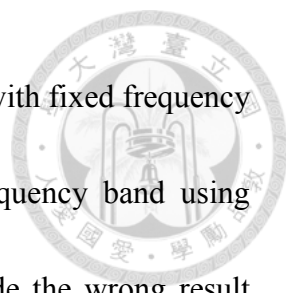


mean procedure to eliminate the fluctuations, which is called the pseudo-instantaneous frequency (pseudo-IF), is defined as:

$$f(t) = \frac{\sum_j H_A^2(t, f_j) f_j}{\sum_j H_A^2(t, f_j)} \quad (4.1.1)$$

where $H_A(t, f)$ is the modulus of wavelet coefficients defined in equation (3.1.4) and f_j is the time-varying frequency band. The time-varying frequency band is defined by the preceding determined frequency as the center with a $10\Delta f$ frequency band (Δf is the bandwidth of Morlet wavelet shown in **Figure 2-4**). It has to mention that the frequency of the first time point is extract from the ridge. The $10\Delta f$ is selected for the reason of no overlapping with the center frequency (**Figure 4-1**). In some cases, the decrease of frequency may drop outside the frequency band. Therefore, take the advantage of the ridge in reflecting the sudden frequency shift, the frequency band will change from $10\Delta f$ to 2 times of the frequency band defined as preceding frequency and the ridge of the present time point.

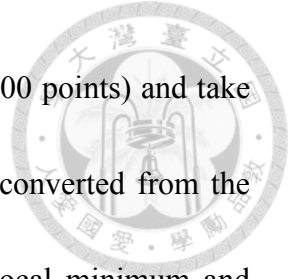
Use the RC frame in section 2.1.7 to compare the pseudo-IF by ridge extraction method, mean method with fixed frequency band (0~7 Hz), time-varying frequency band, and time-varying frequency band with ridge adjustment. The hysteresis loop is shown in **Figure 4-2** and the results are plotted in **Figure 4-3**. From the hysteresis loop, we can observe the sudden frequency shift around 29 secs, slow decrease of frequency from 30



to 40 secs, and remain stable from 40 to 50 secs. The mean method with fixed frequency band (green line) cannot present these features, time-varying frequency band using $\sigma = 2$ (yellow line) do not capture the frequency shift and provide the wrong result because the sudden decrease of frequency drops out the $10df$ frequency band, and the ridge extraction method (blue line) provide fluctuation results even in 40 to 50 secs. Therefore, these methods will not be used in the later experiments. For the time-varying frequency band with ridge adjustment (red line), $\sigma = 1$ shows the sudden frequency shift at 28.15 sec and $\sigma = 2$ shows at 27.23 sec, from 30 to 70 sec, $\sigma = 2$ provides more stable frequency than $\sigma = 1$. As the requirements of frequency stability and also the acceptable time of frequency shift, time-varying mean method with time-varying frequency band using $\sigma = 2$ is chosen to track the pseudo-IF.

In order to discuss the meaning of the pseudo-IF, we simulated a nonlinear SDOF system using plastic Wen model in SAP2000 software. The sampling rate is 200 Hz. The input acceleration, acceleration response, and relative displacement are plotted in **Figure 4-4**. The result of pseudo-IF is shown in **Figure 4-6**. From the observation, there are three local minimums appear around 31.5, 39.5, and 46 secs, and the global minimum appears around 31.5 secs. We check the hysteresis loop (**Figure 4-5**) and find that there are larger areas underneath the loop in these three small time duration. And the area enclosed by the small time duration around 31.5 secs shows the largest. Using the MATLAB function

‘polyfit’ with first order to fit the hysteresis loop in every second (200 points) and take the slope as stiffness. By comparing the pseudo-IF and frequency converted from the stiffness, we find that the pseudo-IF shows the accurate time of local minimum and performs the nonlinear behavior with a smoother result because of the 9.8 secs duration of mother wavelet.



4.1.2 Unwrapped Phase

Unwrapped phase is a physical index, which is related to the wave propagation and can be applied to monitor the change of the structural system. For RC structure, after earthquake excitation, damage as cracking may be induced and blocked the path for wave propagation and hence cause the phase difference. For the steel frame, the slope and final value of unwrapped phase decrease after series of excitation, which indicates the change of the structure behavior. By observing the unwrapped phase difference, it is possible to detect and locate the damage.

The complex wavelet coefficients gives the analytic signal of original signal $x(t)$ by taking the summation of wavelet coefficients in frequency domain:

$$H_{Cf}(f) = \sum_j W_w[x](t, f_j) \quad (4.1.2)$$

where f_j is the selected frequency band from the marginal spectrum and the instantaneous phase can be calculated as defined in section 2.4.



4.2 Application to Twin-tower Structure with Weak Bracing System

4.2.1 Set-up of monitoring system

The set up monitoring system has been described in section 3.2.1 and the data collected from earthquake will be used in this chapter.

4.2.2 Pre-processing procedure

Data collected from earthquake will be used in this chapter. Take average of the absolute acceleration in x-direction ($(Acc_{X-Right} + Acc_{X-Left})/2$) for each floor as the motion in longitudinal direction.

Earthquake Response Data

Applying the proposed MCMW+VCF to the earthquake acceleration response. Here we also choose $\sigma = 2$ to enhance the frequency resolution. The scalogram of wavelet coefficients and the marginal spectrum are shown in **Appendix I**. For damage scenario-1, the dominant change of frequency happened in the 1st mode after EQ4 for both tower-A and tower-B. For damage scenario-2, both 1st and 2nd mode are dominant for 1st floor of tower-A and all floor of tower-B while the dominant frequency of 2nd to 5th floor of tower-A is 1st mode. For damage scenario-3, the dominant frequency changes from 2nd mode to 1st mode with the increase of test cases. Therefore, the frequency ranges of 0~6 Hz, which cover the 1st mode, and 0~10 Hz, which cover the 1st and 2nd mode, will be

used for the feature extraction.



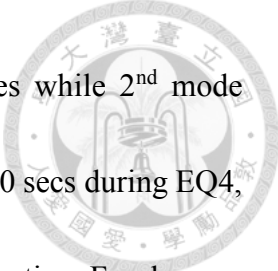
4.2.3 The Results of Damage Assessment

Central Frequency

The results of central frequency are plotted in **Figure 4-7** (w.r.t. frequency band: 0~6 Hz) and **Figure 4-8** (w.r.t. frequency band: 0~10 Hz). The value and trend of central frequency are similar with the central frequency calculated from white noise data. For damage scenario-1, the central frequency decreases after test case 4 for all floors, which indicates the damage occurred and the possible location is in the lowest floor. For damage scenario-2, similar approach can also be applied to demonstrate that the damage location is at 2nd floor of tower-A. For damage scenario-3, the central frequencies w.r.t. frequency band: 0~6 Hz didn't show the changes in EQ2, but decrease w.r.t. frequency band: 0~10 Hz. This phenomenon matches the result discussed in section 3.2.3 that the reason is because the 2nd mode in EQ2 is close to the 1st mode in EQ1.

Pseudo-instantaneous frequency (Pseudo-IF)


The top floor is chosen to calculate the pseudo-IF because it is relatively least influenced by the input excitation. Besides, the 1st mode is under 6 Hz and the 2nd mode is above 6 Hz, therefore, two mode can be calculated separately. The results of pseudo-IF for the sensing node A-5 and B-4 are shown in **Figure 4-9** to **Figure 4-11**. For damage



scenario-1, the pseudo-IF of 1st mode shows changes through cases while 2nd mode remains quite stable. The frequency shift of 1st mode occurs in 35 to 40 secs during EQ4, and EQ5 and EQ6 also show the small frequency shift in this time duration. For damage scenario-2, clear frequency shift of 1st mode can be seen in EQ2 and EQ3 for sensing node A-5, but the tracking of 2nd mode is not successful. This may due to the small vibration of this node in 2nd mode. The mode shape of white noise responses using automated SSI-COV (**Appendix I**) can proof the small vibration of the node A-2 to A-5 in tower-A. And for tower-B, the 2nd mode is comparatively more dominant than the 1st mode in marginal spectrum and mode shape, therefore, the tracking of the 2nd mode is more successful. The frequency remains stable from EQ1 to EQ4 then the decrease happened during EQ5. For damage scenario-3, the frequency shift of 1st mode can be observed clearly for both tower-A and tower-B, and the unstable of 2nd mode in EQ4 and EQ5 may also due to the small vibration of the node, which can be seen from the mode shape.

Unwrapped Phase

The calculated unwrapped phases are plotted in **Figure 4-12** to **Figure 4-14** (w.r.t. frequency band: 0~10 Hz). In this index, frequency band 0~10 Hz shows better results than frequency band: 0~6 Hz, which may due to the reason that the frequency band 0~10 Hz covers more global behavior where the 2nd mode drops in last few test cases. As shown



in **Figure 4-12**, for damage scenario-1, the final value of unwrapped phases show large drop in EQ4, and from EQ5 to EQ7, the values are even lower and all floor converge together. This implies the tendency of damage location in the 1st floor. For damage scenario-2 (**Figure 4-13**), the unwrapped phases change from 2nd to 5th floor in tower-A which also demonstrate the damage location in the 2nd floor. And in EQ5, the drop of the phase of all floor in tower-B might indicates the damage also happens in the lowest floor. For damage scenario-3 (**Figure 4-14**), in tower-A, the unwrapped phases from 2nd to 5th floor show decrease in EQ4, which may indicate that the damage occurs in 2nd floor, and in tower-B, the phases above 2nd floor drop from event to event, which implies that the damage happened in 2nd floor and matches the setup location of weak column. Besides, the phases of 1st floor in both tower show large growth in EQ5, which may due to the change of dominant frequency and imply that the damage occurs in the lowest floor.

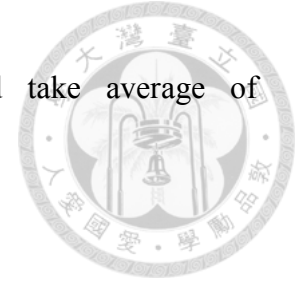
4.3 Application to Two Three-story steel frames

4.3.1 Set-up of monitoring system

The set up monitoring system has been described in section 3.3.1 and the data collected from earthquake will be used in this chapter.

4.3.2 Pre-processing procedure

Take average of the absolute acceleration in x-direction $((Acc_{X-Right} + Acc_{X-Left}) / 2)$



for each floor as the motion in longitudinal direction and take average of $(Acc_{X-Right} - Acc_{X-Left})/2$ for each floor as torsion motion.

Earthquake Response Data

For the earthquake response data, we also choose $\sigma = 2$ to enhance the frequency resolution. The scalogram of wavelet coefficients are shown in **Appendix II**. The results also show that there's almost no frequency shift in x-direction and the unsymmetrical behavior of specimen-1 due to the existence of torsional mode. Besides, it seems that there is the change of dominant frequency from higher to lower mode with the increase of earthquake excitation level. Therefore, for the feature extraction, based on the marginal spectrum, 0~5 Hz is also chosen as the frequency band for x-direction with the covered of 1st mode, but 0~50 Hz is chosen for torsional direction with the observation of the change of dominant frequency.

4.3.3 The Results of Damage Assessment

Central Frequency

Based on the first mode of x-direction and the frequency band of 0~50 Hz for torsion motion for earthquake response, the central frequency for both specimen-1 and 2 are shown in **Figure 4-15**. We can see only the slight frequency changes in x-direction, but for torsion motion, the dominant frequencies for specimen-1 from test case 2 to 5 remain quite stable in higher mode while for specimen-2, they decrease to lower mode from event

to event. This may demonstrate that the torsion motion of specimen-2 has larger response than specimen-1.



Pseudo-instantaneous frequency (Pseudo-IF)

The pseudo-IF for x-direction and torsional direction of specimen-1 and specimen-2 are plotted in **Figure 4-16** and **Figure 4-17**. The results in x-direction show that the frequency are quite stable during earthquake excitation and the drop of frequency during 10~20 sec is in order with earthquake excitation level. The pseudo-IF in torsional direction for specimen-1 and specimen-2 are fluctuant because they occur at higher mode, for specimen-2, it can still observe that the frequency drops in order with excitation level and for specimen-1, the results show more fluctuant due to the unapparent torsion mode.

Unwrapped Phase

Based on the selected frequency band, the analytic signal for all sensors and test cases are reconstructed. The slope and final value of unwrapped phase from individual sensor in x-direction (**Figure 4-18**) shows almost no change among test cases for both specimen-1 and specimen-2. Therefore, the unwrapped phase in x-direction cannot detect an abnormal condition of the structure. Hence, it is impossible to use this information to detect the damage location. On the contrary, the slope and final value of unwrapped phase in torsional direction of specimen-1 and specimen-2 show the difference (**Figure 4-19**). For specimen-1, the unwrapped phases of torsion motion from the first five earthquake

excitation show almost no difference for all floors while for specimen-2, the unwrapped phases of torsion motion decrease from event to event, which implies stronger behavior of torsional responses in specimen-2.



4.4 Chapter Summary

In this chapter, 2 algorithms were introduced and two types of structures (twin-tower structure: damage in lower mode and two 3-story steel frames: nonlinear behavior) were tested and discussed. The proposed damage assessment algorithms were applied to the earthquake response data.

A brief discussion of the proposed methods is given:

1. The time-frequency scalograms of the MCMW+VCF present the frequency shift during the earthquake excitation for the twin-tower structure. For two 3-story steel frames, the scalograms in x-direction show almost no change through test cases and the change of dominant frequency in torsional direction for both specimen 1 and specimen 2 can be observed. Also, the torsional mode for specimen 2 is clearer than specimen 1 because of the unsymmetrical setup.
2. Based on the selected frequency band from marginal spectrum then calculate the central frequency. For twin-tower structure, the central frequencies can detect and locate the damage. For two 3-story steel frames, the earlier frequency shift in torsional



direction of specimen-2 implies the earlier change of dominant frequency and the stronger behavior of torsion motion in the specimen.

3. The pseudo-IF displays the abrupt frequency change for twin-tower structure, shows the stable frequency in x-direction, and more apparent torsion mode of specimen-2.

The fluctuation in some cases may be caused by the ridge adjustment, which provides the wrong frequency with largest amplitude influenced by the noise or input excitation, and it is hard to track the frequency if the vibration is unapparent for the sensing node.

4. The application of unwrapped phase to twin-tower structure also detect and locate the damage for three damage scenarios. And for two 3-story steel frames, the unwrapped phase shows the torsion motion of specimen-2 has stronger behavior than specimen-1, which matches the results of central frequency and pseudo-IF.

Chapter 5. Field Application



The main purpose of this chapter is to verify the efficiency and accuracy of the proposed MCMW+VCF and damage indices in field experiments.

5.1 Application to Mingli Elementary School

The Mingli elementary school locates in the Hualien City, Hualien County, Taiwan.

5.1.1 Set-up of monitoring system

Thirty accelerometers were instrumented in this RC structure. The sampling rate was determined with 200 Hz. The layout of sensors is shown in **Figure 5-1**. Five of earthquake events are picked and analyzed using the proposed scheme, include one event (EV04-1999/09/20) before Chi-Chi earthquake, two events (EV05, EV06-1999/09/20) during Chi-Chi earthquake, and two events (EV13-2006/12/26, EV31-2010/10/02) after retrofit. The peak acceleration (PA) of every recorded earthquake event is plotted in **Figure 5-2**.

5.1.2 Pre-processing procedure

Sensor #28, #5, #14, #19 are chosen as the basement (input), 2F (output), 3F (output), 4F (output) in longitudinal direction (y dir.) and sensor #27, #10, #16, #22 are chosen as the basement (input), 2F (output), 3F (output), 4F (output) in transverse direction (x dir.). The recorded accelerations of basement in both directions are used to select the start time



to do the analysis, which are plotted in **Figure 5-3**.

Earthquake Response Data

Applying the proposed MCMW+VCF to the earthquake acceleration response with $\sigma = 2$ to enhance the frequency resolution. The scalogram of wavelet coefficients and the marginal spectrum are shown in **Appendix III**. For both direction, EV05 shows the lowest modal frequency, which may imply the severe damage happened, and EV31 shows the highest, which proves the success of retrofit. Based on the marginal spectrum, 1.5~5 Hz in y-direction and 1~4 Hz in x-direction are chosen as the frequency band to calculate the damage assessment algorithms.

5.1.3 The Results of Damage Assessment

Central Frequency

The result of central frequencies for the five chosen events is plotted in **Figure 5-4**. The lowest frequency for both directions occurs in the EV05, which is the mainshock of Chi-Chi earthquake, and the larger frequencies of EV13 and EV31 in comparison to the previous events indicate the success of retrofit.

Unwrapped Phase

The results of unwrapped phase is plotted in **Figure 5-5**. The lowest slope in EV05 indicates the severest damage among these events and the similar trend of all floors shows



the possibility of damage occurred in the lowest floor. The higher slopes of EV13 and EV31 also demonstrate the success of retrofit.

Pseudo-instantaneous frequency (Pseudo-IF)

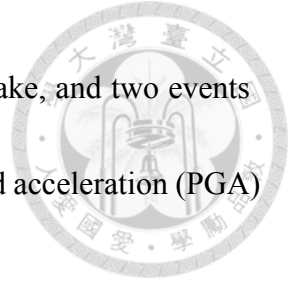
The pseudo-IF of 4F for five events are shown in **Figure 5-6** to **Figure 5-10**. From the observation, the frequency fluctuates under small earthquake excitation (EV04, EV06, EV13, and EV31), especially in y-direction, which is due to the affection of noise. And it has to mention that, for large earthquake excitation (EV05), the absolute acceleration is strongly affected by input excitation in lower frequency and leads to the wrong result, therefore, the relative acceleration is used to calculate the pseudo-IF and the result shows the frequency decreasing with time in y-direction.

5.2 Application to NCHU Civil & Environmental Engineering Building

The Civil & Environmental Engineering Building of National Chung Hsing University locates in the Taichung City, Taiwan.

5.2.1 Set-up of monitoring system

Twenty-nine accelerometers were instrumented in this RC structure. The sampling rate was determined with 200 Hz. The layout of sensors is shown in **Figure 5-11**. Five of earthquake events are picked and analyzed using the proposed scheme, include one event (EV09-1996/03/05) before Chi-Chi earthquake, one event (EV13-1999/09/20) during



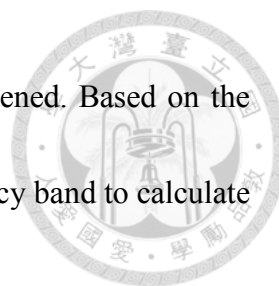
Chi-Chi earthquake, one event (EV27-1999/09/24) after the earthquake, and two events (EV59-2006/03/09, EV94-2009/11/05) after retrofit. The peak ground acceleration (PGA) of every recorded earthquake event is plotted in **Figure 5-12**.

5.2.2 Pre-processing procedure

Sensor #27, #15, #22 are chosen as the 1F (input), 4F (output), 7F (output) in one side of longitudinal direction (x1 dir.) and sensor #25, #13 #19 are chosen as the 1F (input), 4F (output), 7F (output) in another side of longitudinal direction (x2 dir.). Sensor #24, #12, #18 are chosen as the 1F (input), 4F (output), 7F (output) in one side of transverse direction (y1 dir.) and sensor #26, #14 #21 are chosen as the 1F (input), 4F (output), 7F (output) in another side of transverse direction (y2 dir.). Take average of the absolute acceleration in x-direction ($(Acc_{x1} + Acc_{x2})/2$) for each floor as the motion in longitudinal direction and take $(Acc_{y1} - Acc_{y2})/2$ for each floor in transverse direction. The recorded acceleration of 1F in both directions are used to select the start time to do the analysis, which are plotted in **Figure 5-13**.

Earthquake Response Data

Applying the proposed MCMW+VCF to the earthquake acceleration response with $\sigma = 2$ to enhance the frequency resolution. The scalogram of wavelet coefficients and the marginal spectrum are shown in **Appendix III**. For both direction, EV13 shows the



lowest modal frequency, which may imply the severe damage happened. Based on the marginal spectrum, 1~4 Hz in both direction is chosen as the frequency band to calculate the damage assessment algorithms.

5.2.3 The Results of Damage Assessment

Central Frequency

The result of central frequencies for the five events is plotted in **Figure 5-14**. The lowest frequencies for both directions occur in EV13, which is the mainshock of Chi-Chi earthquake, and the frequencies regain in EV59 and EV94 indicate the success of retrofit.

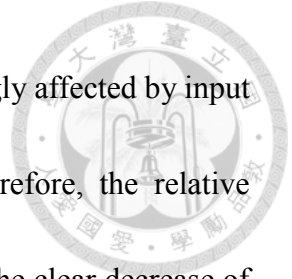
Unwrapped Phase

The result of unwrapped phase is shown in **Figure 5-15**. The unwrapped phase of EV13 shows the lowest slope and two floor have the similar trend, which implies the severest damage among five events and the damage may happen in the lower floor. The slope of EV59 and EV94 are larger than EV13's, but lower than EV09's. This may imply the success of retrofit, but did not reach the initial condition of structure.

Pseudo-instantaneous frequency (Pseudo-IF)

The pseudo-IF of 7F for five events are shown in **Figure 5-16** to **Figure 5-20**. The response in the beginning and end of the small earthquake excitation (EV09, EV27, EV59, and EV94) is easily affected by noise and results in the fluctuate frequency. And for large

earthquake excitation (EV13), the absolute acceleration is also strongly affected by input excitation in lower frequency and leads to the wrong result, therefore, the relative acceleration is used to calculate the pseudo-IF and the result shows the clear decrease of frequency in both directions.



Chapter 6. Conclusion



In this research, pattern-level data analysis technique (i.e. feature extraction using individual sensing signal) was used for structural damage detection and localization.

Wavelet decomposition of dynamic data using modified complex Morlet wavelet with variable central frequency (MCMW+VCF) was selected in this study. Based on the wavelet coefficients, several damage assessment algorithms were proposed:

1. Marginal spectrum
2. Central frequency
3. Pseudo-instantaneous frequency
4. Unwrapped phase
5. Novelty index
6. Correlation
7. Normalized component energy

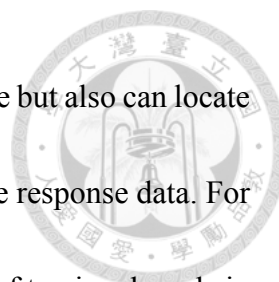
The earthquake as well as white noise response data of two lab experiments (twin-tower structure: damage in lower mode and two 3-story steel frames: nonlinear behavior) and the earthquake response data of two field experiments (Mingli elementary school and NCHU Civil & Environmental Engineering Building) were used for the verification of the proposed algorithms.



6.1 Research conclusions

In this study the pattern-level damage assessment techniques were developed. Based on Wavelet transform methodology, the modified Complex Morlet wavelet with variable central frequencies (MCMW+VCF) was proposed to extract the vibration features of a structure under either white noise excitation or seismic excitations. Then based on the extracted features, several damage assessment algorithms were proposed. The analysis results can be summarized as follows:

1. The wavelet transform using MCMW+VCF modified the representation of scalogram from general time-scale plane to the time-frequency plane, which had the advantages of identifying multi-degree-of-freedom system in frequency domain and can clearly identify the time-varying model frequencies of a structural system. Also, with the fixed scale parameter $a = 1$, the proposed wavelet transform simplified the choice of wavelet parameters and the reconstruction of signals.
2. The marginal spectrum of MCMW+VCF provided smoother spectrum in comparison to the fast Fourier transform, and the amplitude of the spectrum reflected the input energy. Based on the marginal spectrum, the frequency band can be chosen to extract signal features and then can be implemented to the damage assessment algorithms.
3. The central frequencies provided the identified dominant frequency of each floor and also a rough assessment of damage severity by only analyzing the output signal. For



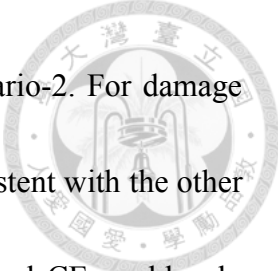
the twin-tower structure, the results can not only detect the damage but also can locate the damage for case of both white noise excitation and earthquake response data. For the two 3-story steel structures, the earlier changed of frequency of torsional mode in specimen-2 under earthquake excitation demonstrated the unsymmetrical setup of the structural system. The field application of two RC structures both showed the lowest frequencies in the mainshock of Chi-Chi earthquake and regain after retrofitted. Therefore, the central frequency can successfully perform the physical feature of the structure.

4. The identification of the pseudo-IF of scalogram using time-varying frequency band with ridge adjustment showed the success in detecting the sudden frequency shift from the study of twin tower structure, though the unapparent vibration of the sensing node made it hard to track the pseudo-IF in some cases. The pseudo-IF reflected the stable frequency in x-direction of the two 3-story structures even under severe earthquake excitation. For the filed experiments, the pseudo-IF was fluctuant because the acceleration response was easily affected by noise under small earthquake excitation. And for large earthquake excitation, because the absolute acceleration was strongly affected by input excitation in lower frequency and led to the wrong result, therefore, the relative acceleration was used and the result could successfully show the frequency decreasing with time. It has to mention that, with the check of pseudo-



IF using relative acceleration for lab experiments, the results were consistent with using absolute accelerations.

5. The extracted unwrapped phase is related to the speed of wave propagation in the structure, which can be applied to monitor the change of the structural system. If the structural member was damaged (or induced crack), the change of slope in the unwrapped phase can easily be identified. The results for lab and field experiments all showed the change of slope, which implied the change of dominant frequency within the selected frequency band. And the difference between floors could identify the damage location.
6. The novelty index (NIn) and correlation are both reference-based indices and can be used to identify the damage. These two indices can only utilize the response of white noise excitation because it compares the wavelet coefficients in scalogram. The application of two indices to twin-tower structure could detect and locate the damage for all three damage scenarios, but it showed the disadvantage of the indices that they cannot reflect the distance if the frequency shifts far away from the reference. For two 3-story steel frames, both indices could detect the stronger unsymmetrical behavior of specimen-2, but it showed the disadvantage of the correlation that it cannot compare two sets of data with same distribution, but different values.
7. The application of normalized component energy to twin-tower structure could detect



and locate the damage for damage scenario-1 and damage scenario-2. For damage scenario-3, it could locate the damage, but the trend did not consistent with the other 2 damage scenarios. For two 3-story steel frames, the normalized CE could only confirm the unsymmetrical setup of specimen-2, but could not detect the extent of damage. For the field application, because there was no record of ambient vibration, we could not check whether or not this index can be used to identify the damage.

Based on the proposed wavelet transform with MCMW+VCF, the results of the damage assessment algorithms reflected the change of a structure from its health condition and mostly showed the consistency. It is recommended that using central frequency and novelty index for ambient vibration response, and unwrapped phase and pseudo-IF for earthquake excitation. These methods can be used as the effective tools for structural health monitoring.

6.2 Future work

1. The proposed wavelet transform is based on the fixed scale parameter $a = 1$, if another fixed number of scale is used, there will be multiple combinations of time and frequency resolution can be chosen on the requirements for both resolutions without at the expense of either of them.
2. The identification of pseudo-IF using time-varying frequency band with ridge

adjustment showed fluctuation in some cases because the ridge was influenced by noise, input excitation, and other modes. The combination of wavelet transform and Recursive Least Square (RSL) algorithm may solve this problem and provide a better result.



References



- [1] Amezquita-Sanchez, J. P., & Adeli, H. (2015). Synchrosqueezed wavelet transform-fractality model for locating, detecting, and quantifying damage in smart highrise building structures. *Smart Materials and Structures*, 24(6).
- [2] Balafas, K., & Kiremidjian, A. S. (2015). Development and validation of a novel earthquake damage estimation scheme based on the continuous wavelet transform of input and output acceleration measurements. *Earthquake Engineering & Structural Dynamics*, 44(4), 501-522.
- [3] Basu, B., & Gupta, V. K. (1997). Non-stationary seismic response of MDOF systems by wavelet transform. *Earthquake Engineering & Structural Dynamics*, 26(12), 1243-1258.
- [4] Chao, S. H., & Loh, C. H. (2013). Vibration-based damage identification of reinforced concrete member using optical sensor array data. *Structural Health Monitoring*, 12(5-6), 397-410.
- [5] Chen, B., Chen, Z. w., Wang, G. j., & Xie, W. p. (2014). Damage Detection on Sudden Stiffness Reduction Based on Discrete Wavelet Transform. *The Scientific World Journal*, 16.
- [6] Chopra, S., & Marfurt, K. J. (2015). *Choice of mother wavelets in CWT spectral decomposition*. Paper presented at the SEG Technical Program Expanded Abstracts.



- [7] Feldman, M. (2011). Hilbert transform in vibration analysis. *Mechanical Systems and Signal Processing*, 25(3), 735-802.
- [8] Goggins, J., Basu, B., Broderick, B. M., & Elghazouli, A. Y. (2007). Investigation of the seismic response of braced frames using wavelet analysis. *Structural Control and Health Monitoring*, 14(4), 627-648.
- [9] Guo, Y., & Kareem, A. (2015). System Identification through Nonstationary Response: Wavelet and Transformed Singular Value Decomposition-Based Approach. *Journal of Engineering Mechanics*, 141(7).
- [10] Hsueh, W., & Loh, C. H. (2017). Damage detection of structures by wavelet analysis: application to seismic response of steel frames. *Proc. SPIE 10168, Sensors and Smart Structures Technologies for Civil, Mechanical, and Aerospace Systems 2017*.
- [11] Kijewski, T., & Kareem, A. (2003). Wavelet Transforms for System Identification in Civil Engineering. *Computer-Aided Civil and Infrastructure Engineering*, 18(5), 339-355.
- [12] Klepka, A., & Uhl, T. (2014). Identification of modal parameters of non-stationary systems with the use of wavelet based adaptive filtering. *Mechanical Systems and Signal Processing*, 47(1-2), 21-34.
- [13] Lardies, J., & Ta, M. N. (2005). A wavelet-based approach for the identification of damping in non-linear oscillators. *International Journal of Mechanical Sciences*,



- 47(8), 1262-1281.
- [14] Lee, S. G., Yun, G. J., & Shang, S. (2014). Reference-free damage detection for truss bridge structures by continuous relative wavelet entropy method. *Structural Health Monitoring, 13*(3), 307-320.
- [15] Li, C., & Liang, M. (2012). A generalized synchrosqueezing transform for enhancing signal time-frequency representation. *Signal Processing, 92*(9), 2264-2274.
- [16] Nair, K. K., & Kiremidjian, A. S. (2009). *A Damage Detection Algorithm Using the Morlet Wavelet Transform*. Stanford University.
- [17] Noh, H. Y., Nair, K. K., Lignos, D. G., & Kiremidjian, A. S. (2011). Use of Wavelet-Based Damage-Sensitive Features for Structural Damage Diagnosis Using Strong Motion Data. *Journal of Structural Engineering, 137*(10), 1215-1228
- [18] Robertson, A. N., Farrar, C. R., & Sohn, H. (2003). Singularity detection for structural health monitoring using Holder exponents. *Mechanical Systems and Signal Processing, 17*(6), 1163-1184.
- [19] Staszewski, W. J. (1997). Identification of damping in MDOF systems using time-scale decomposition. *Journal of Sound and Vibration, 203*(2), 283-305.
- [20] Tarinejad, R., & Damadipour, M. (2014). Modal identification of structures by a novel approach based on FDD-wavelet method. *Journal of Sound and Vibration, 333*(3), 1024-1045.

[21] Thakur, G., Brevdo, E., Fučkar, N. S., & Wu, H. T. (2013). The Synchrosqueezing algorithm for time-varying spectral analysis: Robustness properties and new paleoclimate applications. *Signal Processing*, 93(5), 1079-1094.

[22] Todorovska, M. I. (2001). *Estimation of Instantaneous Frequency of Signals Using the Continuous Wavelet Transform*. University of Southern California, report CE 01-07.



Tables



Table 3-1 Test protocol of twin-tower steel structure

Damage scenario-1														
CASE	WN1	EQ1	WN2	EQ2	WN3	EQ3	WN4	EQ4	WN5	EQ5	WN6	EQ6	WN7	EQ7
PGA(gal)	50	200	50	300	50	450	50	600	50	750	50	900	50	1050
Damage scenario-2 & Damage scenario-3														
CASE	WN1	EQ1	WN2	EQ2	WN3	EQ3	WN4	EQ4	WN5	EQ5				
PGA(gal)	50	200	50	400	50	600	50	800	50	1000				

Table 3-2 Test protocol of two three-story steel frames

Specimen-1 & Specimen-2														
CASE	WN1	WN2	EQ1	WN3	EQ2	WN4	EQ3	WN5	EQ4	WN6	EQ5	WN7	EQ6	WN8
PGA(gal)	50	50	100	50	250	50	400	50	550	50	700	50	850	50
CASE	EQ7	WN9	EQ8	WN10	EQ9	WN11								
PGA(gal)	1000	50	1150	50	1300	50								

Figures

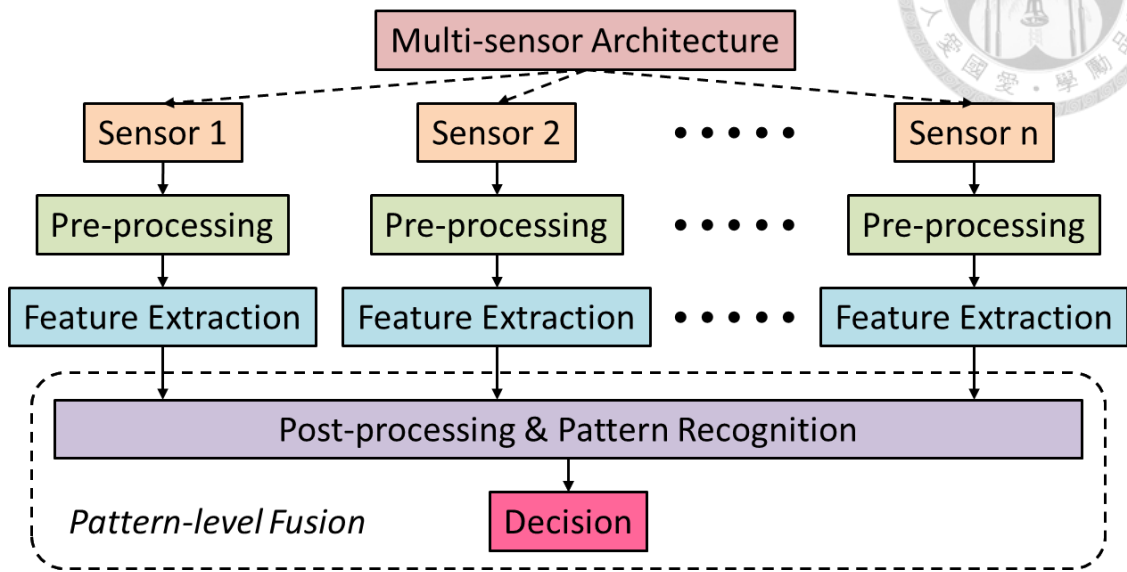


Figure 1-1 The flowchart of the pattern-level feature extraction technique

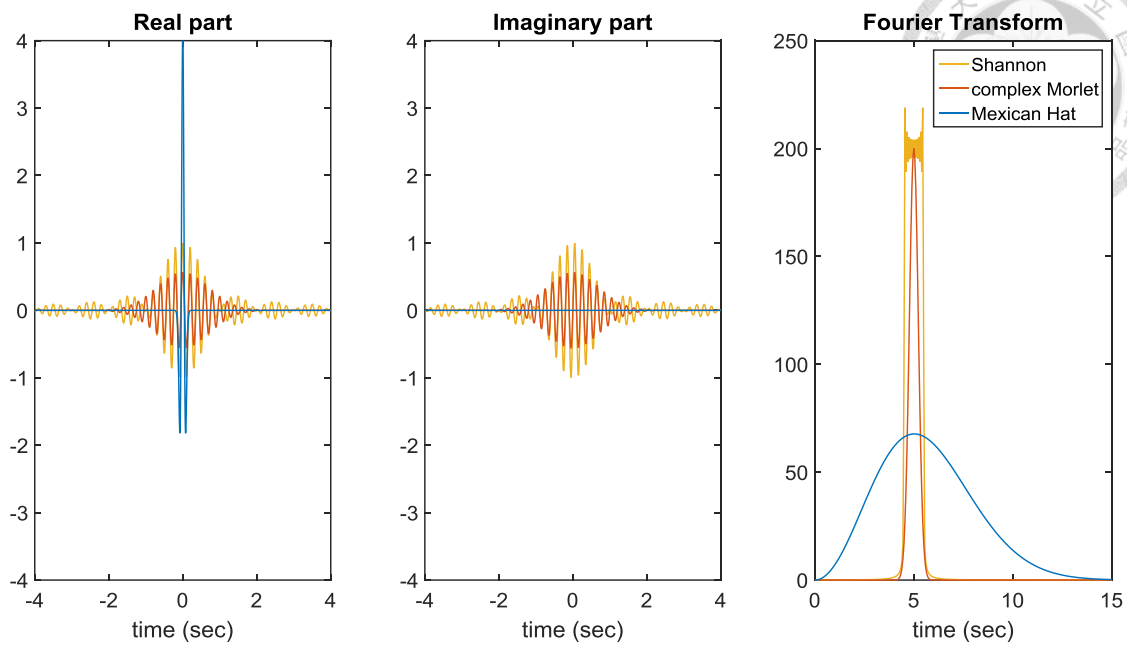


Figure 2-1 The shapes of Shannon, Complex Morlet, and Mexican Hat wavelets in time and frequency domain (All the wavelets have the same analysis frequency of 5 Hz)

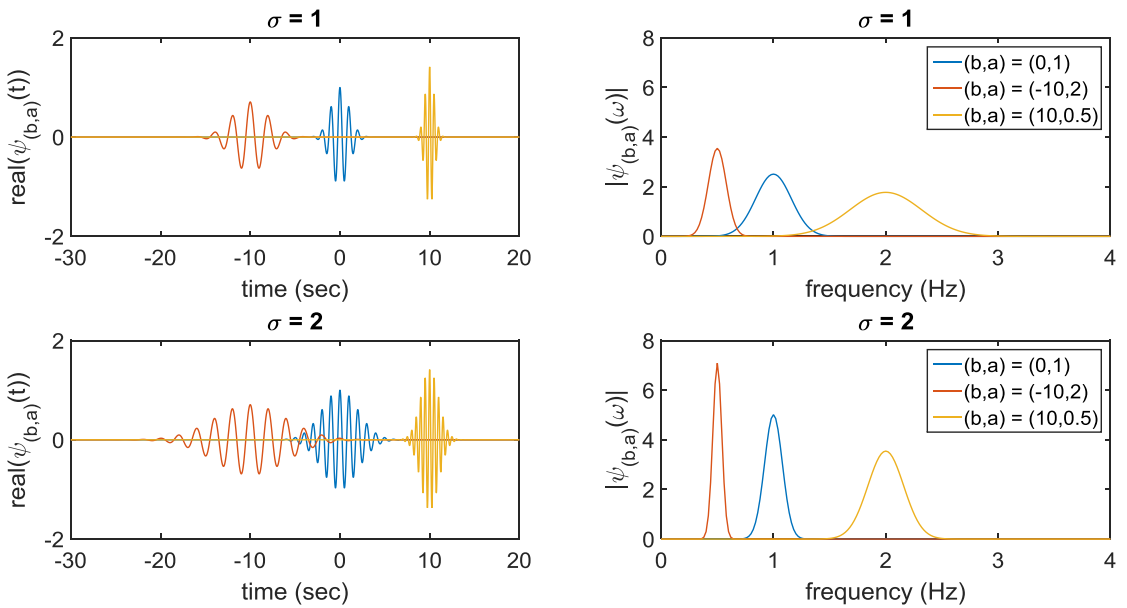


Figure 2-2 The shape of complex Morlet wavelet in different parameters a and b (fixed $\omega_0 = 1$ Hz) with $\sigma = 1$ (top) and $\sigma = 2$ (bottom) in time and frequency domain

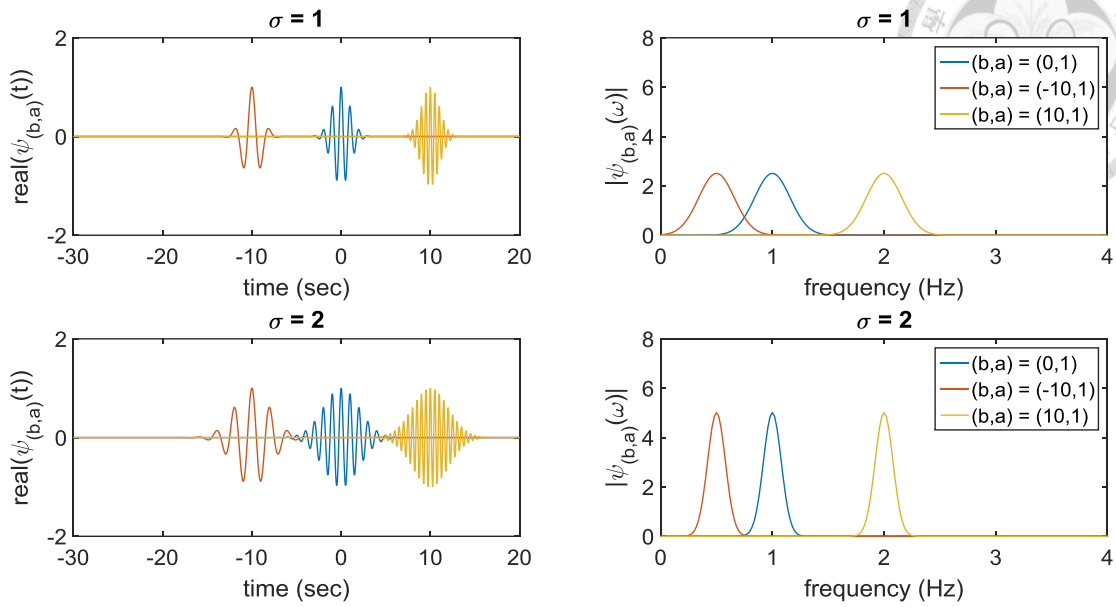


Figure 2-3 The shape of complex Morlet wavelet in different central frequency (fixed $a = 1$) with $\sigma = 1$ (top) and $\sigma = 1$ (bottom) in time and frequency domain

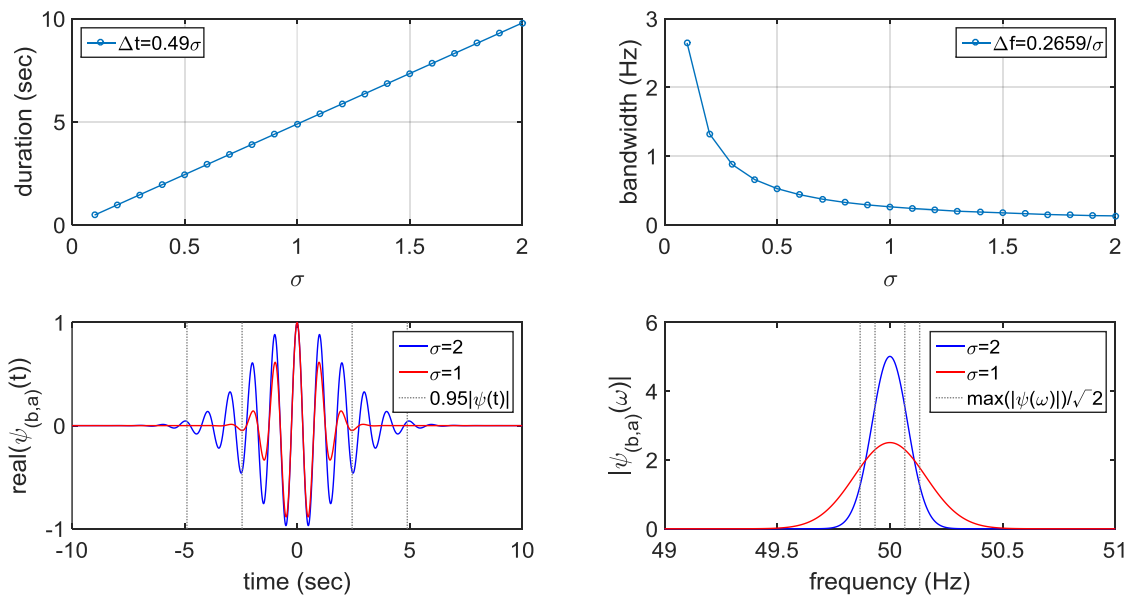


Figure 2-4 The relationship between σ , time duration (top left) and frequency bandwidth (top right). The definition of time duration is $0.95|\psi(t)|$ (bottom left) and

frequency bandwidth is $\max(|\psi(\omega)|)/\sqrt{2}$ (bottom right)

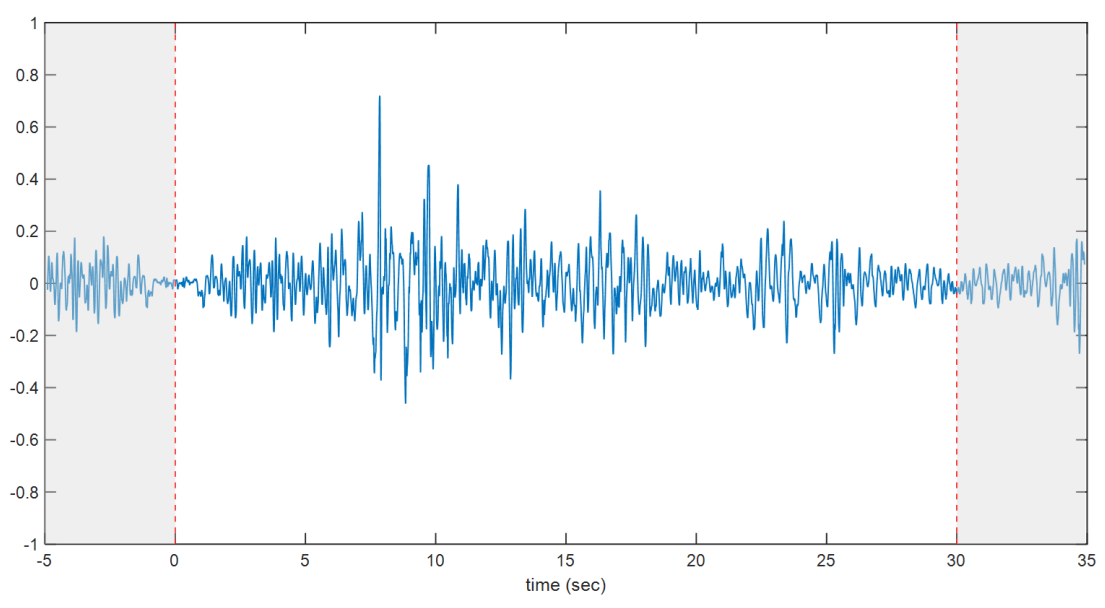
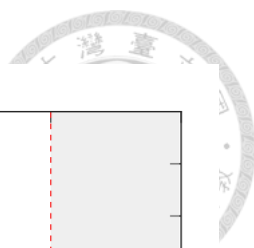


Figure 2-5 Signal padding operation for using $\sigma = 2$

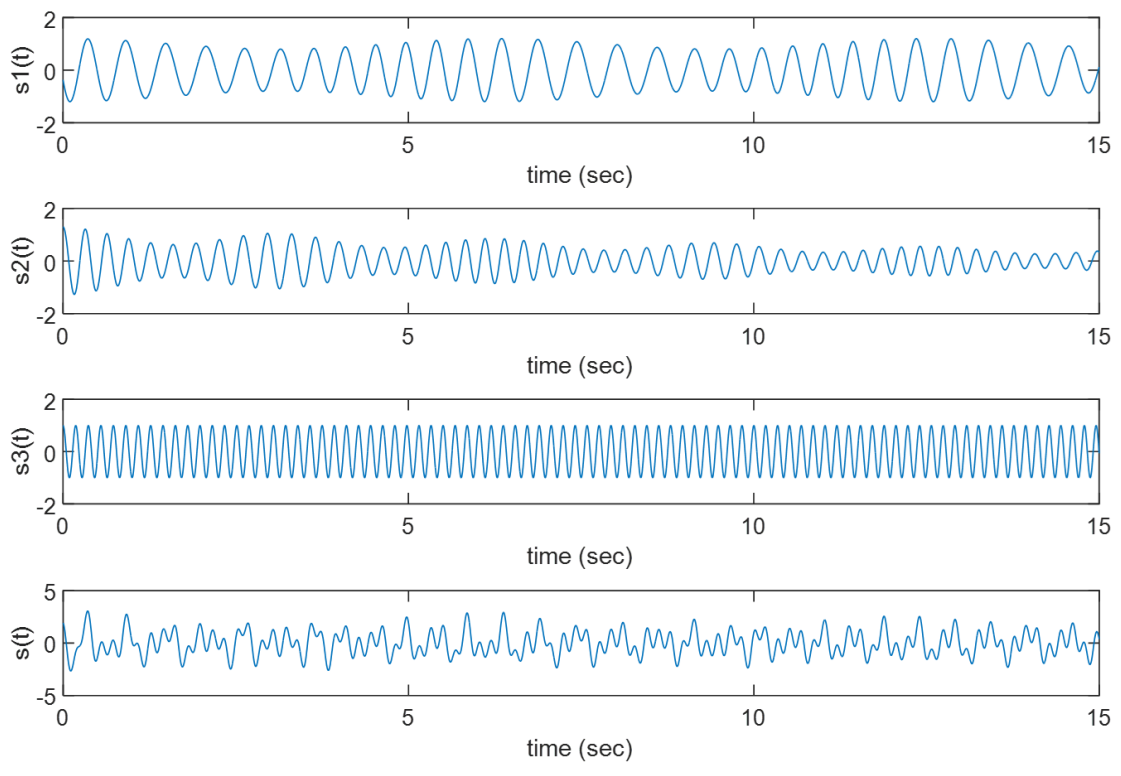


Figure 2-6 The wave form of the simulated nonlinear time functions

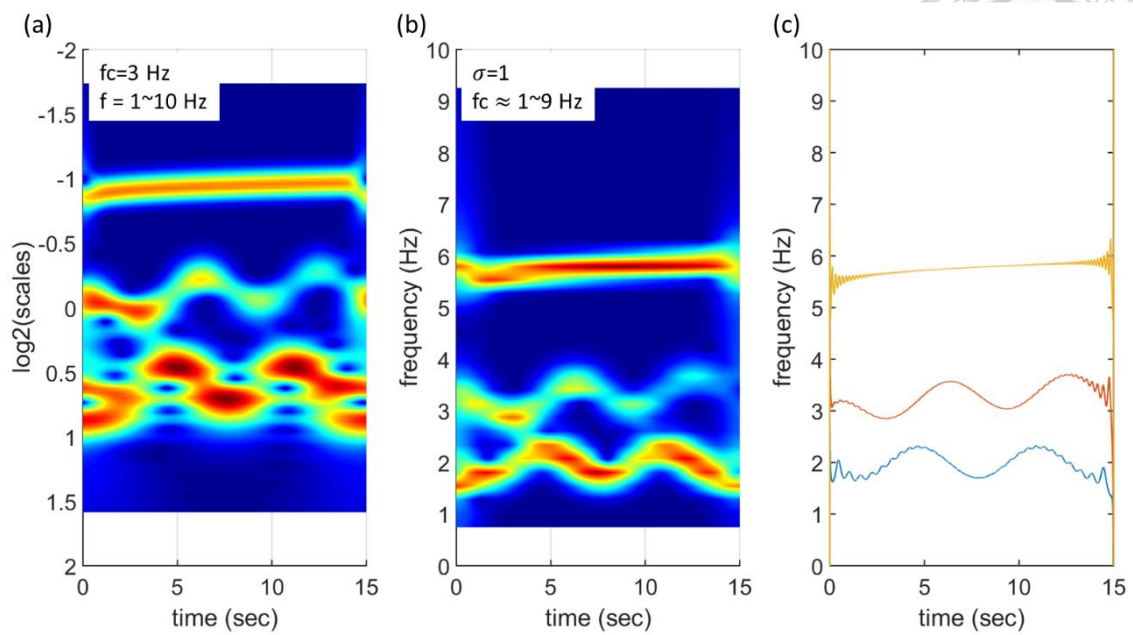


Figure 2-7 Plot time-frequency analysis of the test signal $s(t)$; (a) using general CWT, (b) using MCMW+VCF, (c) the instantaneous frequency using Hilbert transform of original signal $s_1(t)$, $s_2(t)$, and $s_3(t)$



Figure 2-8 One-story two-bay reinforced concrete frame

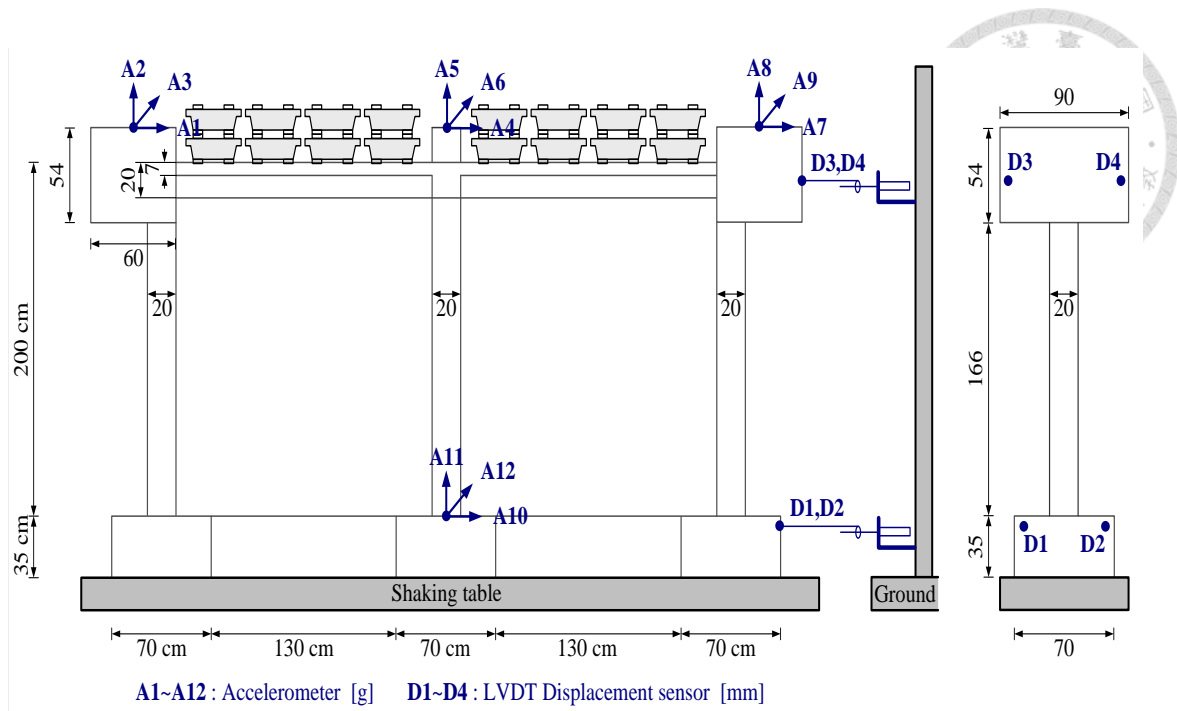


Figure 2-9 Dimension of RC frame

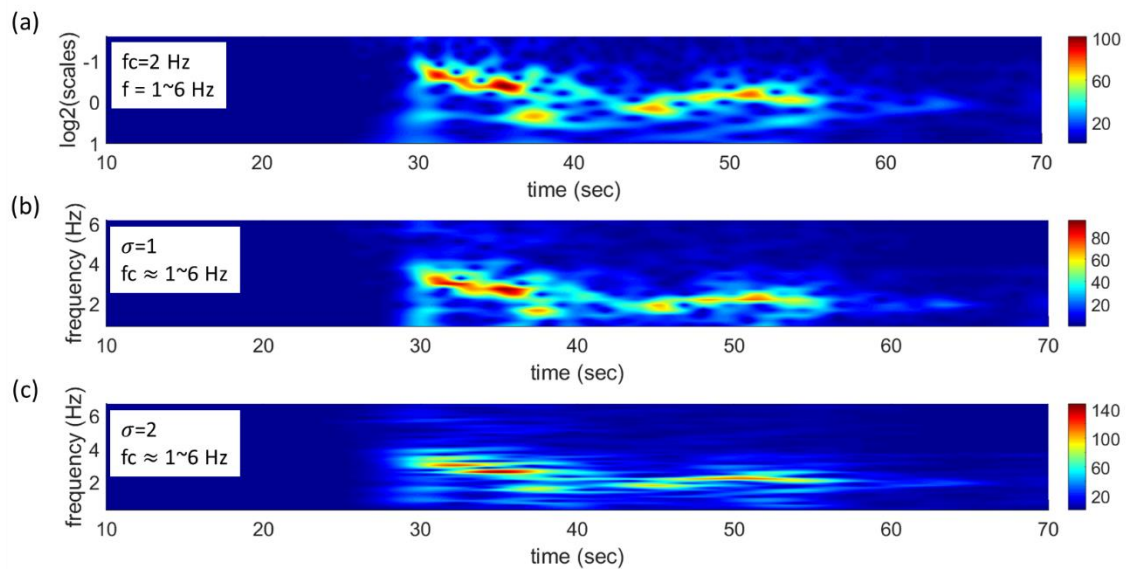


Figure 2-10 The scalogram of RC frame (a) using general CWT, (b) using MCMW+VCF with $\sigma=1$, (c) using MCMW+VCF with $\sigma=2$

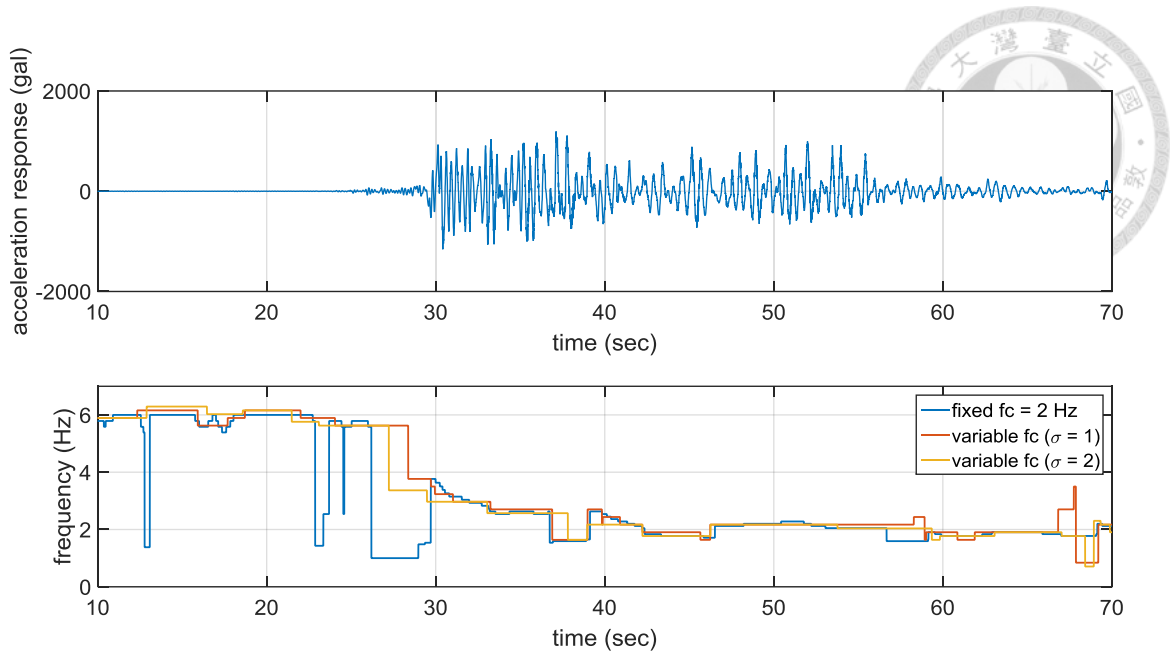


Figure 2-11 The acceleration of RC frame (top) and the ridge calculated from different wavelet transform (bottom)

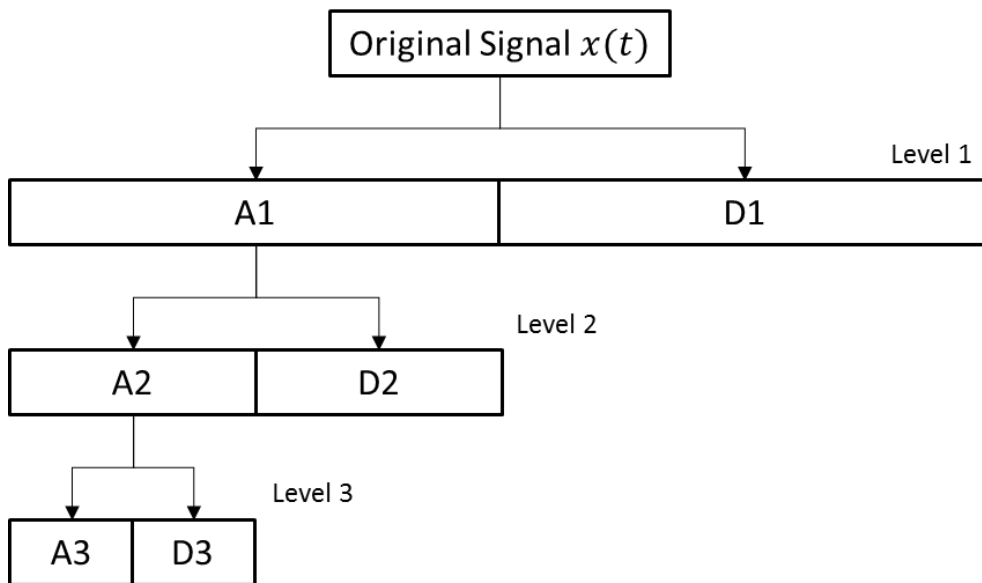


Figure 2-12 Discrete wavelet transform tree

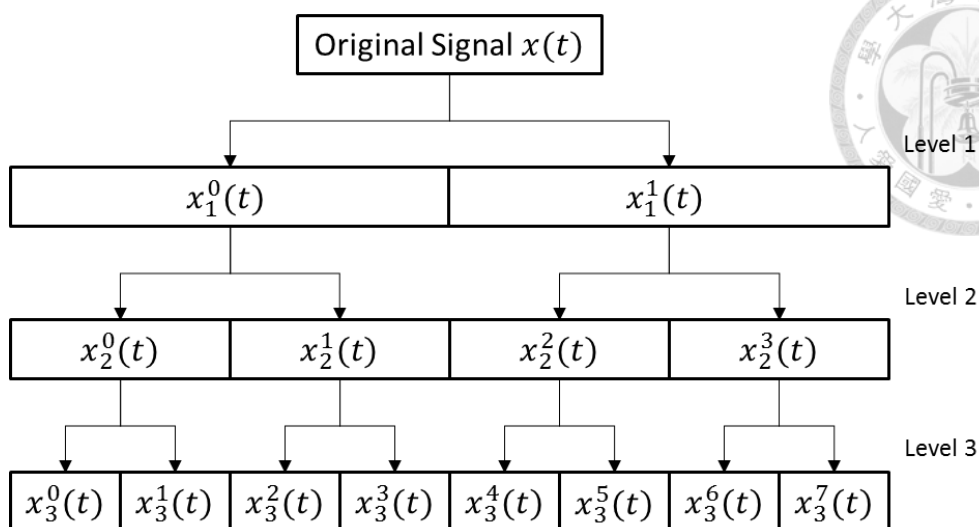


Figure 2-13 Wavelet packet transform tree

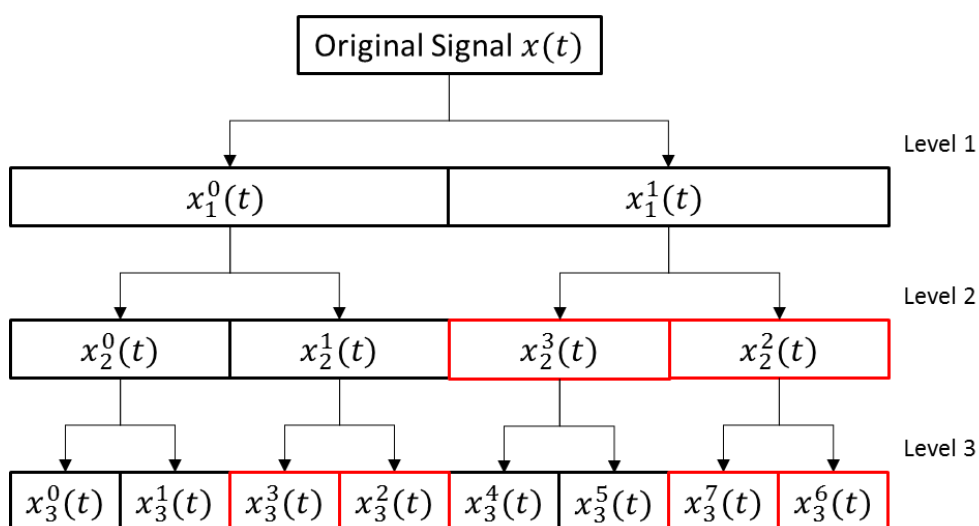


Figure 2-14 Wavelet packet transform tree (in Paley order)



Figure 3-1 The twin-tower steel structure

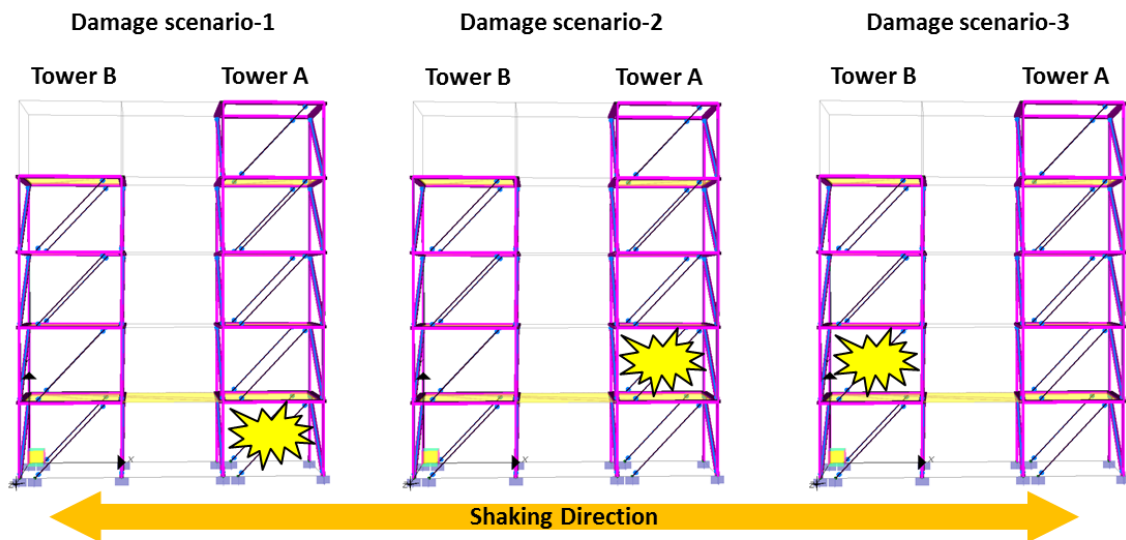


Figure 3-2 Damage scenario-1, 2, and 3 of the twin-tower steel structure

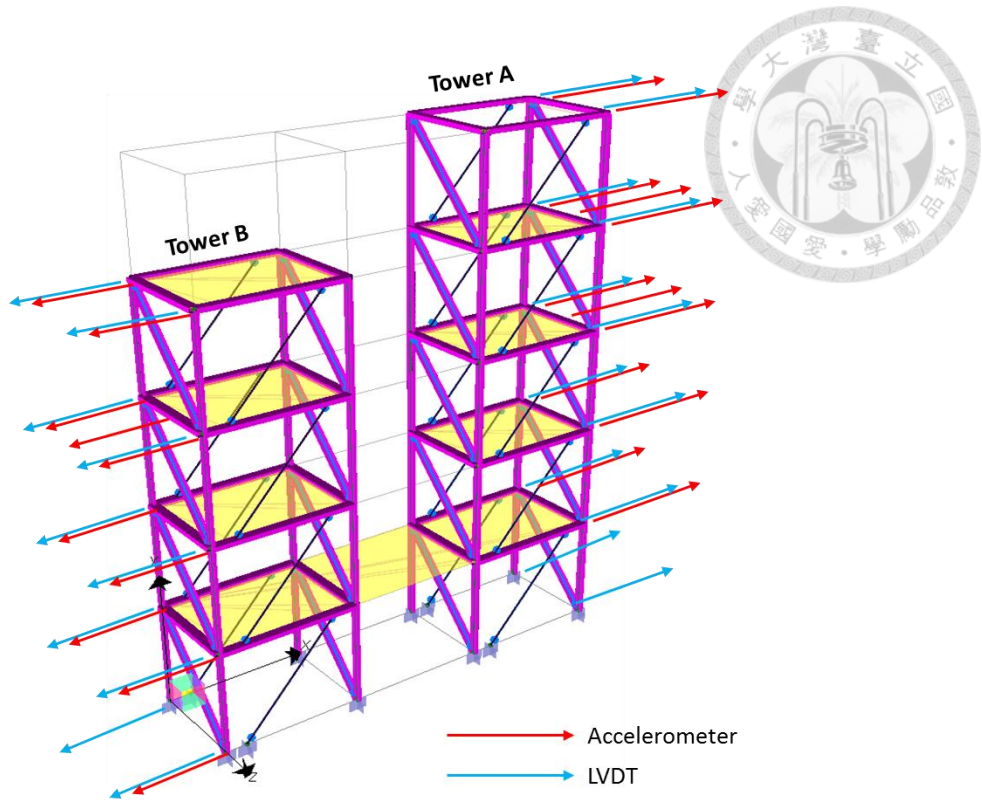


Figure 3-3 Sensor instrumentations for the twin-tower steel structure

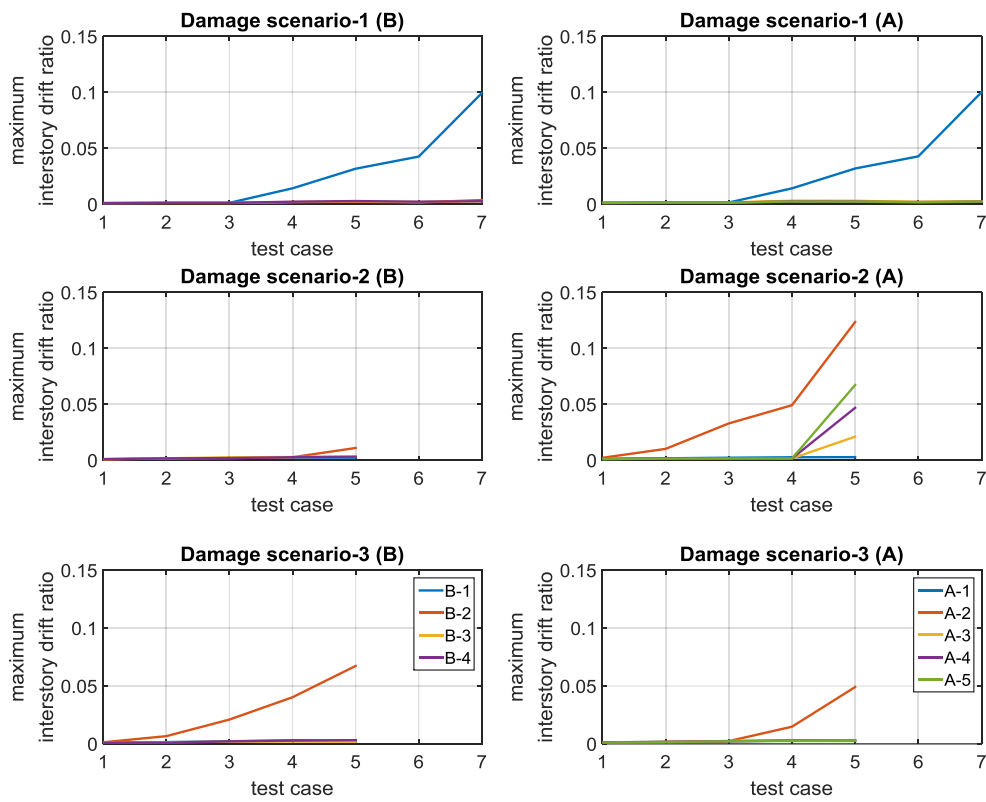


Figure 3-4 The maximum interstory drift ratio for twin-tower steel structure

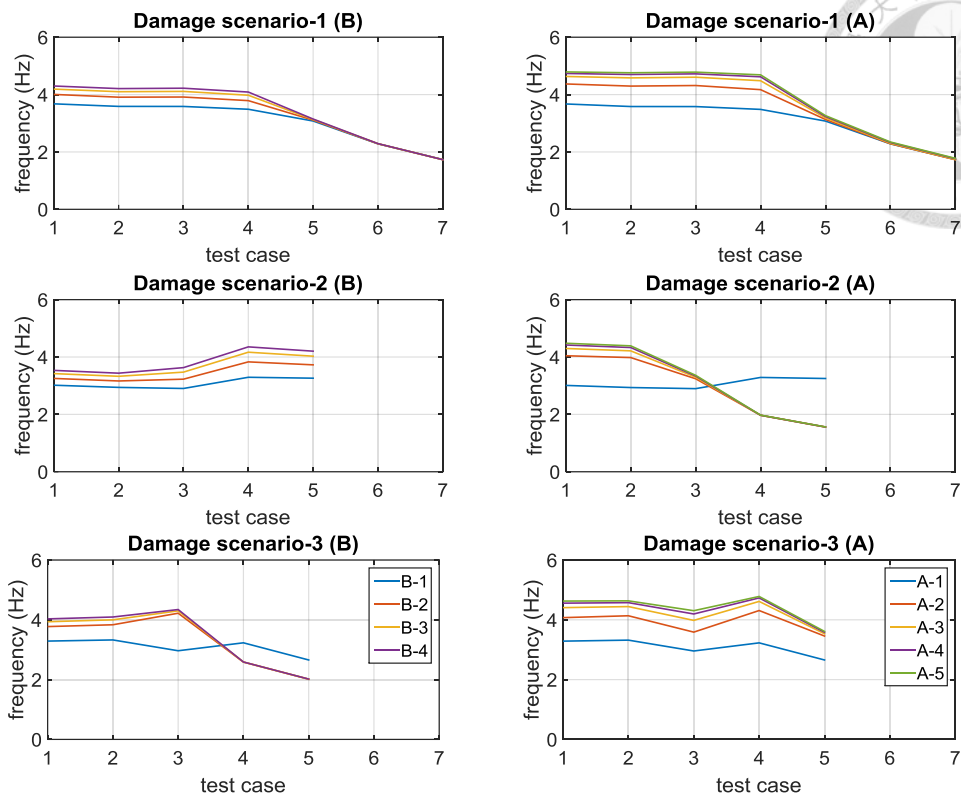


Figure 3-5 The central frequencies for twin-tower steel structure (w.r.t. frequency band: 0~6 Hz)

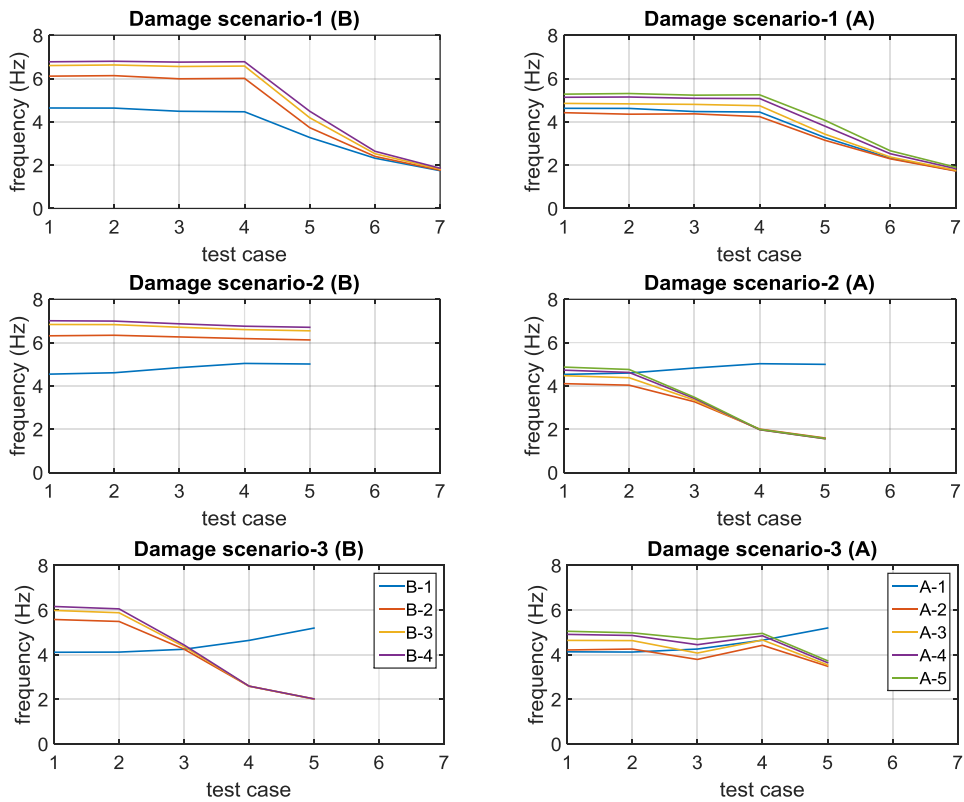


Figure 3-6 The central frequencies for twin-tower steel structure (w.r.t. frequency band: 0~10 Hz)

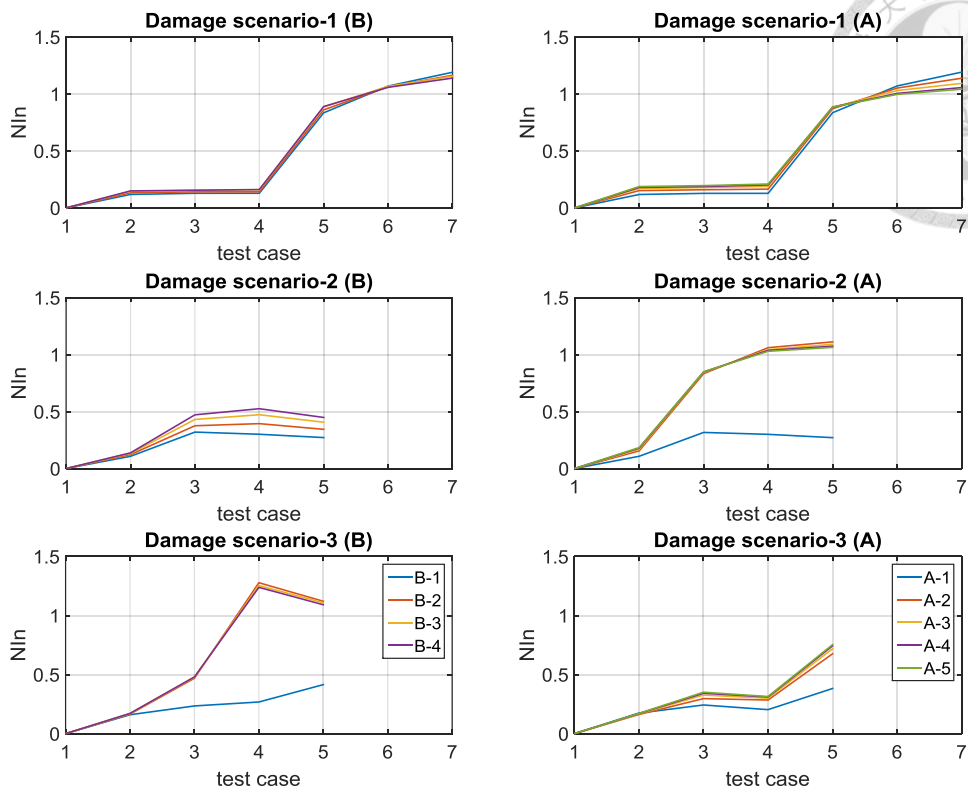


Figure 3-7 The Novelty index for twin-tower steel structure (w.r.t. frequency band: 0~6 Hz)

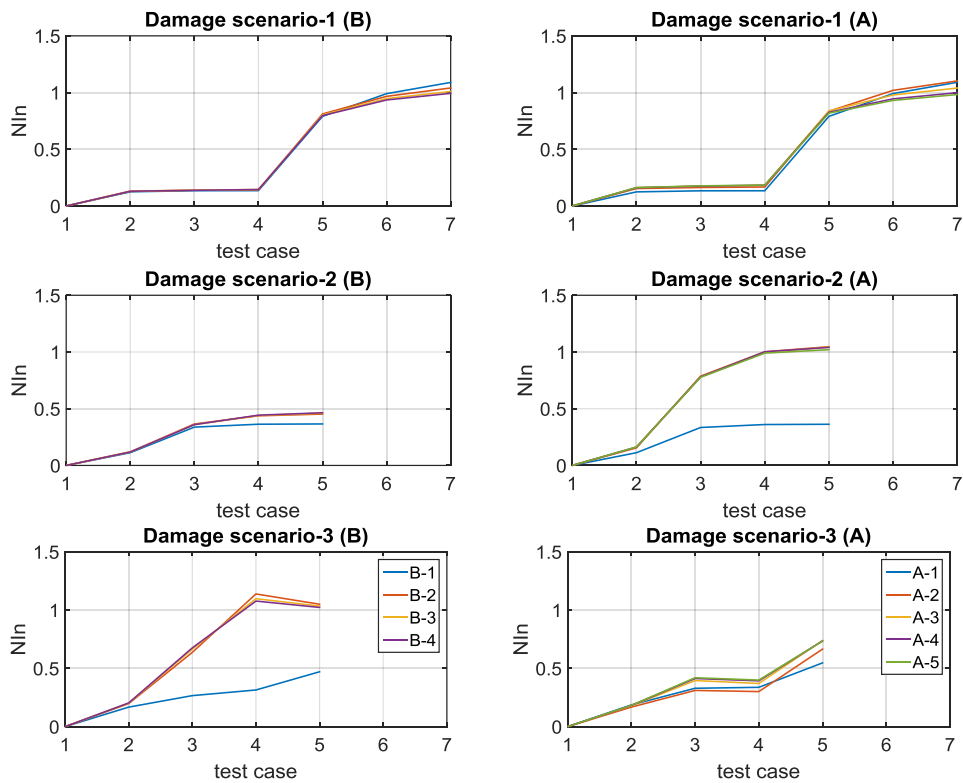


Figure 3-8 The Novelty index for twin-tower steel structure (w.r.t. frequency band: 0~10 Hz)

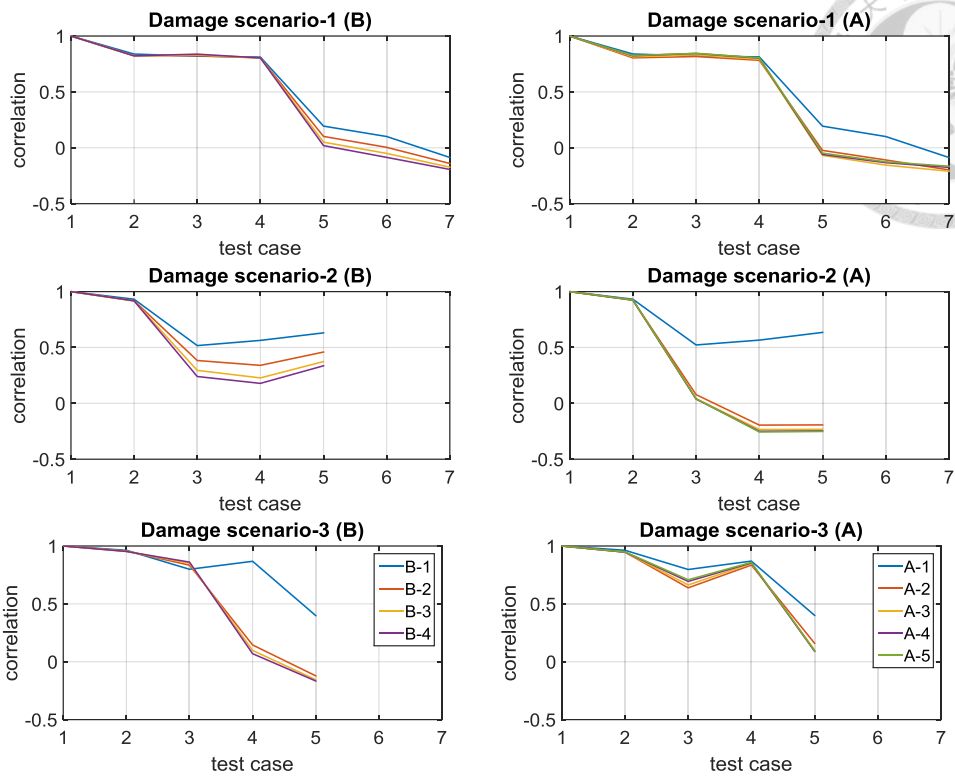


Figure 3-9 The correlation for twin-tower steel structure (w.r.t. frequency band: 0~6 Hz)

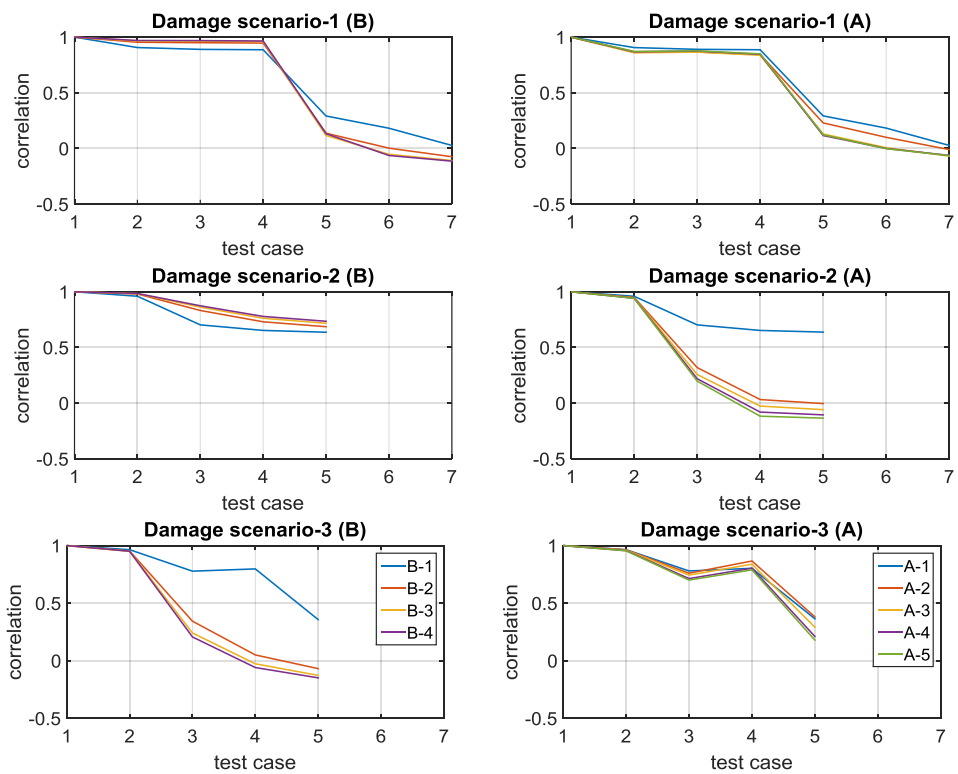


Figure 3-10 The correlation for twin-tower steel structure (w.r.t. frequency band: 0~10 Hz)

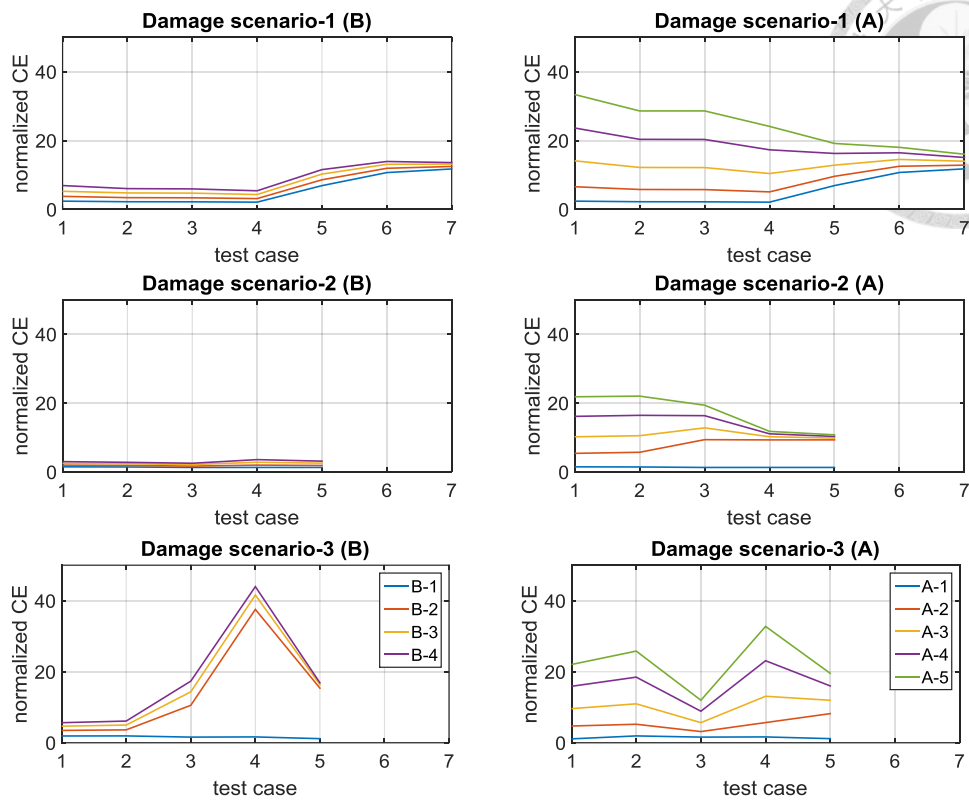


Figure 3-11 The normalized CE for twin-tower steel structure (w.r.t. frequency band: 0~6 Hz)

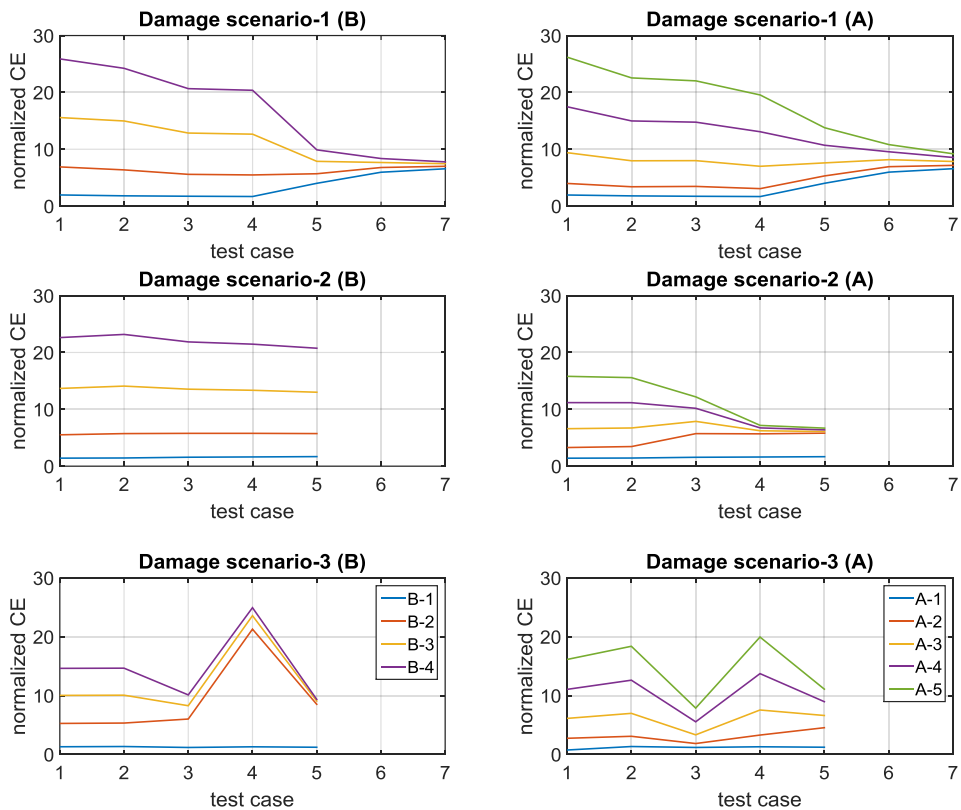


Figure 3-12 The normalized CE for twin-tower steel structure (w.r.t. frequency band: 0~10 Hz)

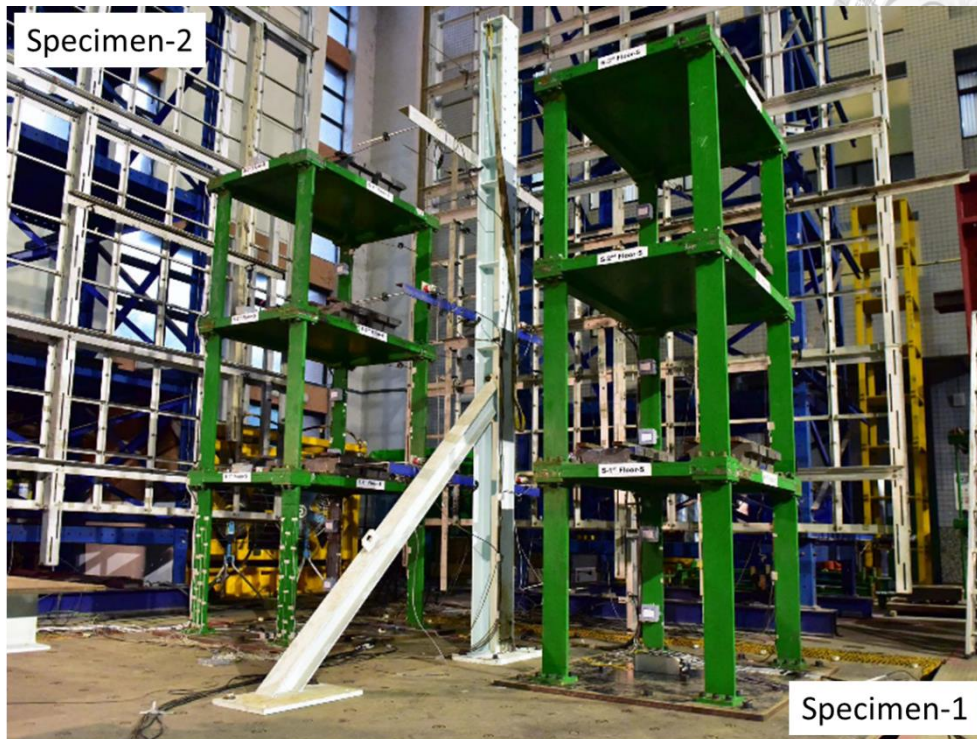


Figure 3-13 Two three-story steel frames

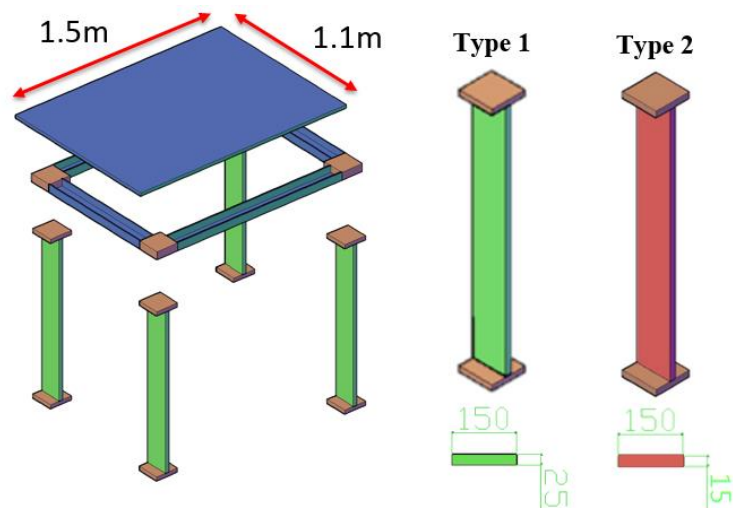


Figure 3-14 Components of each floor for two three-story steel frames

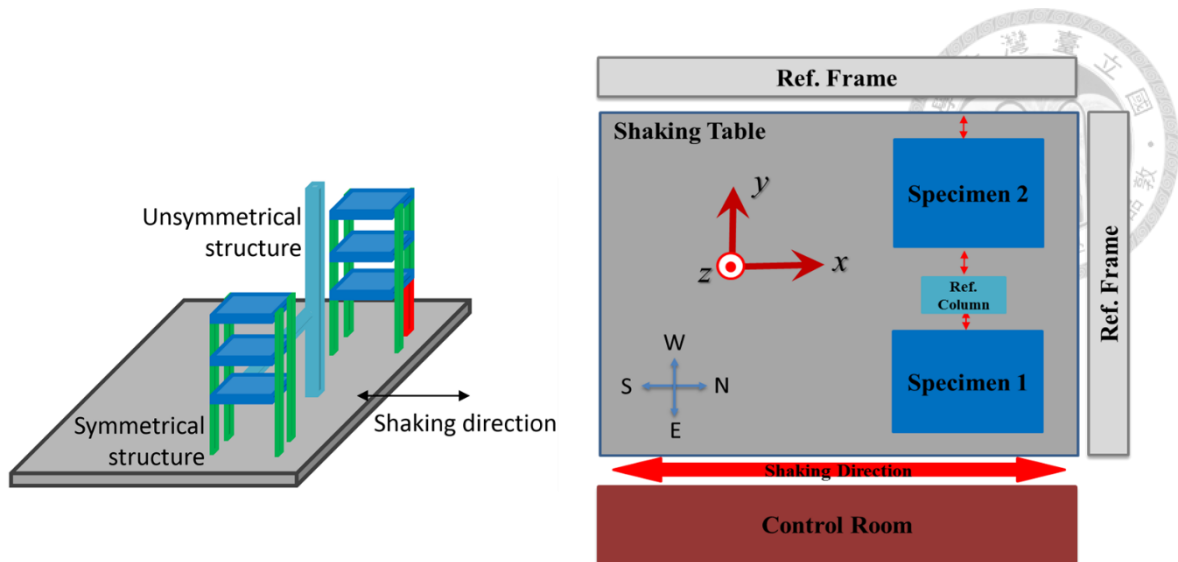


Figure 3-15 Configuration of the two three-story steel frames

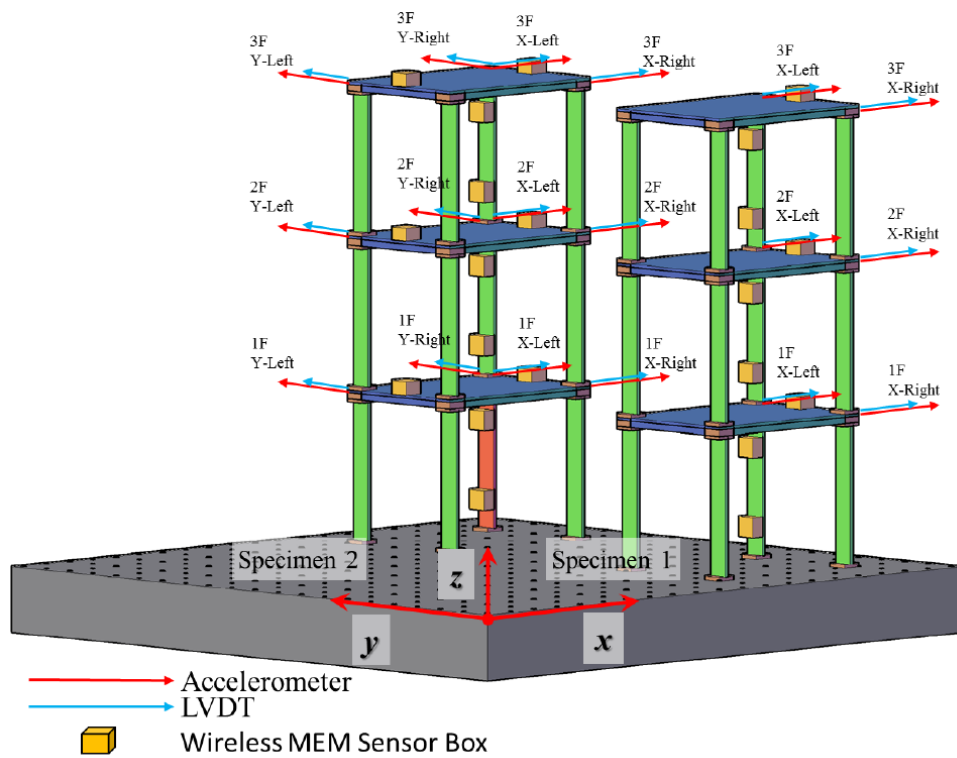


Figure 3-16 Sensor instrumentations for the two three-story steel frames

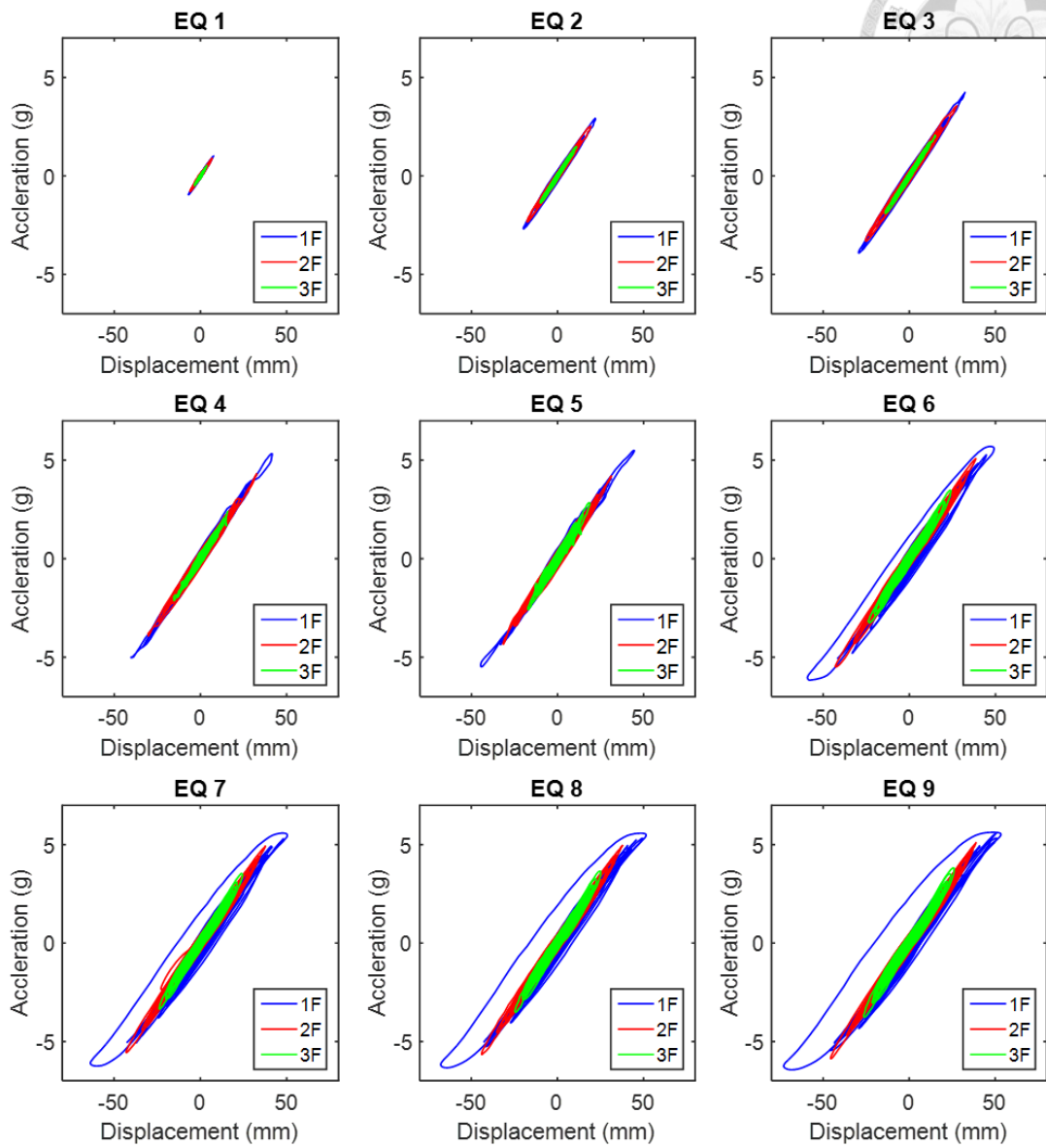


Figure 3-17 Hysteresis loop of specimen-1

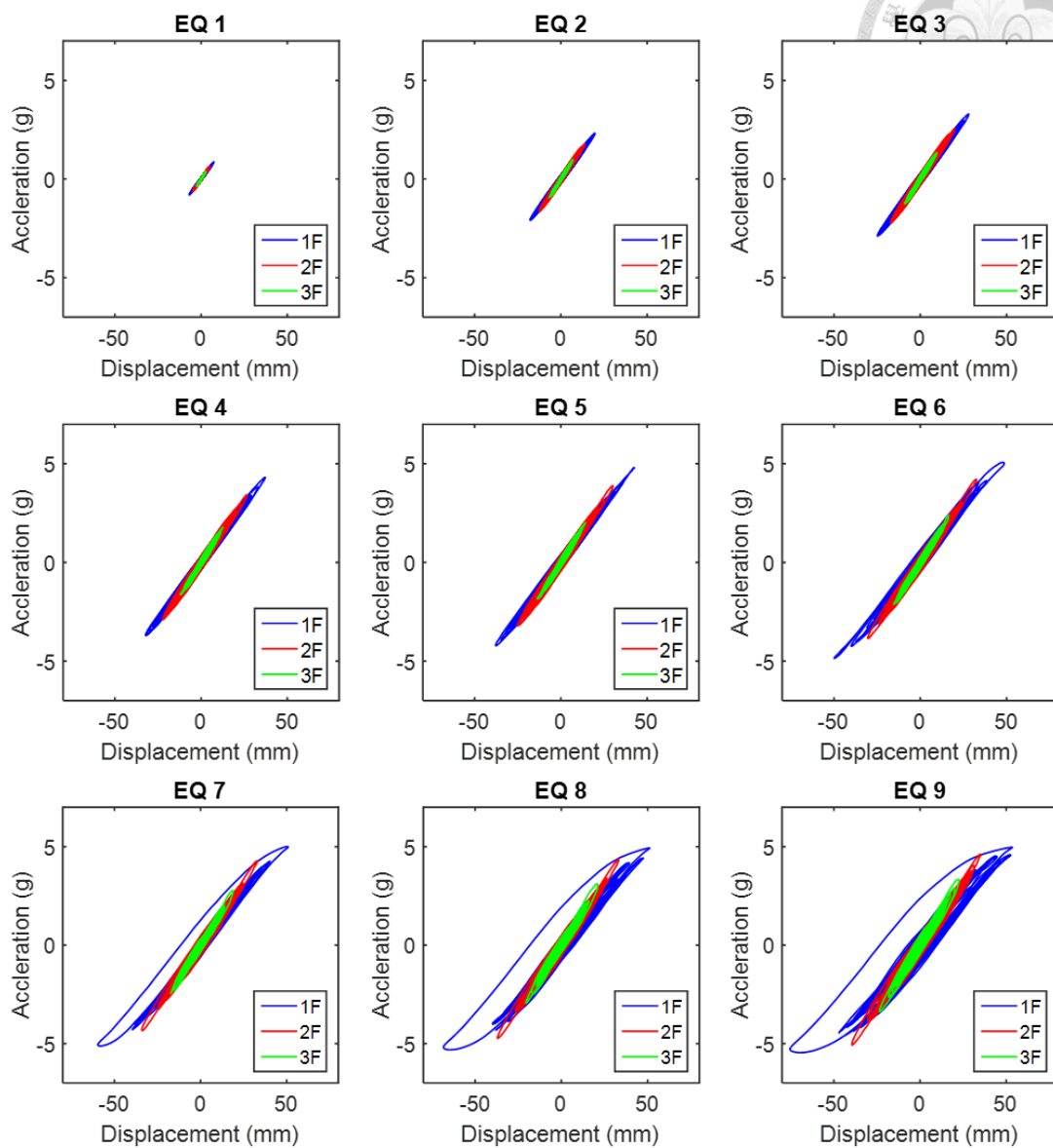


Figure 3-18 Hysteresis loop of specimen-2

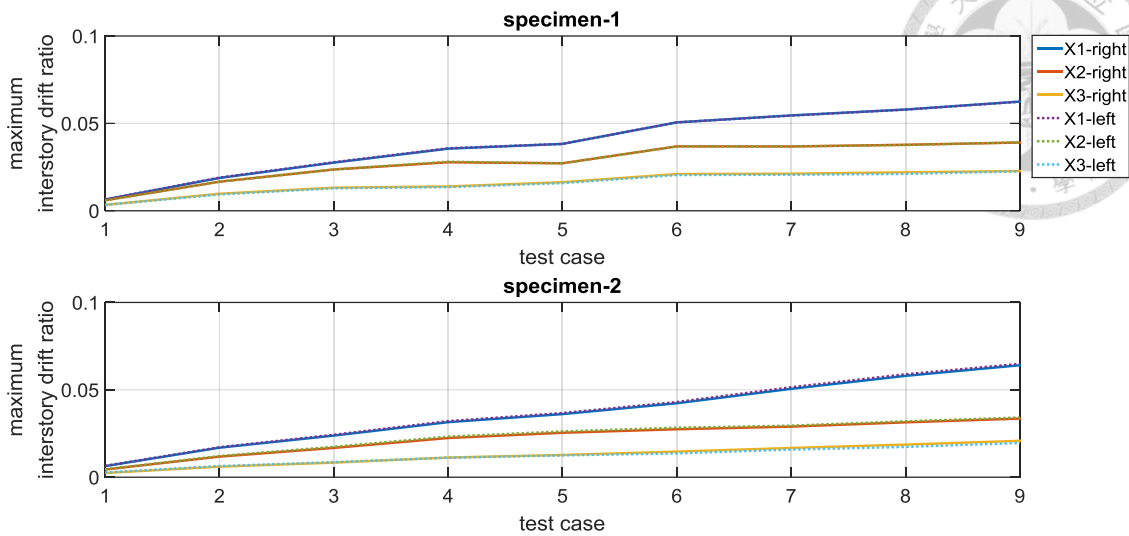


Figure 3-19 The maximum interstory drift ratio for two three-story steel frames

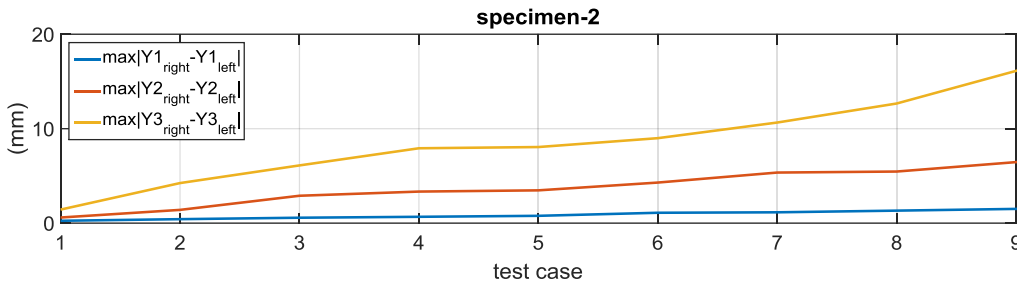


Figure 3-20 The maximum story drift for specimen-2

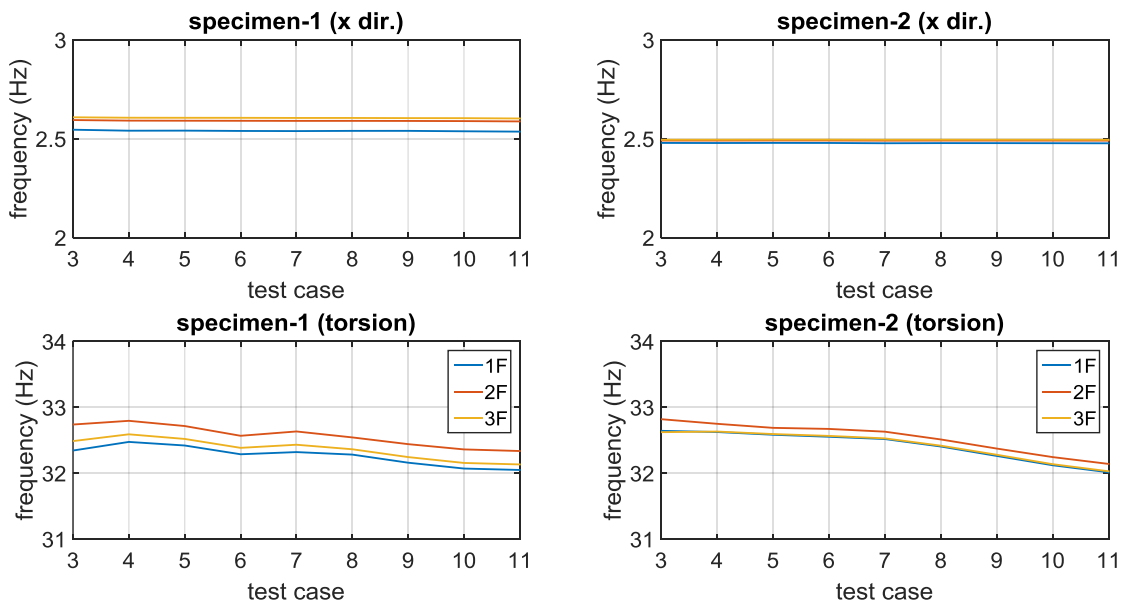


Figure 3-21 The central frequency for two three-story steel frames (w.r.t. x-dir. frequency band: 0~5 Hz, torsional dir. frequency band 25~40 Hz)

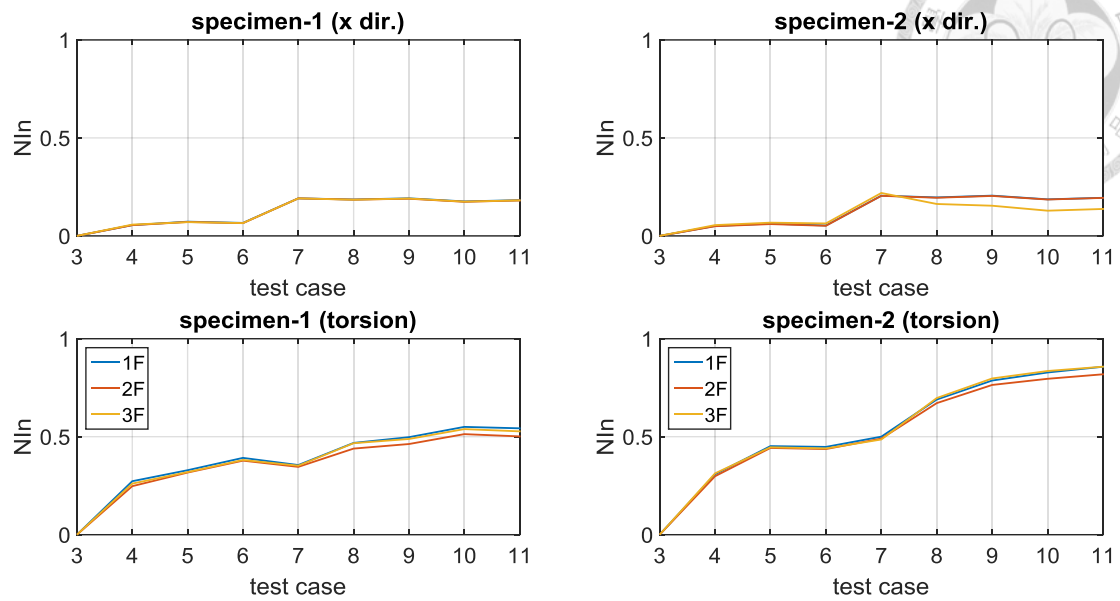


Figure 3-22 The Novelty index for two three-story steel frames (w.r.t. x-dir. frequency band: 0~5 Hz, torsional dir. frequency band 25~40 Hz)

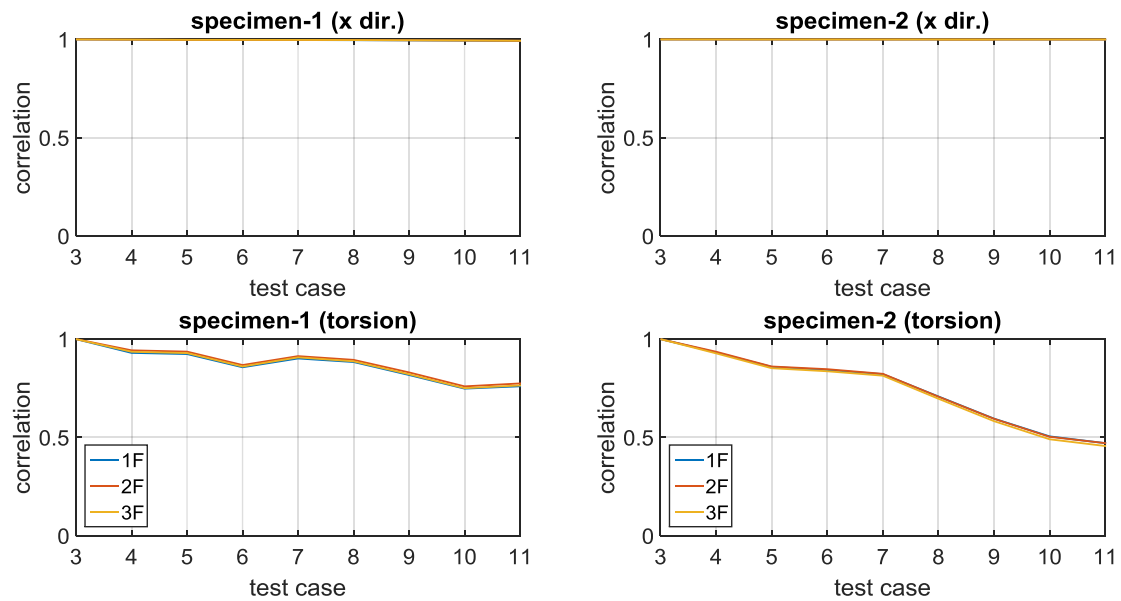


Figure 3-23 The correlation for two three-story steel frames (w.r.t. x-dir. frequency band: 0~5 Hz, torsional dir. frequency band 25~40 Hz)

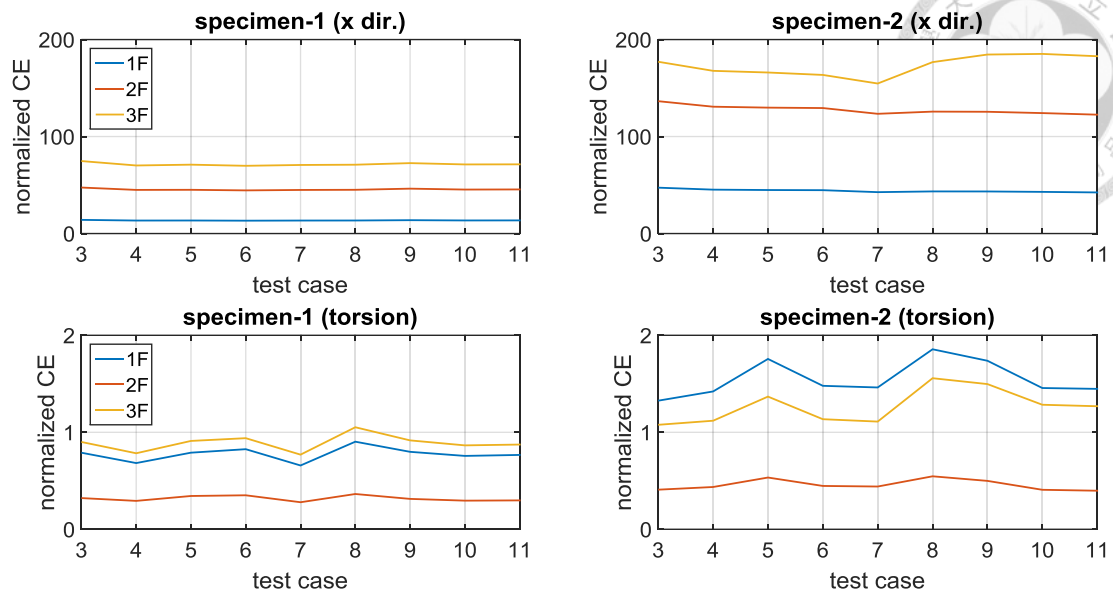


Figure 3-24 The normalized CE for two three-story steel frames (w.r.t. x-dir. frequency band: 0~5 Hz, torsional dir. frequency band 25~40 Hz)

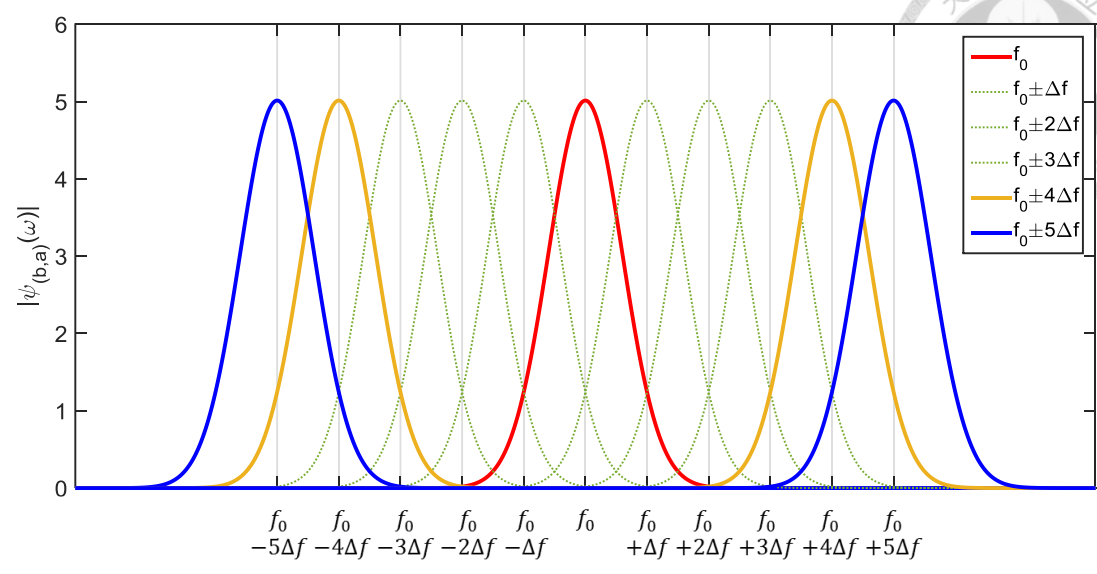
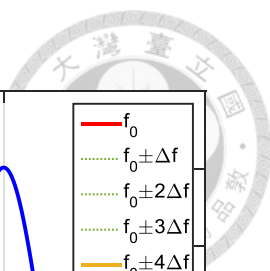


Figure 4-1 The analysis frequency band of complex Morlet wavelet

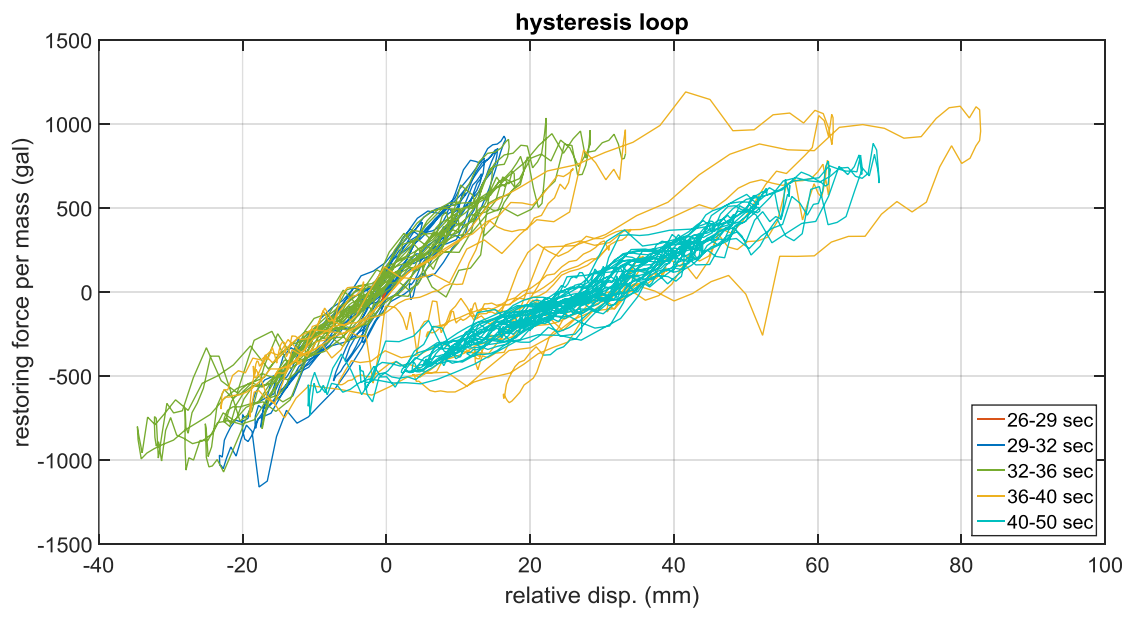


Figure 4-2 The hysteresis loop for RC frame

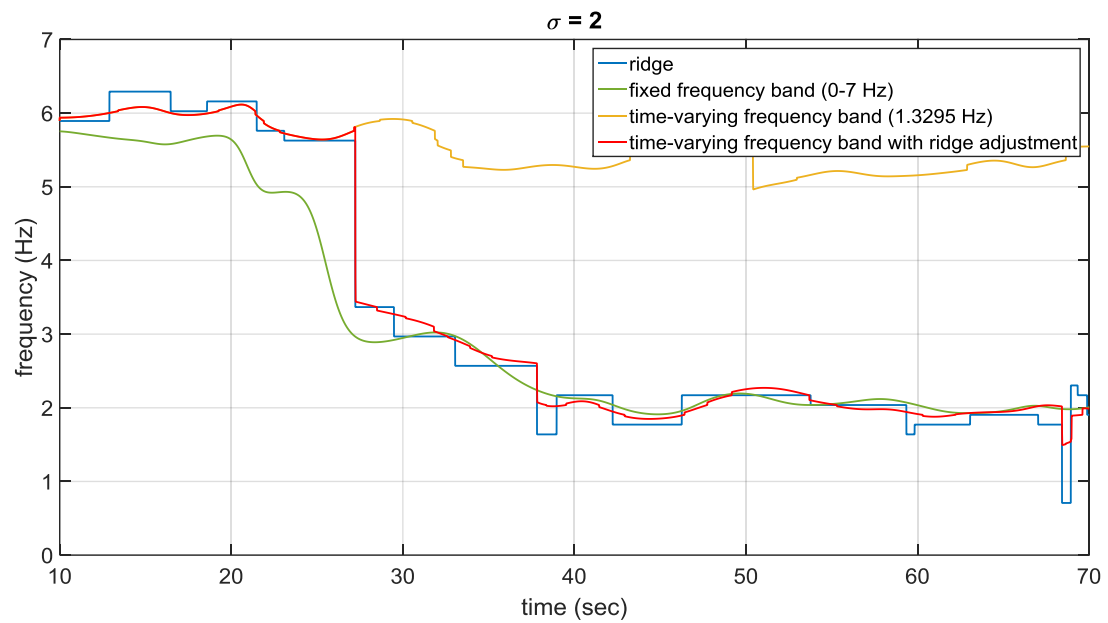
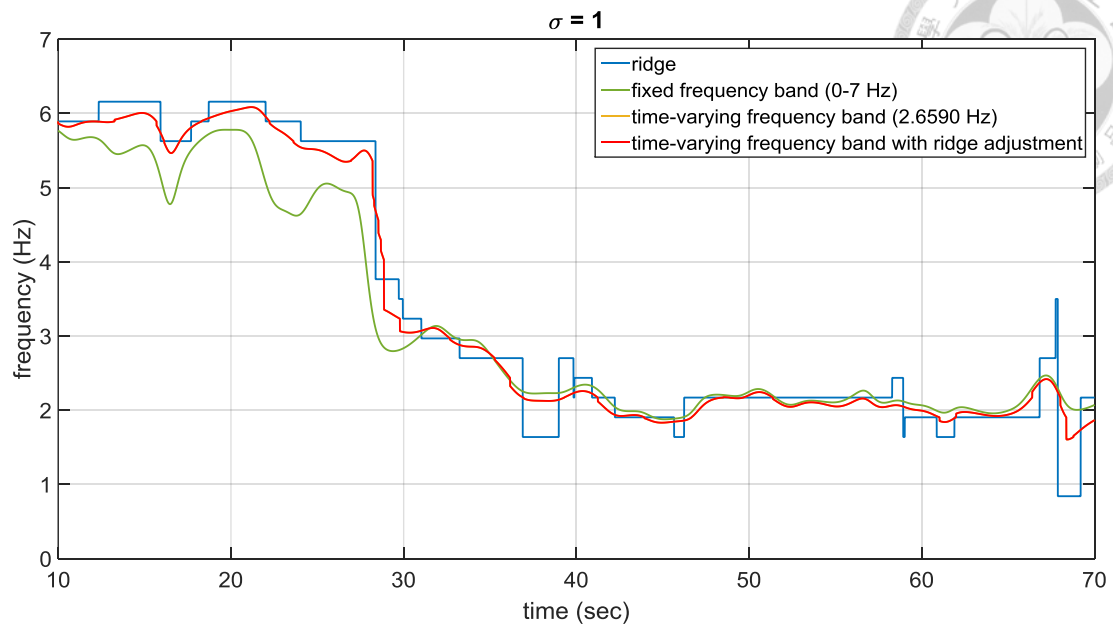
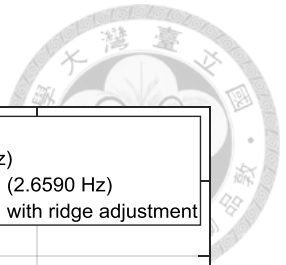


Figure 4-3 The pseudo-IF using different extraction methods

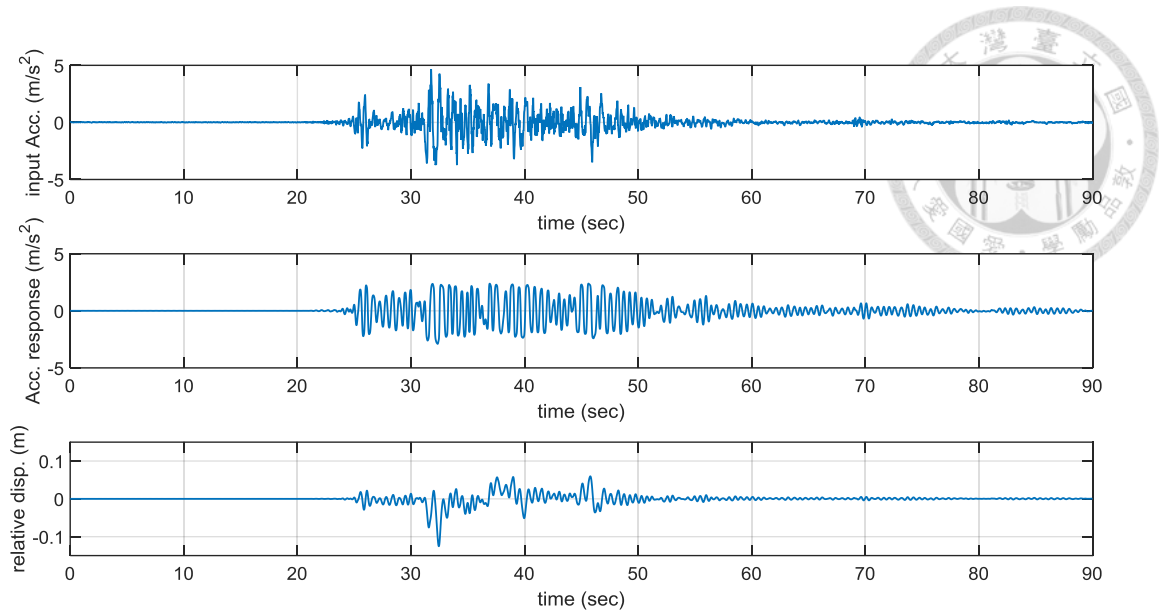


Figure 4-4 The time history of the simulated nonlinear SDOF system

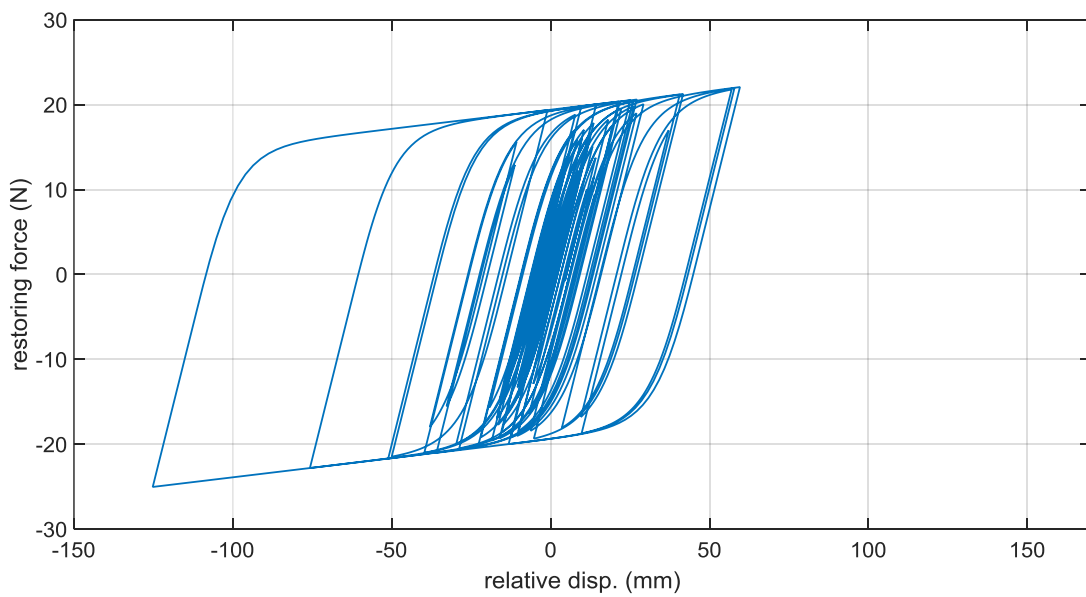


Figure 4-5 The hysteresis loop of the simulated nonlinear SDOF system

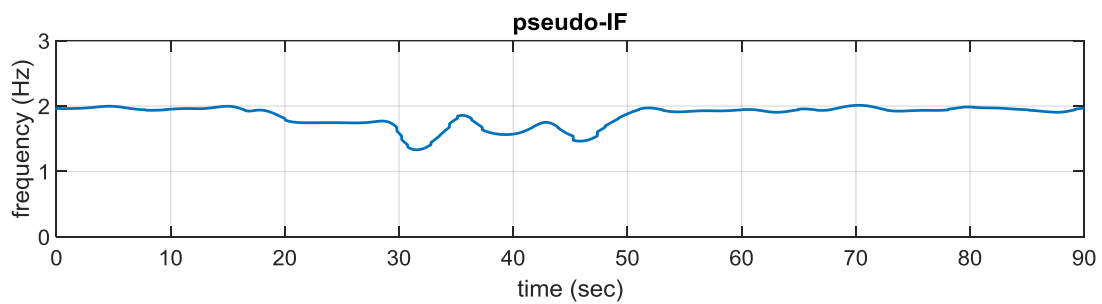


Figure 4-6 The pseudo-IF of the simulated nonlinear SDOF system

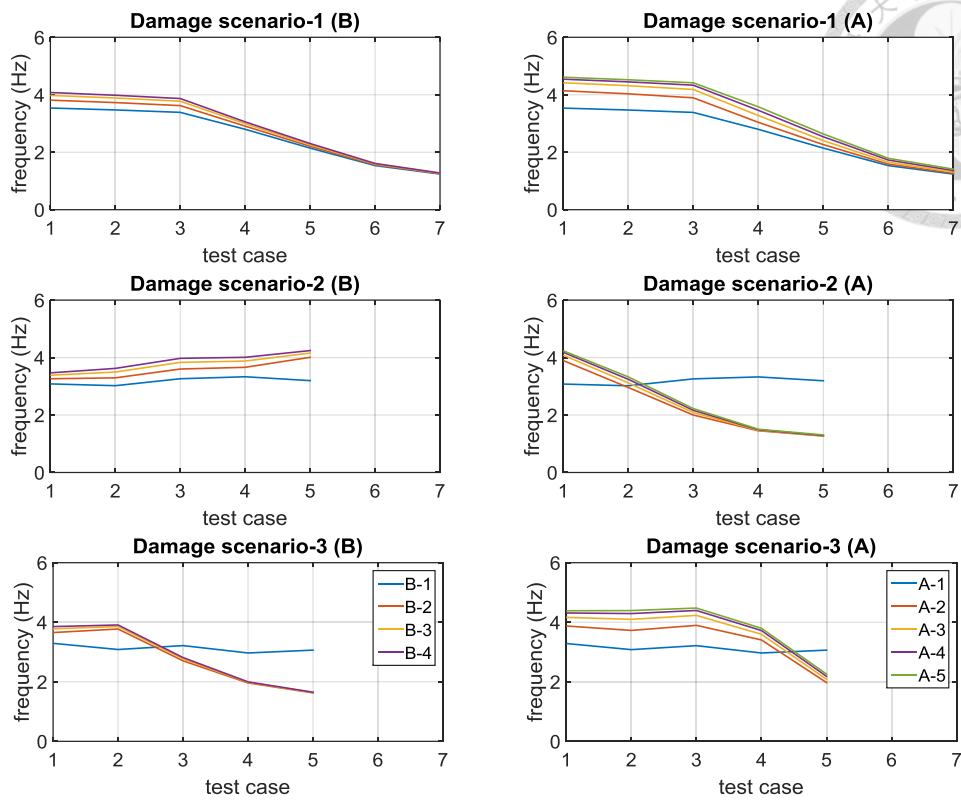


Figure 4-7 The central frequencies for twin-tower steel structure (w.r.t. frequency band: 0~6 Hz)

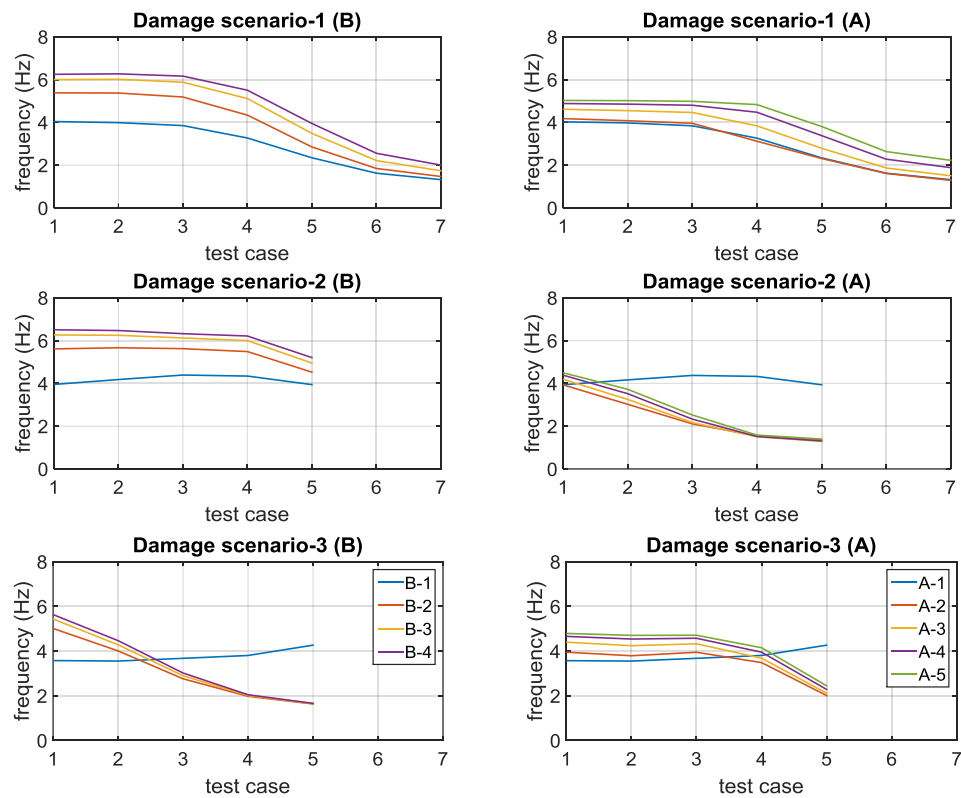


Figure 4-8 The central frequencies for twin-tower steel structure (w.r.t. frequency band: 0~10 Hz)

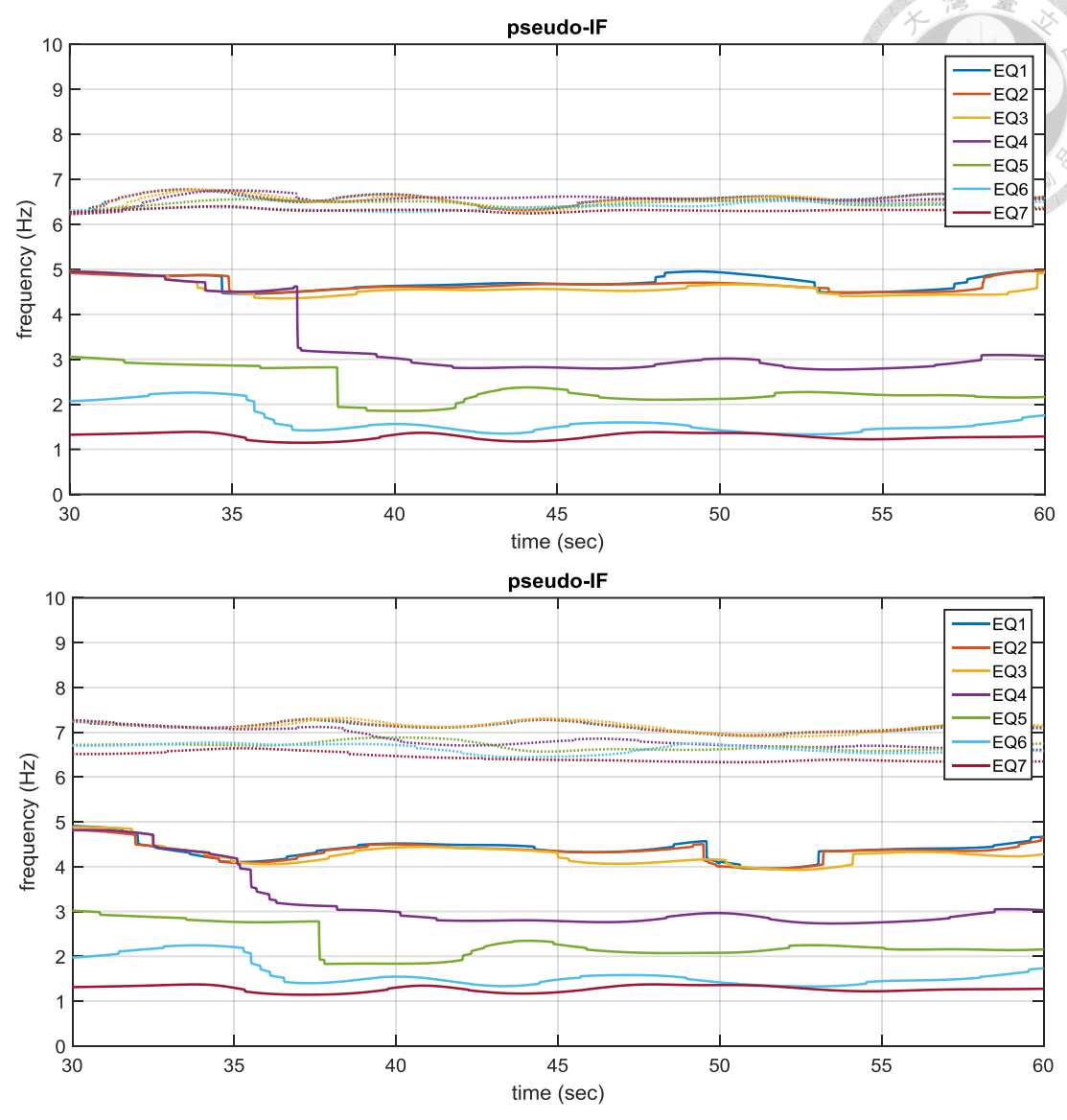
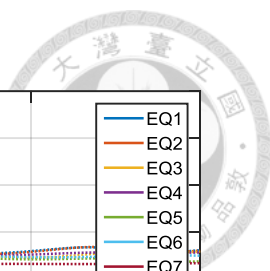


Figure 4-9 The pseudo-IF for damage scenario-1 with sensing node A-5 (top) and sensing node B-4 (bottom)

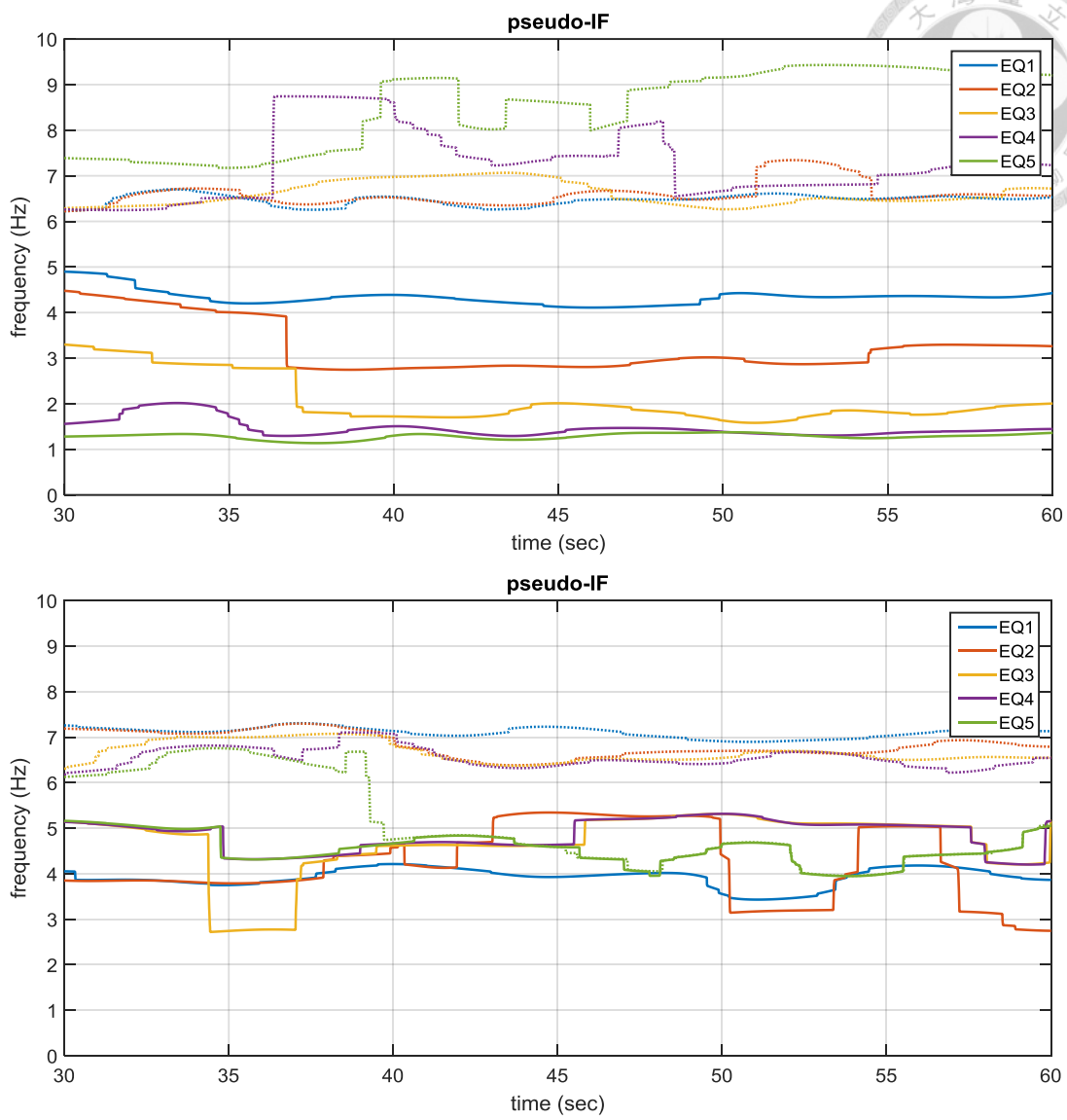
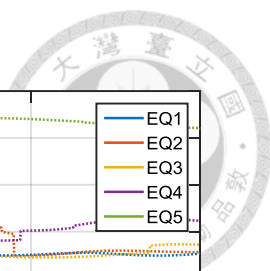


Figure 4-10 The pseudo-IF for damage scenario-2 with sensing node A-5 (top) and sensing node B-4 (bottom)

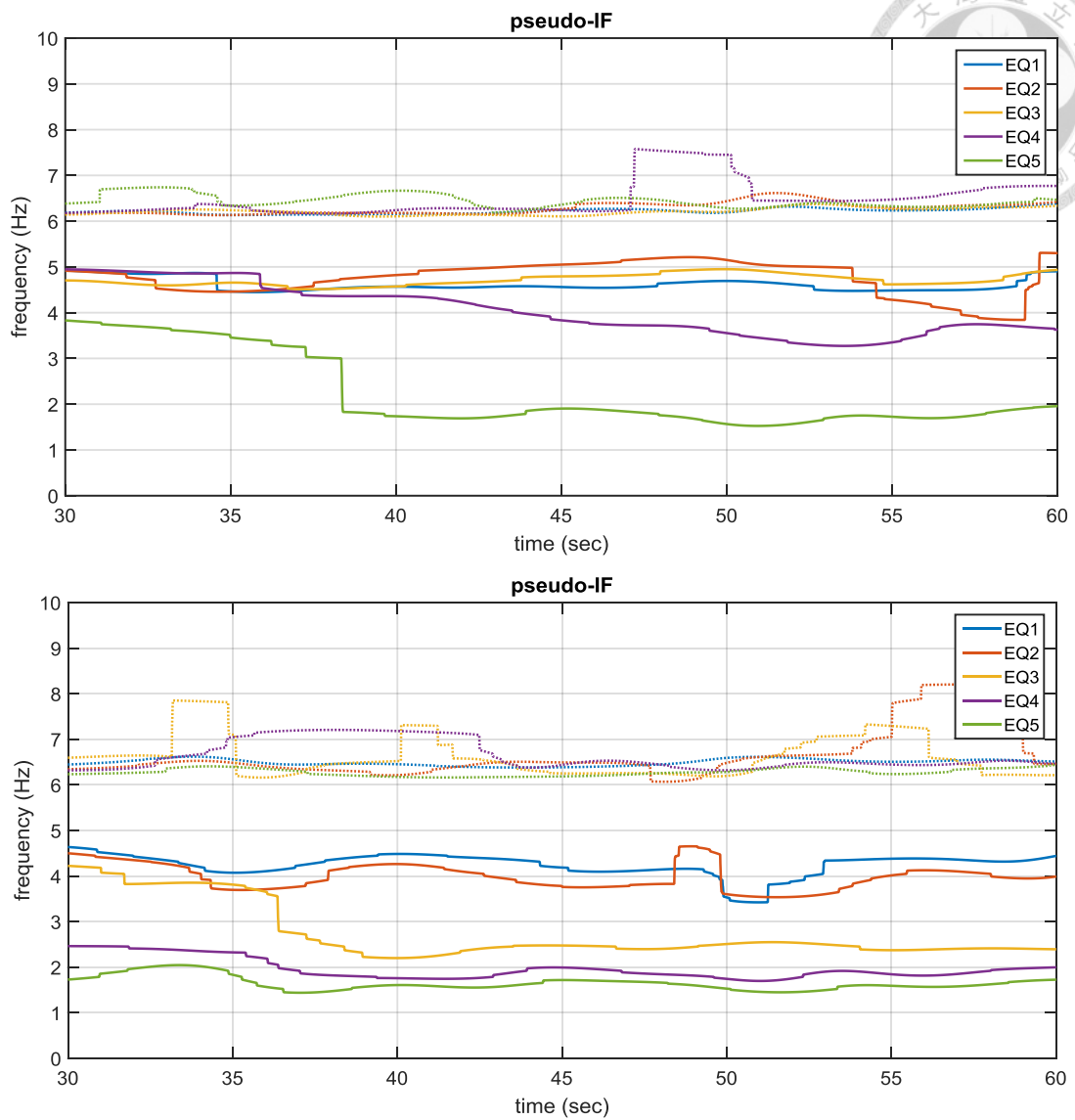


Figure 4-11 The pseudo-IF for damage scenario-3 with sensing node A-5 (top) and sensing node B-4 (bottom)

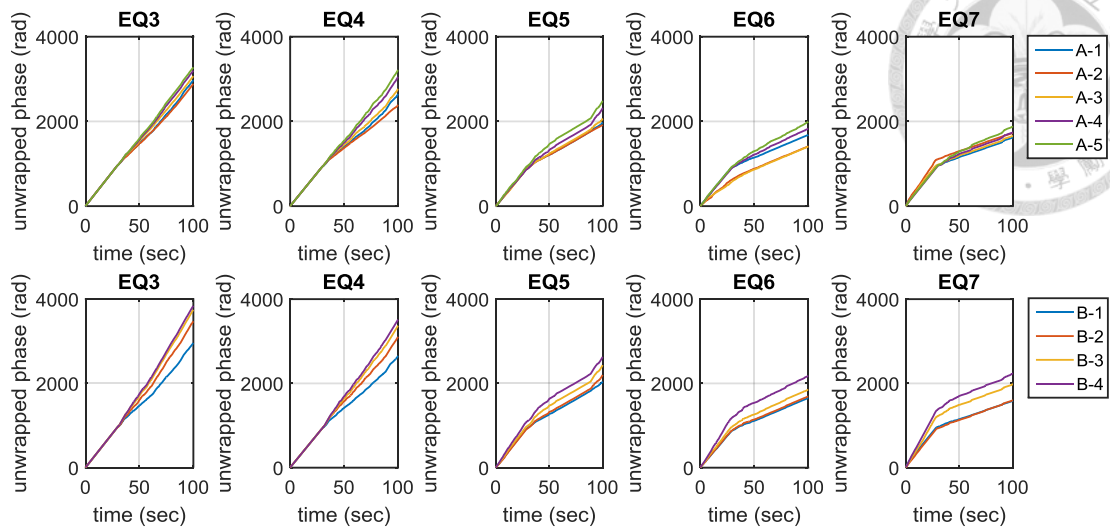


Figure 4-12 The unwrapped phase for damage scenario-1
(w.r.t. frequency band: 0~10 Hz)

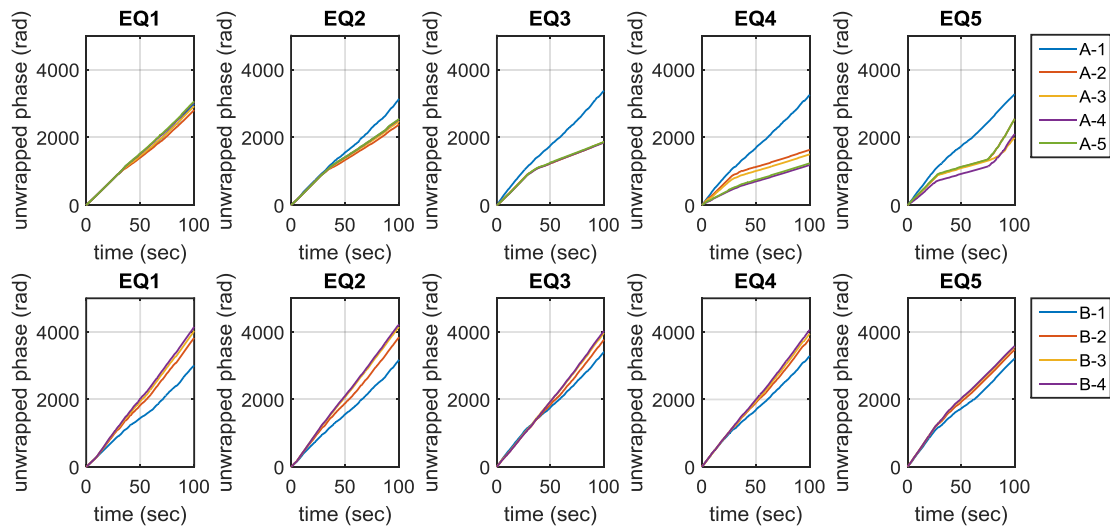


Figure 4-13 The unwrapped phase for damage scenario-2
(w.r.t. frequency band: 0~10 Hz)

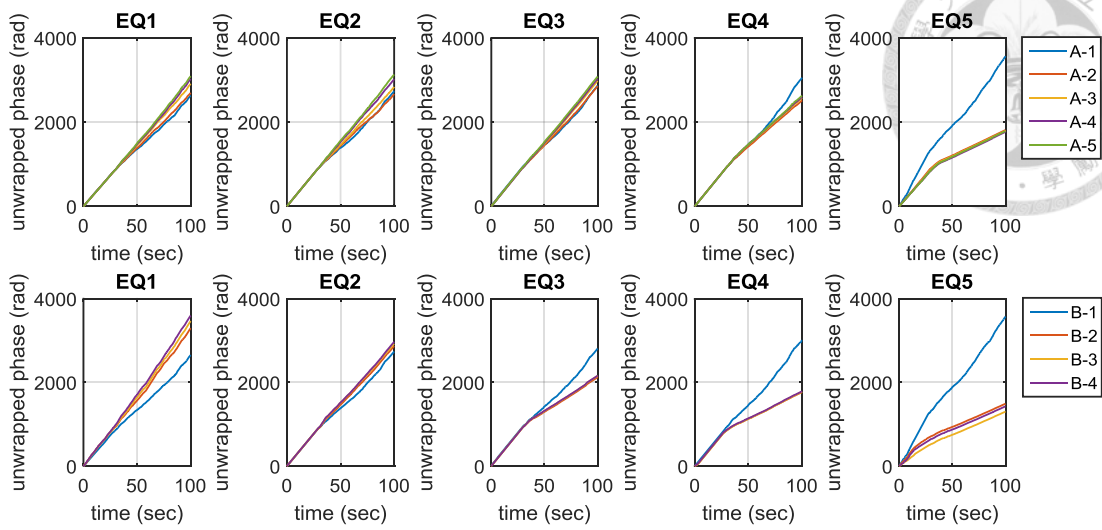


Figure 4-14 The unwrapped phase for damage scenario-3 (w.r.t. frequency band: 0~10 Hz)

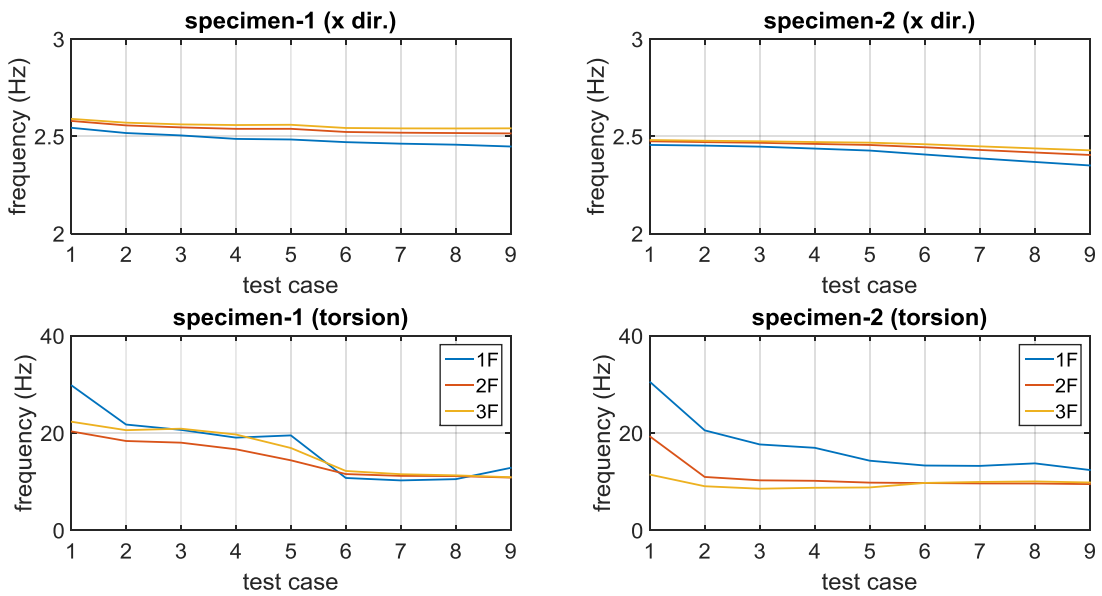


Figure 4-15 The central frequency for two three-story steel frames (w.r.t. x-dir. frequency band: 0~5 Hz, torsional dir. frequency band 0~50 Hz)

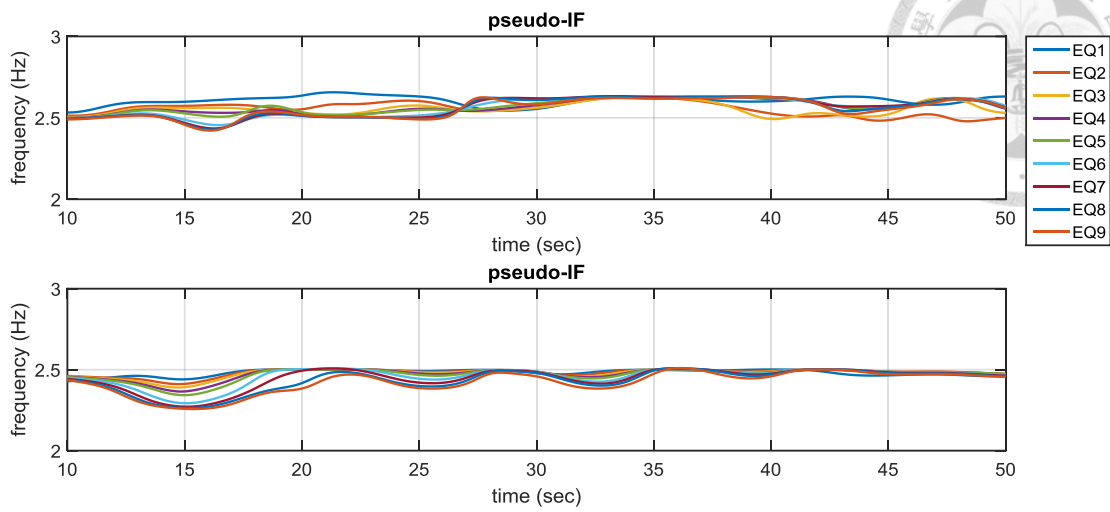


Figure 4-16 The pseudo-IF for two three-story steel frames in x-dir. with specimen-1 (top) and specimen-2 (bottom) (w.r.t. x-dir. frequency band: 0~5 Hz)

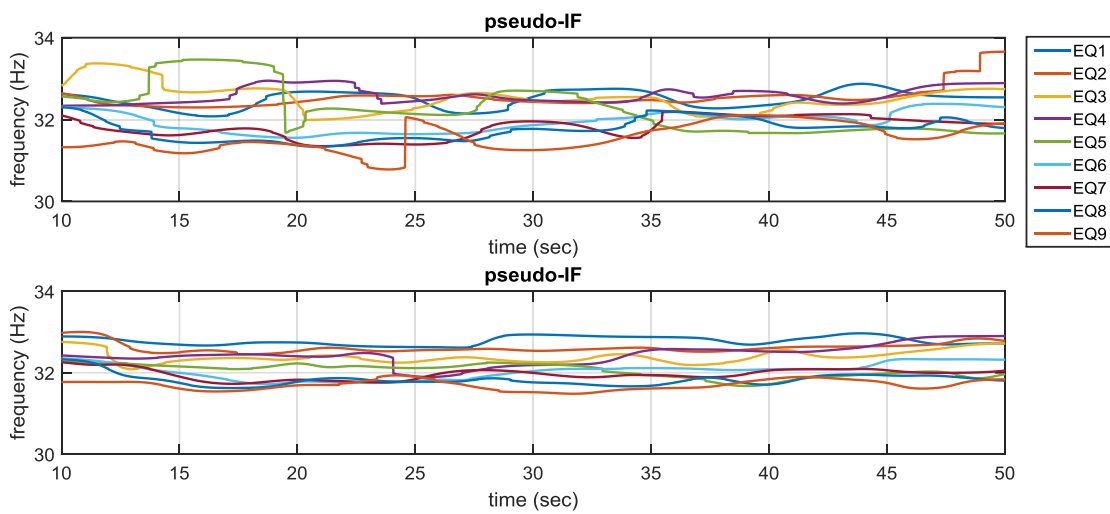


Figure 4-17 The pseudo-IF for two three-story steel frames in torsion direction with specimen-1 (top) and specimen-2 (bottom) (w.r.t. torsional dir. frequency band: 25~40 Hz)

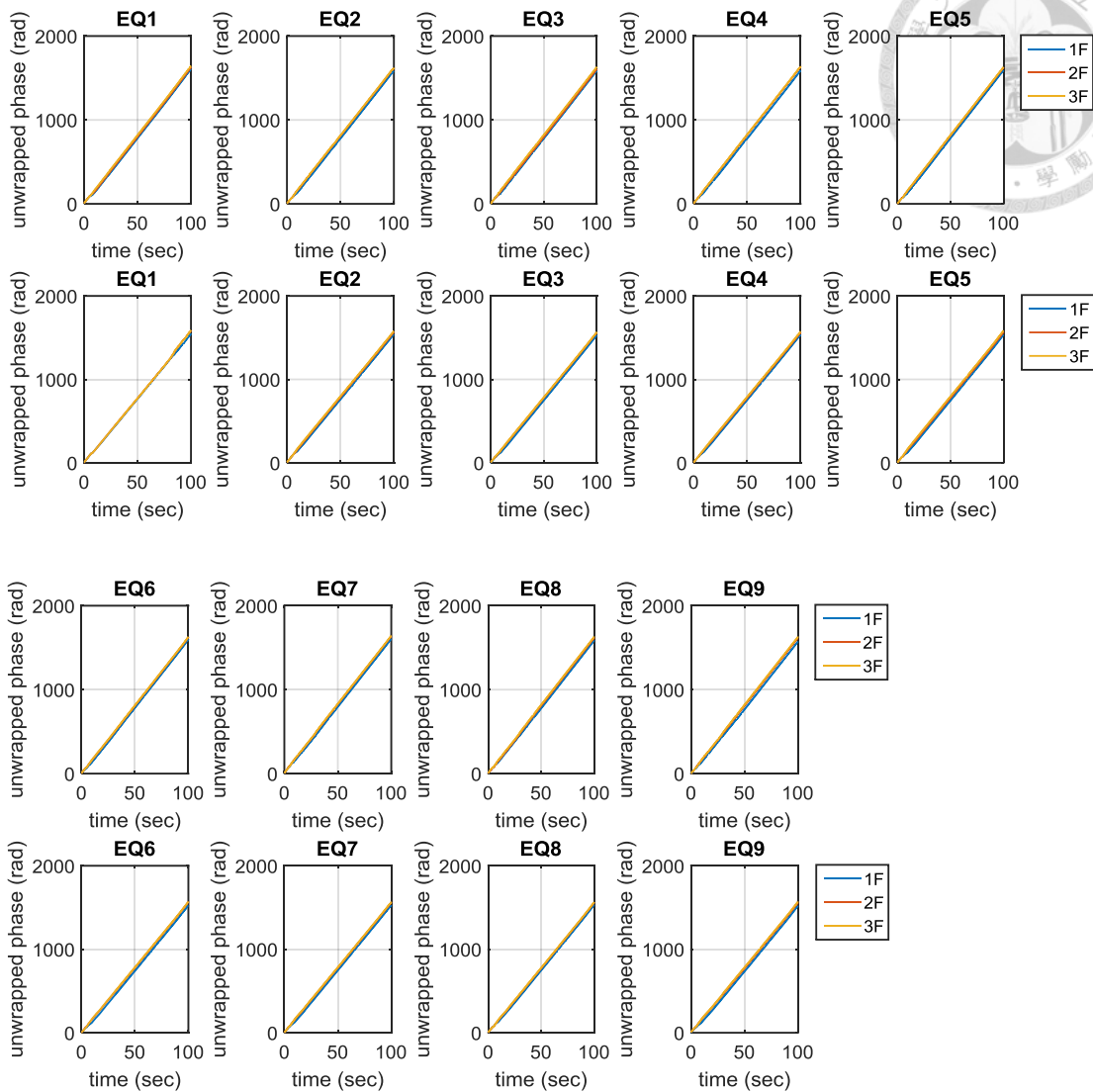


Figure 4-18 The unwrapped phase for two three-story steel frames in x-dir. with specimen-1 (1st and 3rd row) and specimen-2 (2nd and 4th row) (w.r.t. x-dir. frequency band: 0~5 Hz)

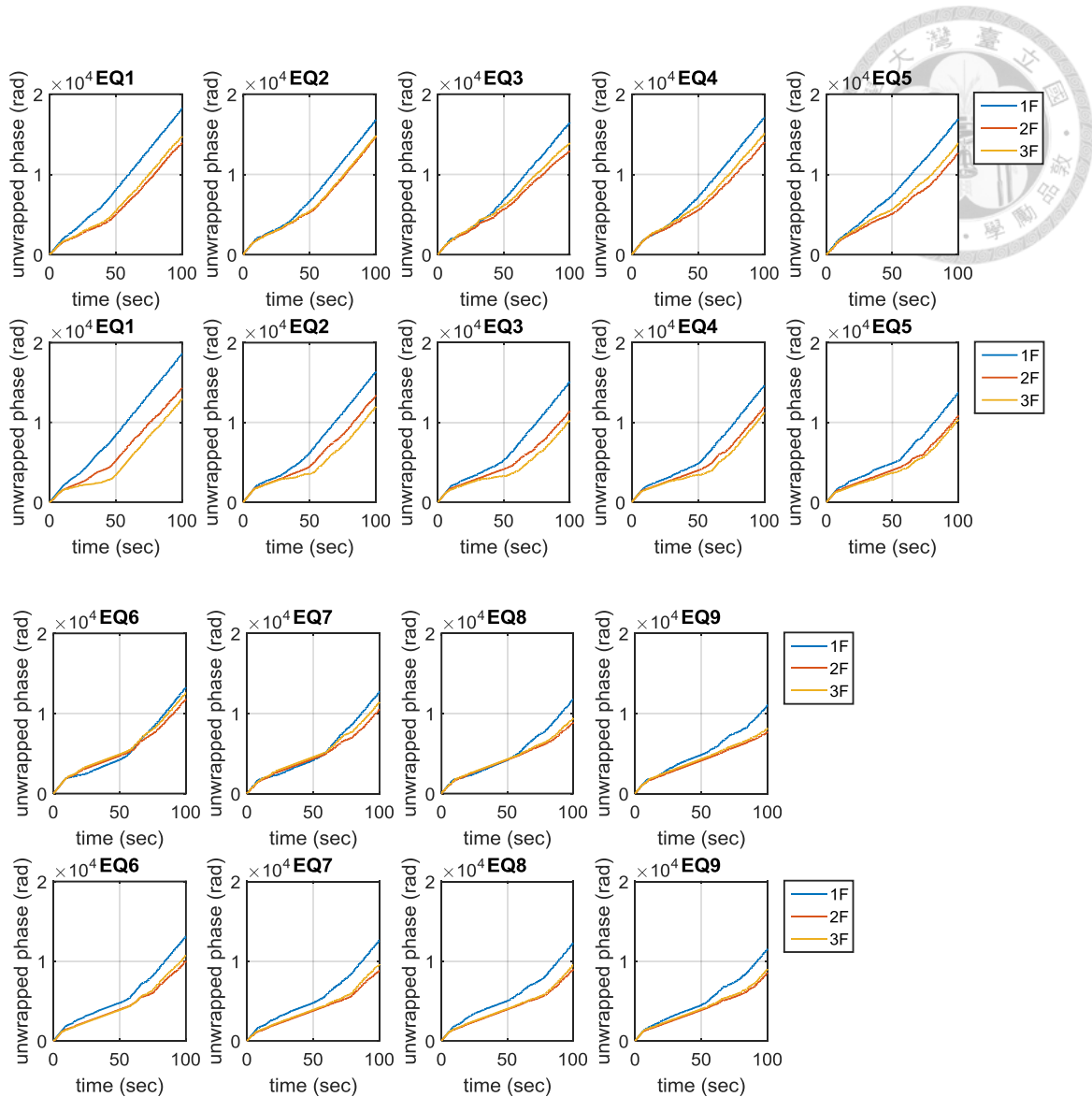


Figure 4-19 The unwrapped phase for two three-story steel frames in torsional dir. with specimen-1 (1st and 3rd row) and specimen-2 (2nd and 4th row) (w.r.t. torsional dir. frequency band: 0~50 Hz)

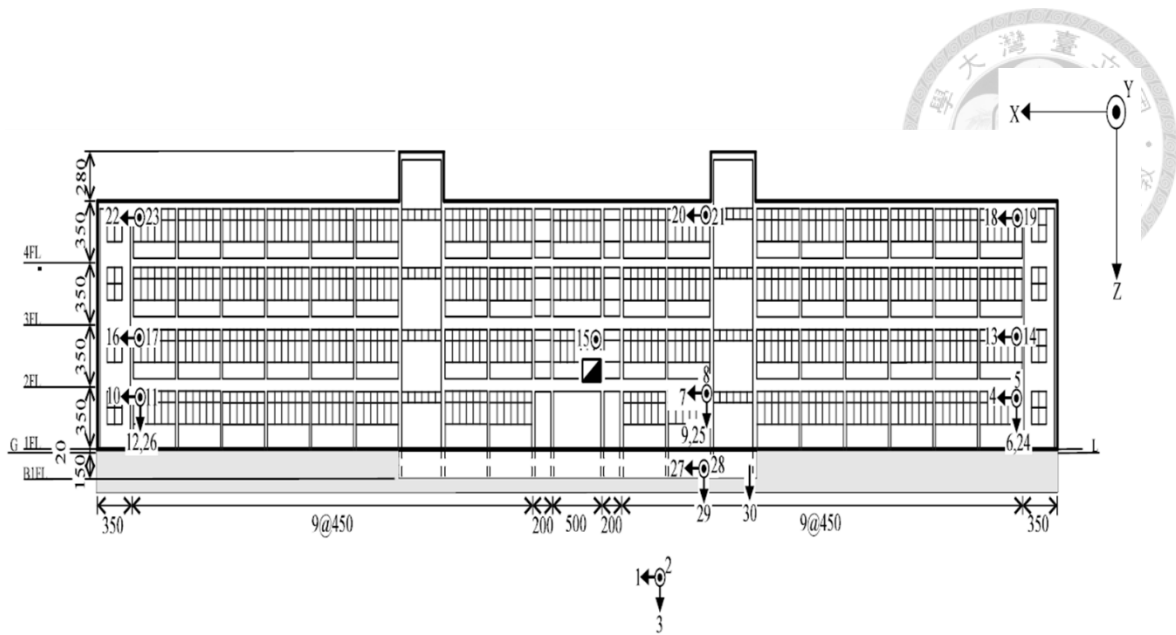


Figure 5-1 Sensor instrumentations for the Mingli Elementary School

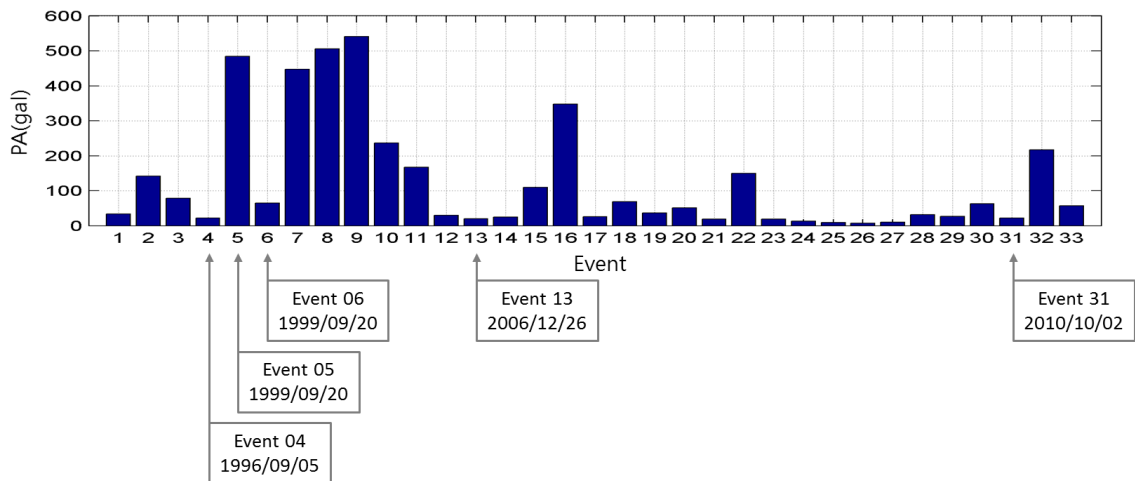


Figure 5-2 The peak acceleration (PA) of every recorded earthquake event

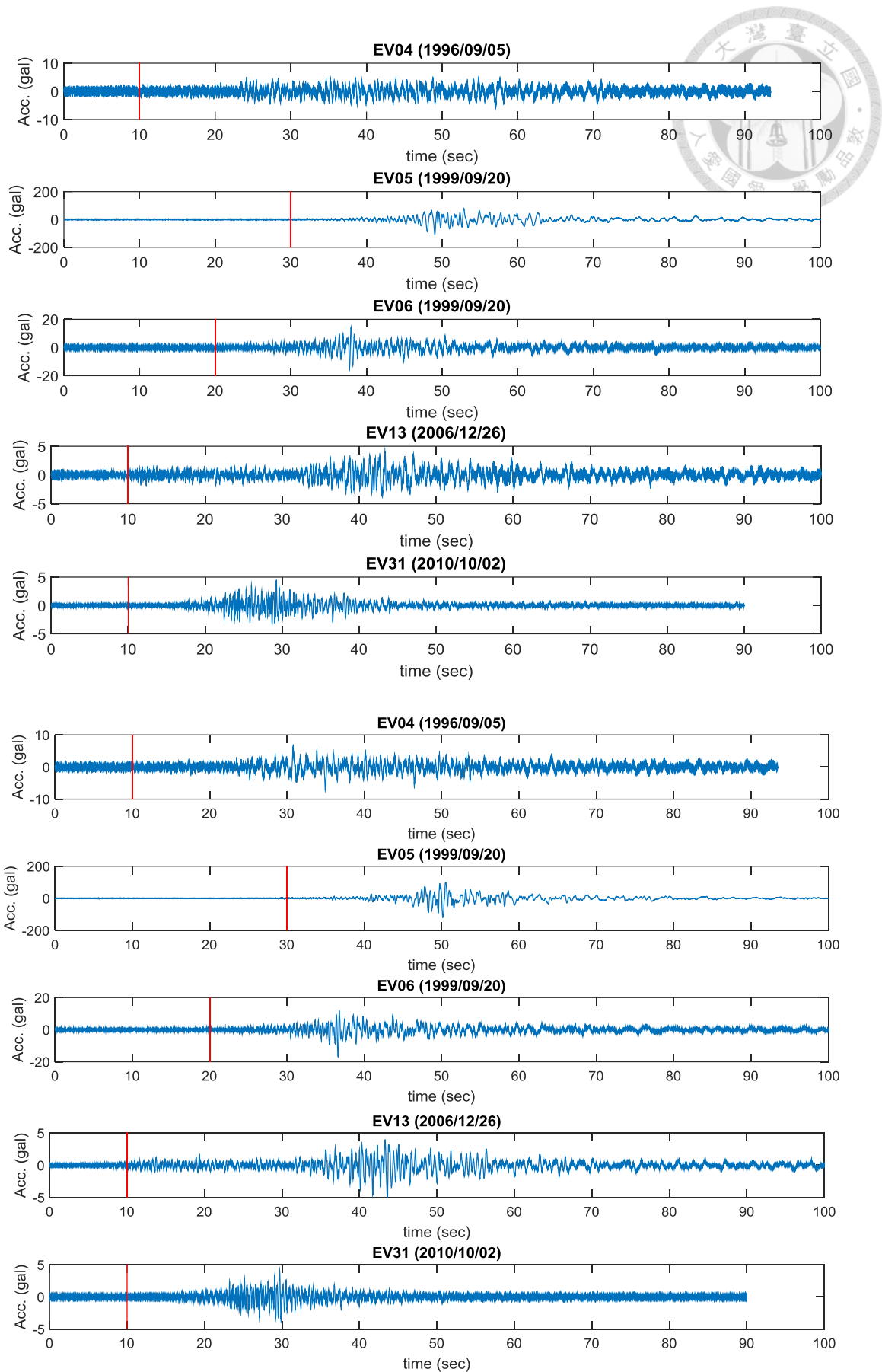


Figure 5-3 The recorded accelerations of basement in y-dir. (top) and x-dir. (bottom)

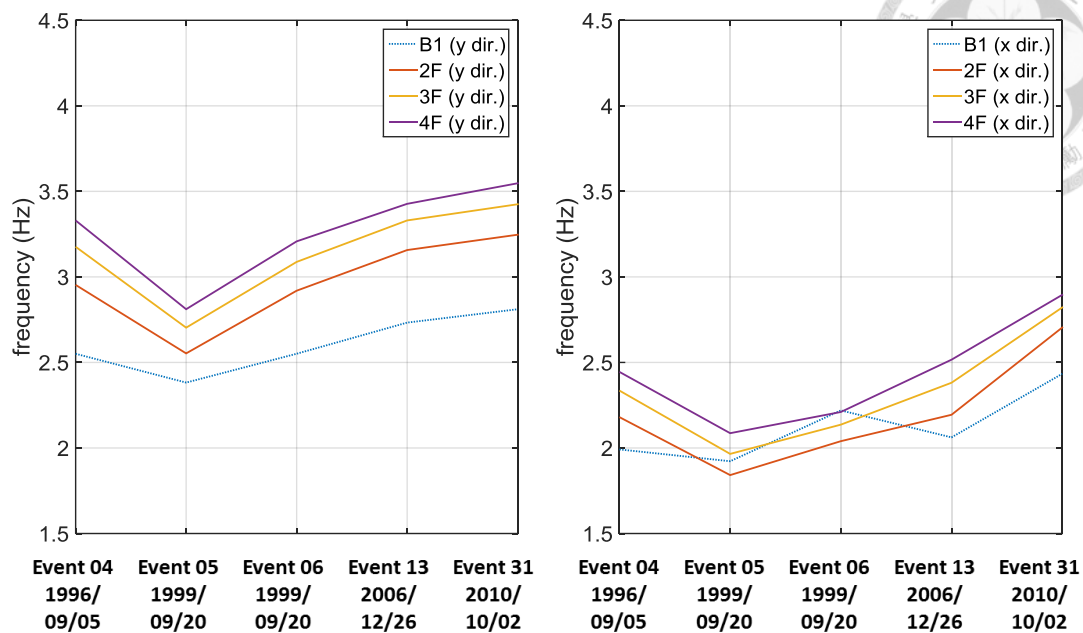


Figure 5-4 The central frequency for the Mingli Elementary School (w.r.t. y-dir. frequency band: 1.5~5 Hz, x-dir. frequency band 1~4 Hz)

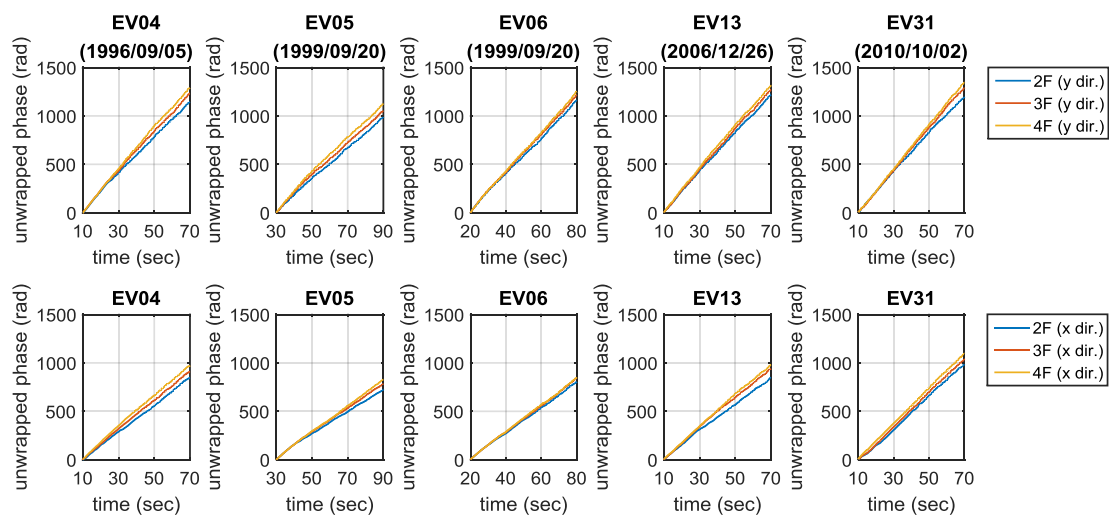


Figure 5-5 The unwrapped phase for the Mingli Elementary School (w.r.t. y-dir. frequency band: 1.5~5 Hz, x-dir. frequency band 1~4 Hz)

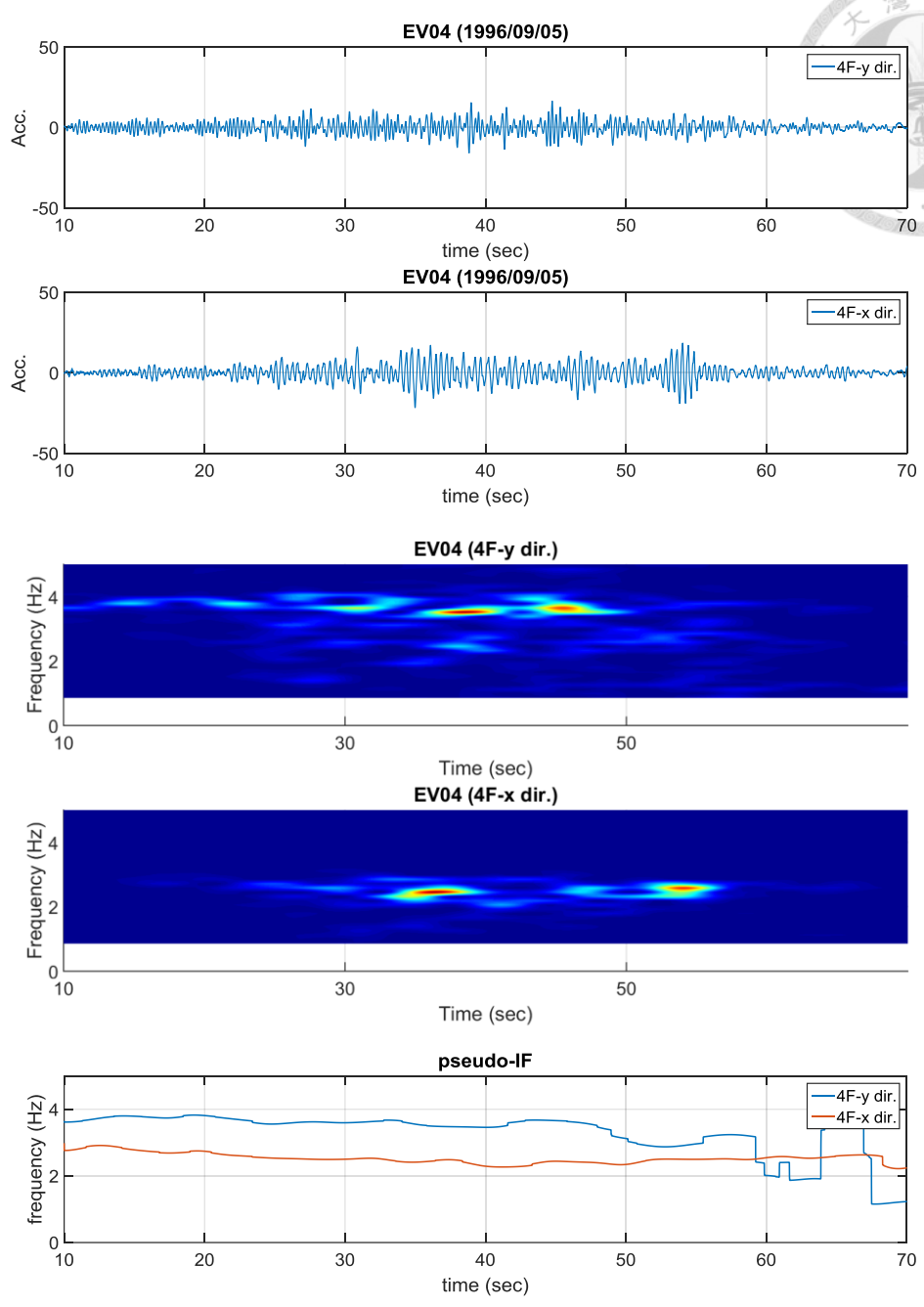
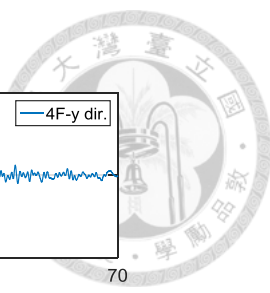


Figure 5-6 The pseudo-IF for EV04 (1996/09/05)
(w.r.t. frequency band: 0.5~6 Hz for both directions)

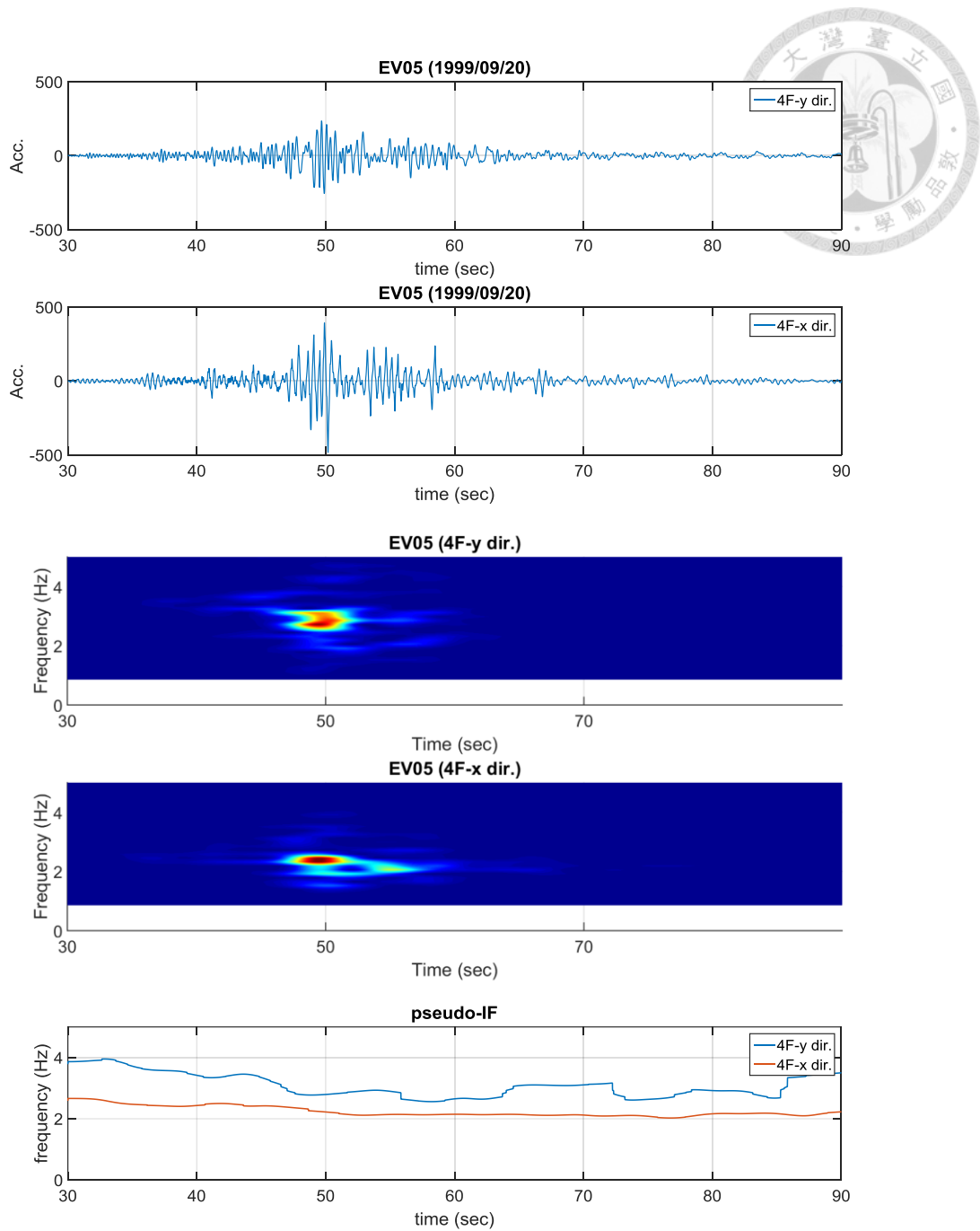


Figure 5-7 The pseudo-IF for EV05 (1999/09/20) using relative acceleration (w.r.t. frequency band: 0.5~6 Hz for both directions)

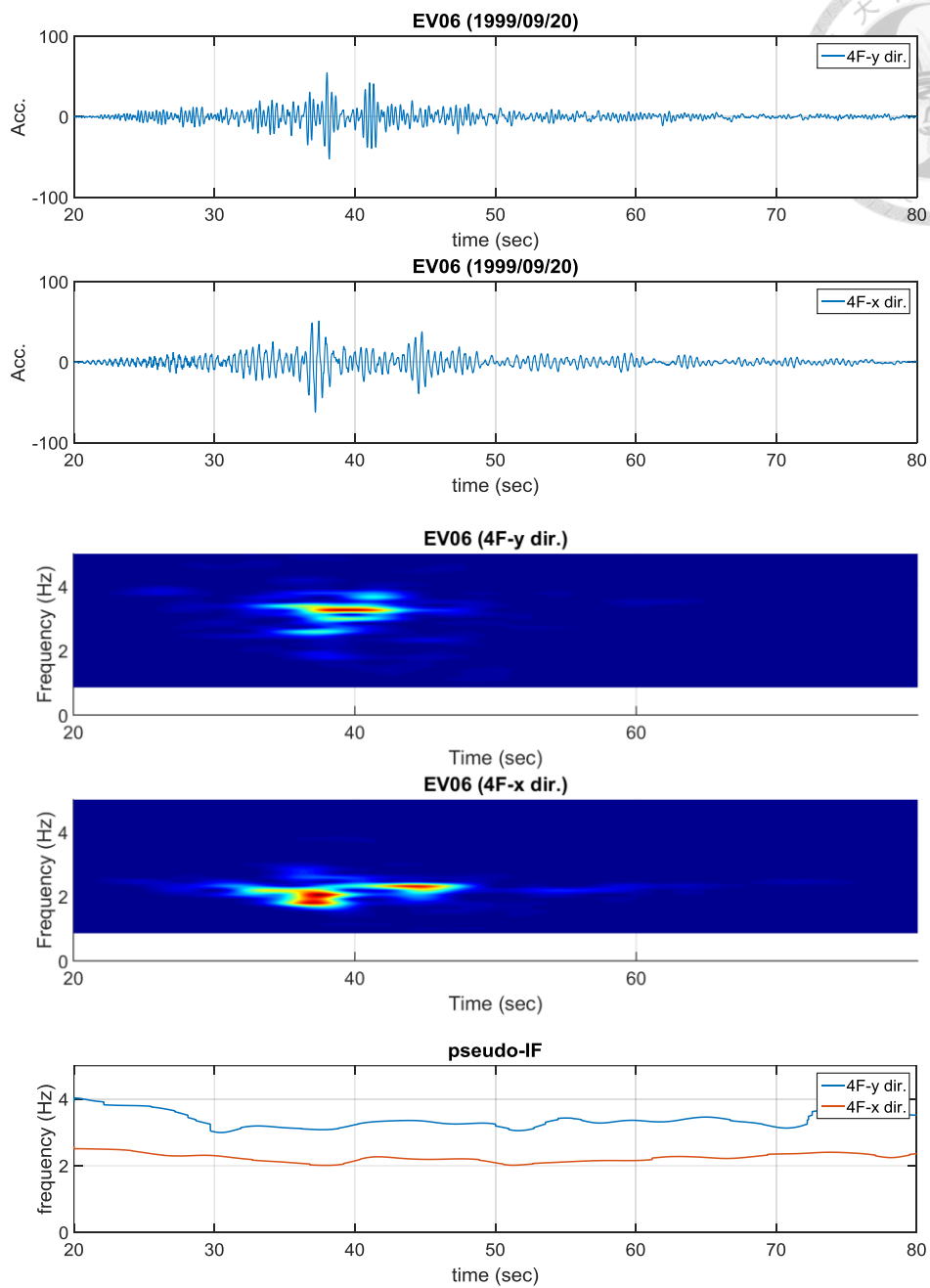


Figure 5-8 The pseudo-IF for EV06 (1999/09/20)
(w.r.t. frequency band: 0.5~6 Hz for both directions)

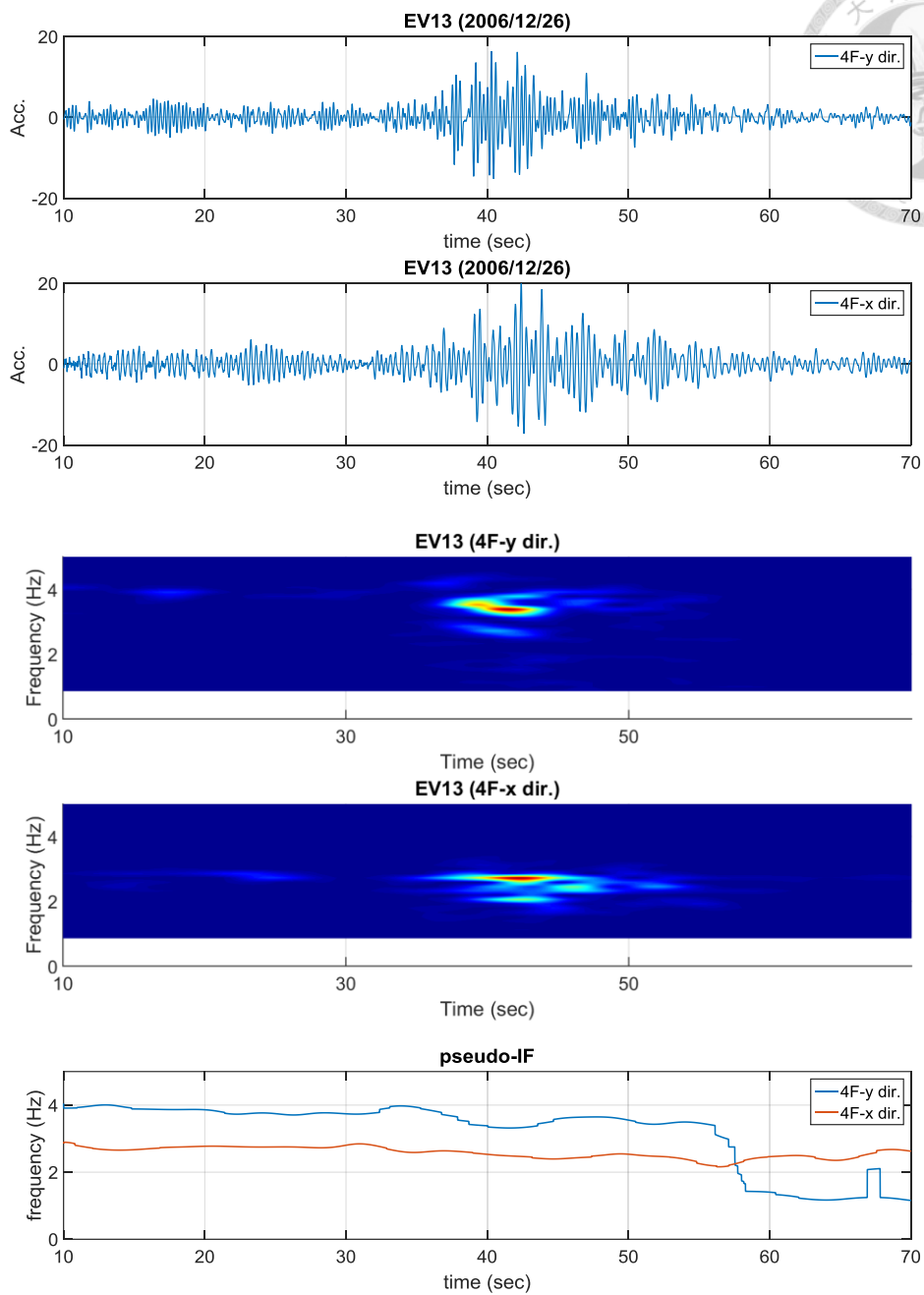


Figure 5-9 The pseudo-IF for EV05 (2006/12/26)
(w.r.t. frequency band: 0.5~6 Hz for both directions)

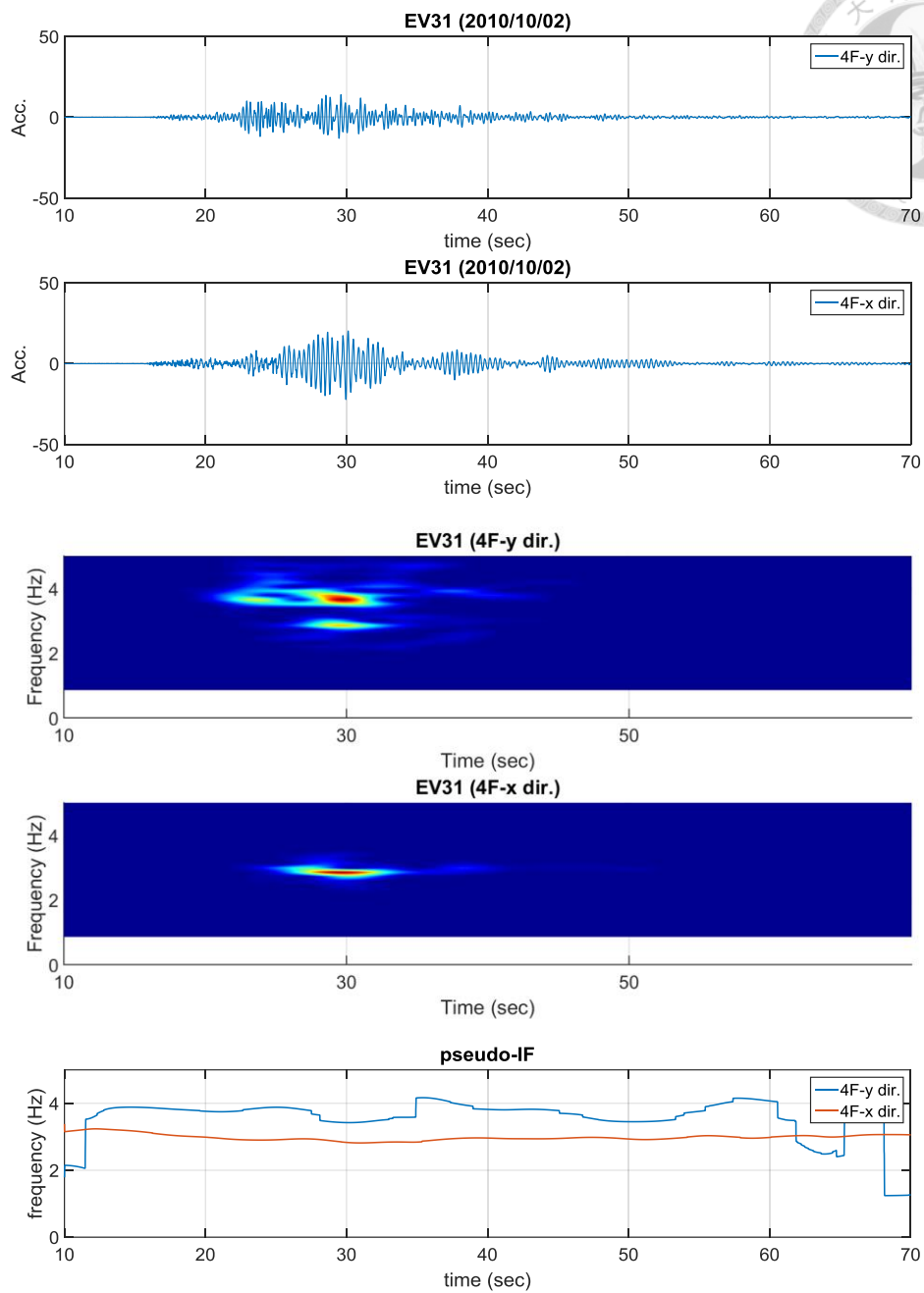


Figure 5-10 The pseudo-IF for EV05 (2010/10/02)
(w.r.t. frequency band: 0.5~6 Hz for both directions)

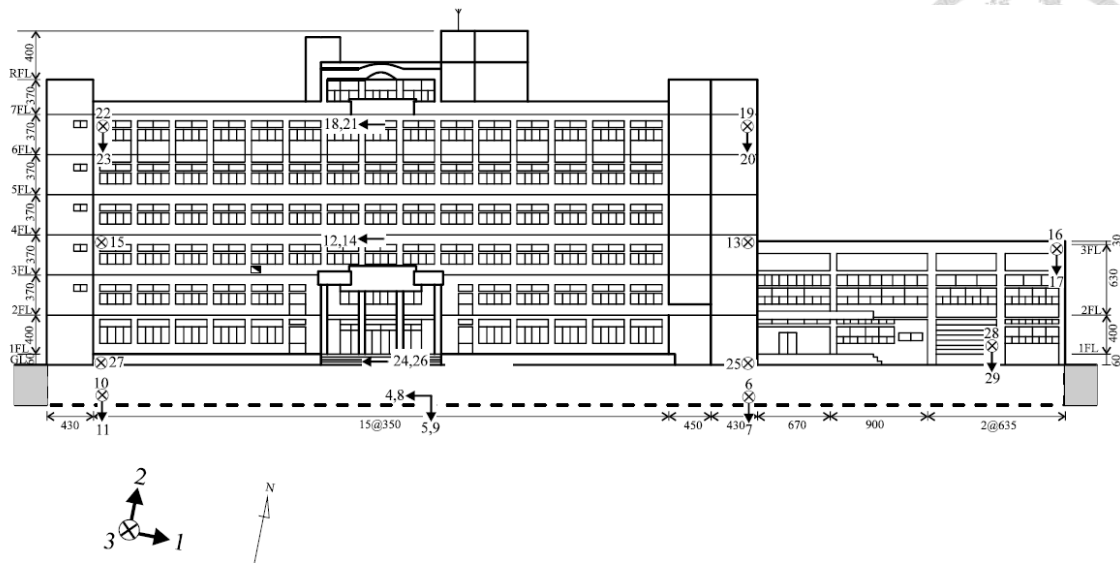


Figure 5-11 Sensor instrumentations for the NCHU Civil & Environmental Engineering Building

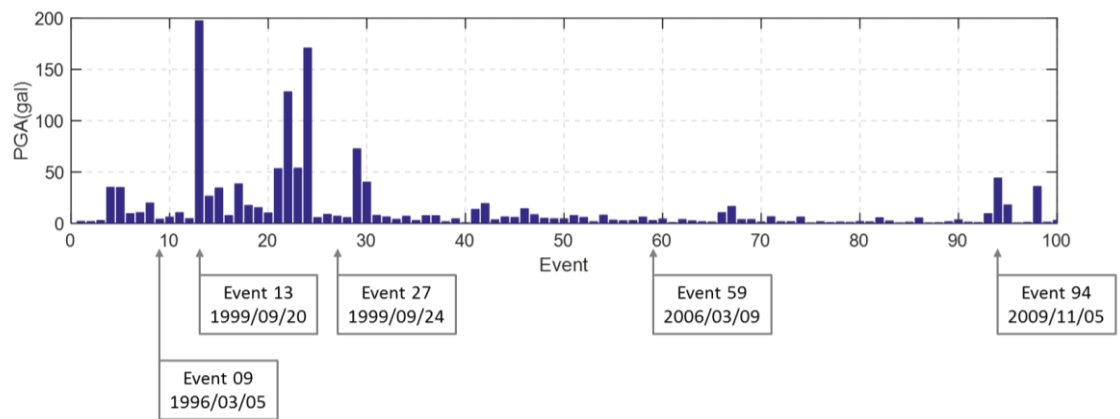


Figure 5-12 The peak ground acceleration (PGA) of every recorded earthquake event

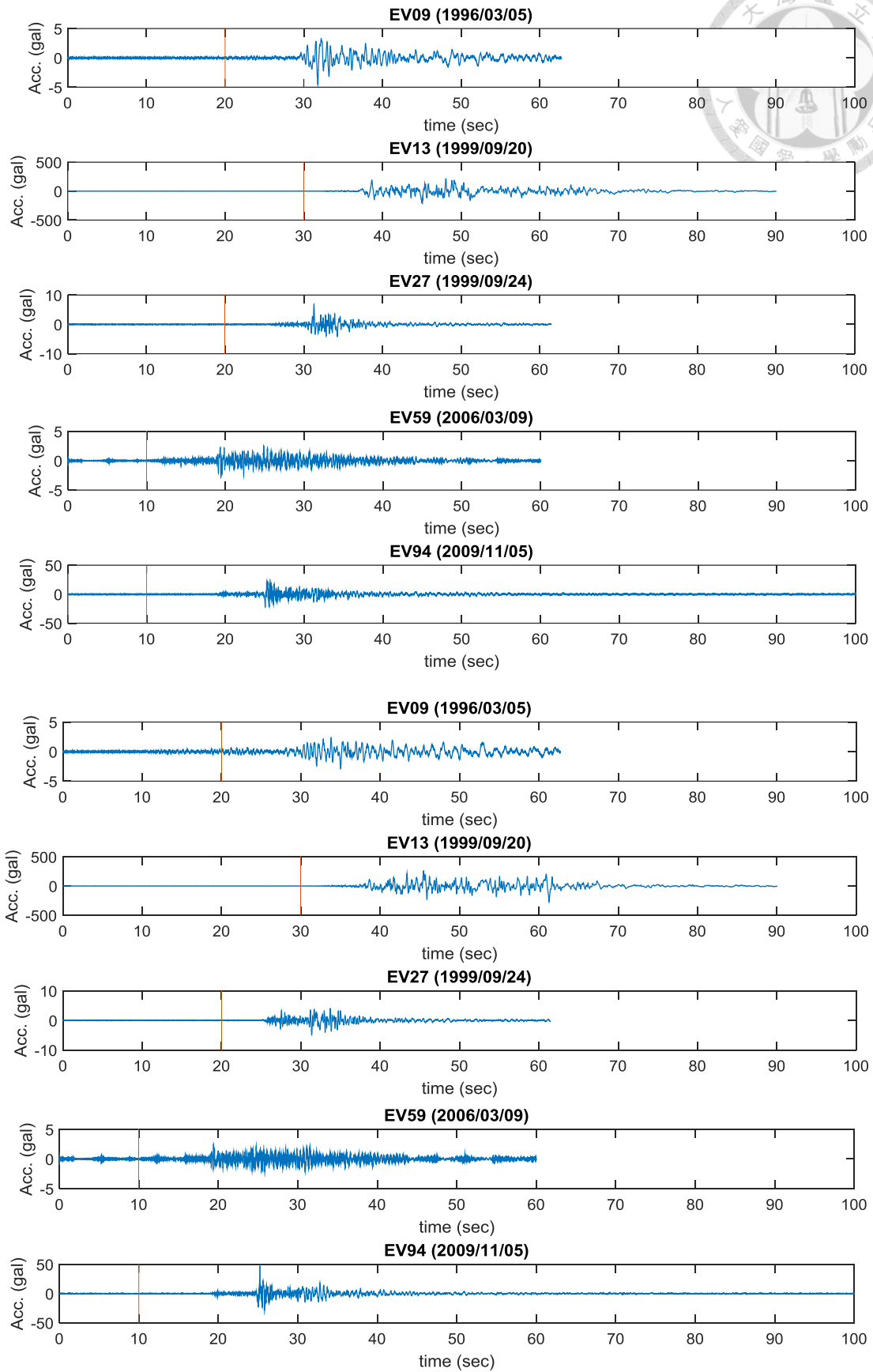
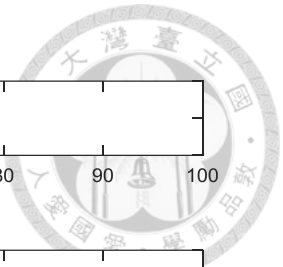


Figure 5-13 The recorded accelerations of 1F in x-dir. (top) and y-dir. (bottom)

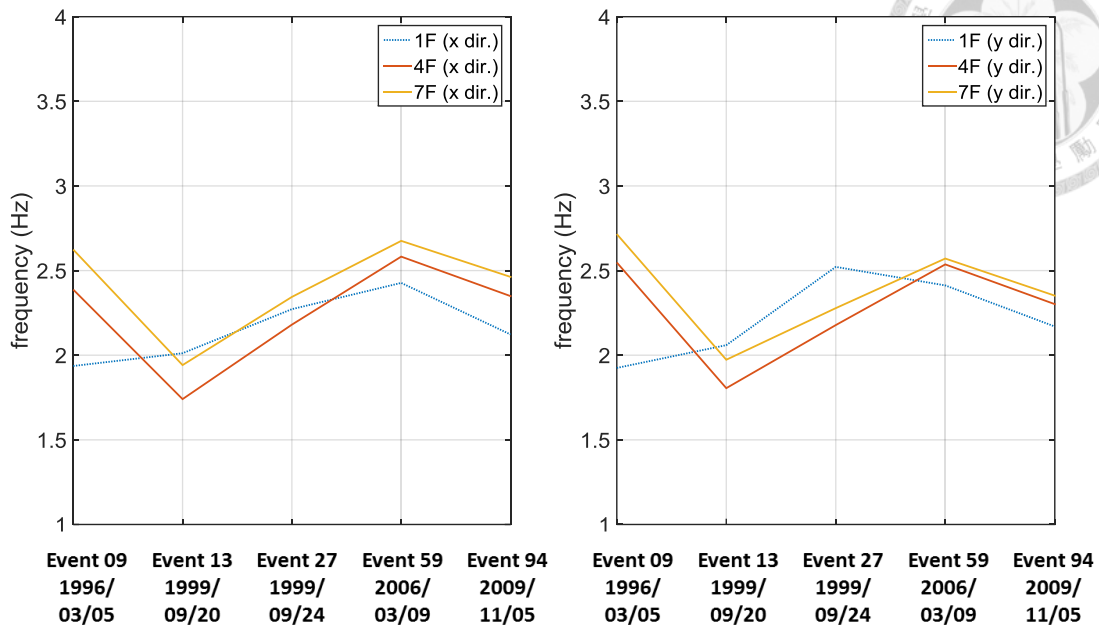
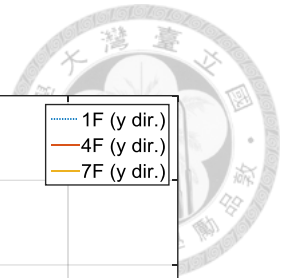


Figure 5-14 The central frequency for the NCHU Civil & Environmental Engineering Building (w.r.t. frequency band: 1~4 Hz for both direction)

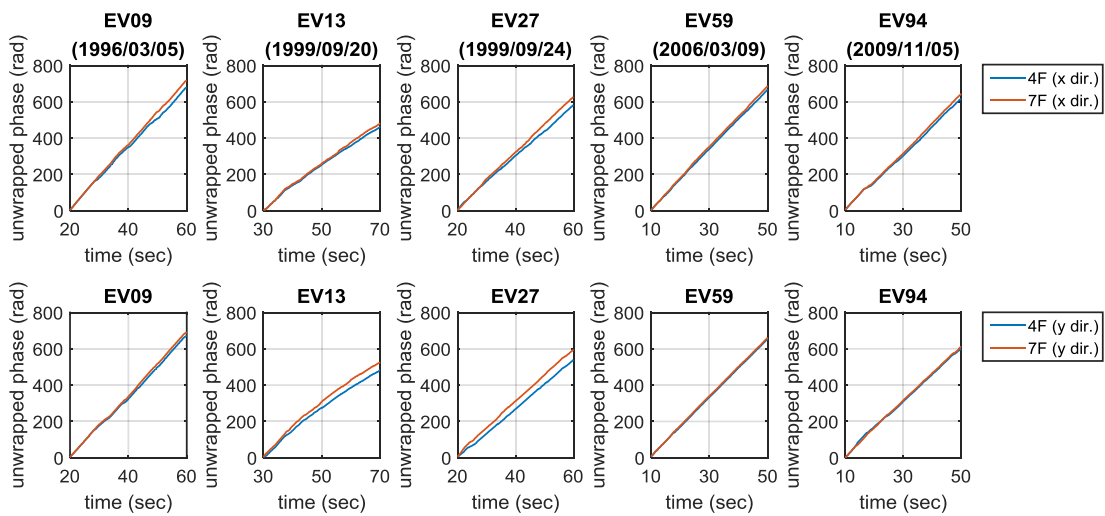


Figure 5-15 The unwrapped phase for the NCHU Civil & Environmental Engineering Building (w.r.t. frequency band: 1~4 Hz for both direction)

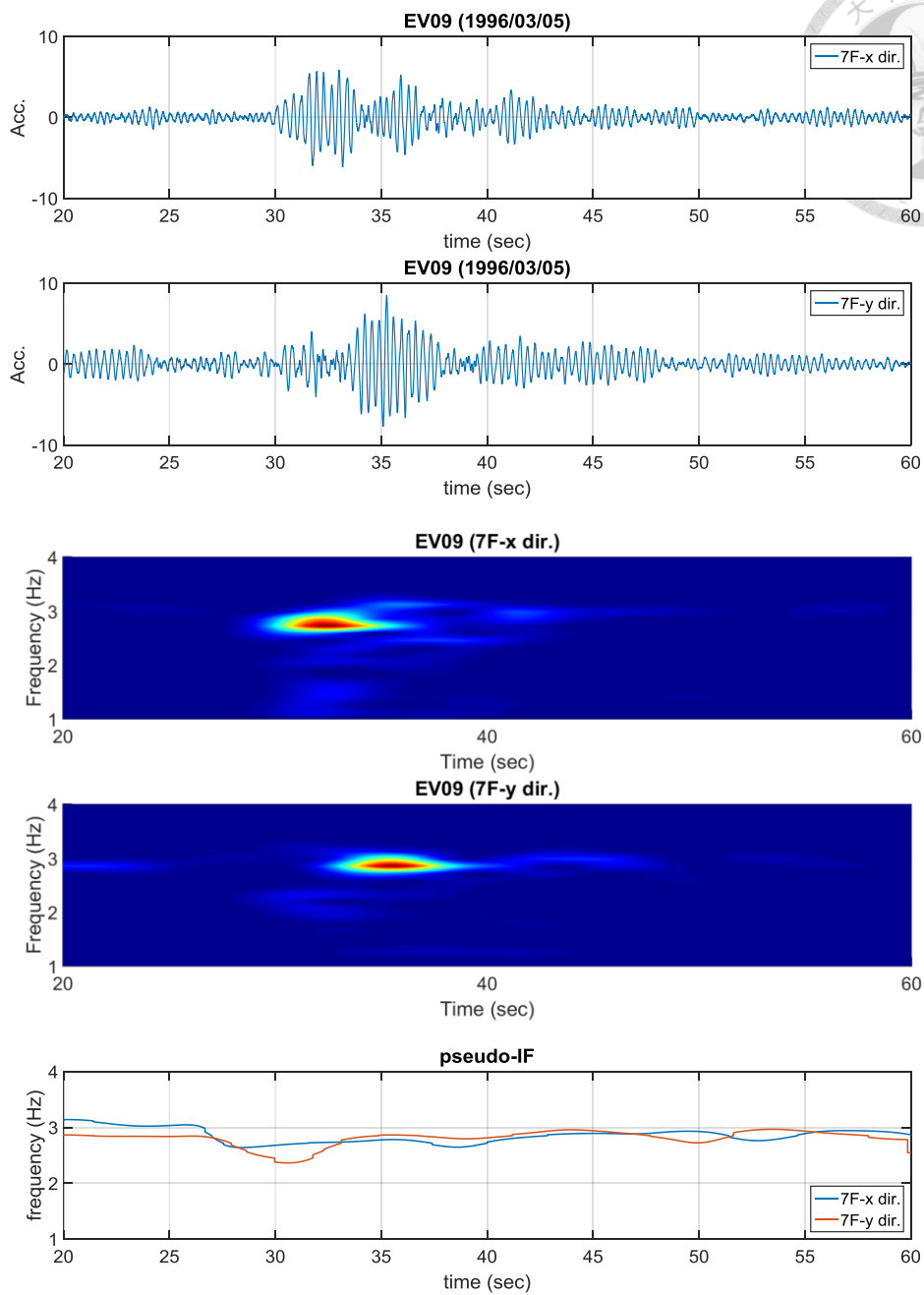


Figure 5-16 The pseudo-IF for EV09 (1996/03/05)
(w.r.t. frequency band: 0.5~6 Hz for both directions)

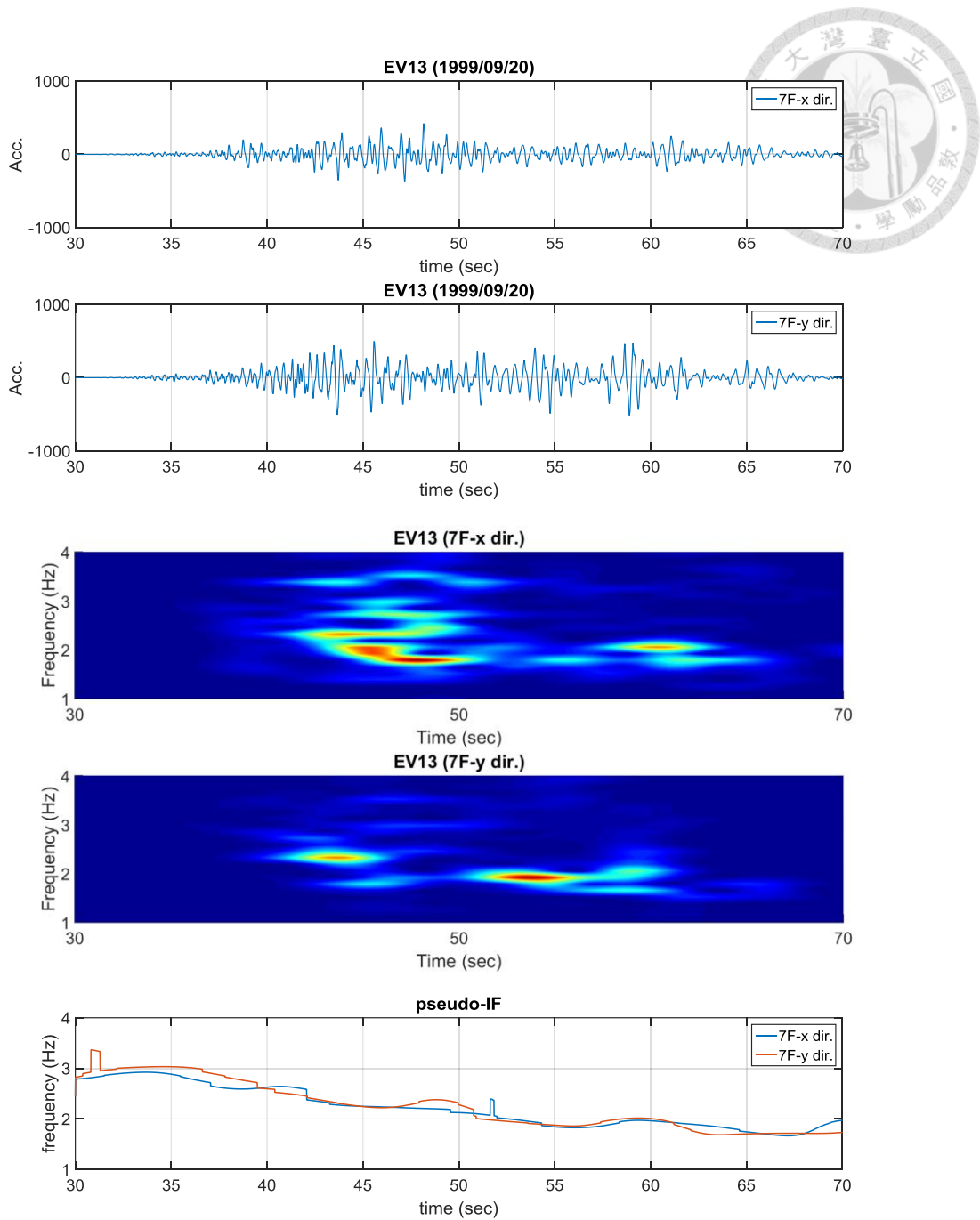


Figure 5-17 The pseudo-IF for EV13 (1999/09/20) using relative acceleration (w.r.t. frequency band: 0.5~6 Hz for both directions)

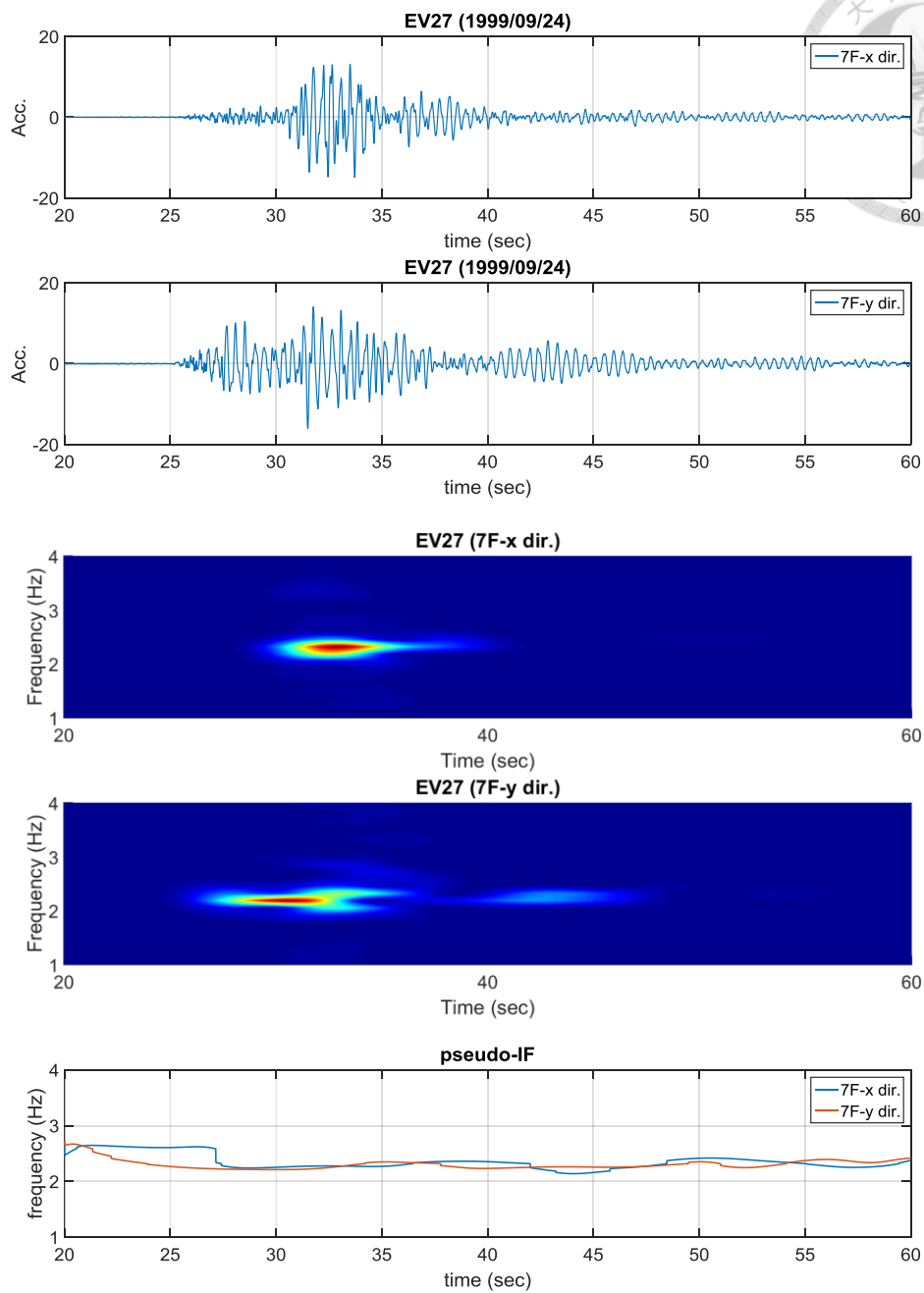


Figure 5-18 The pseudo-IF for EV27 (1999/09/24)
(w.r.t. frequency band: 0.5~6 Hz for both directions)

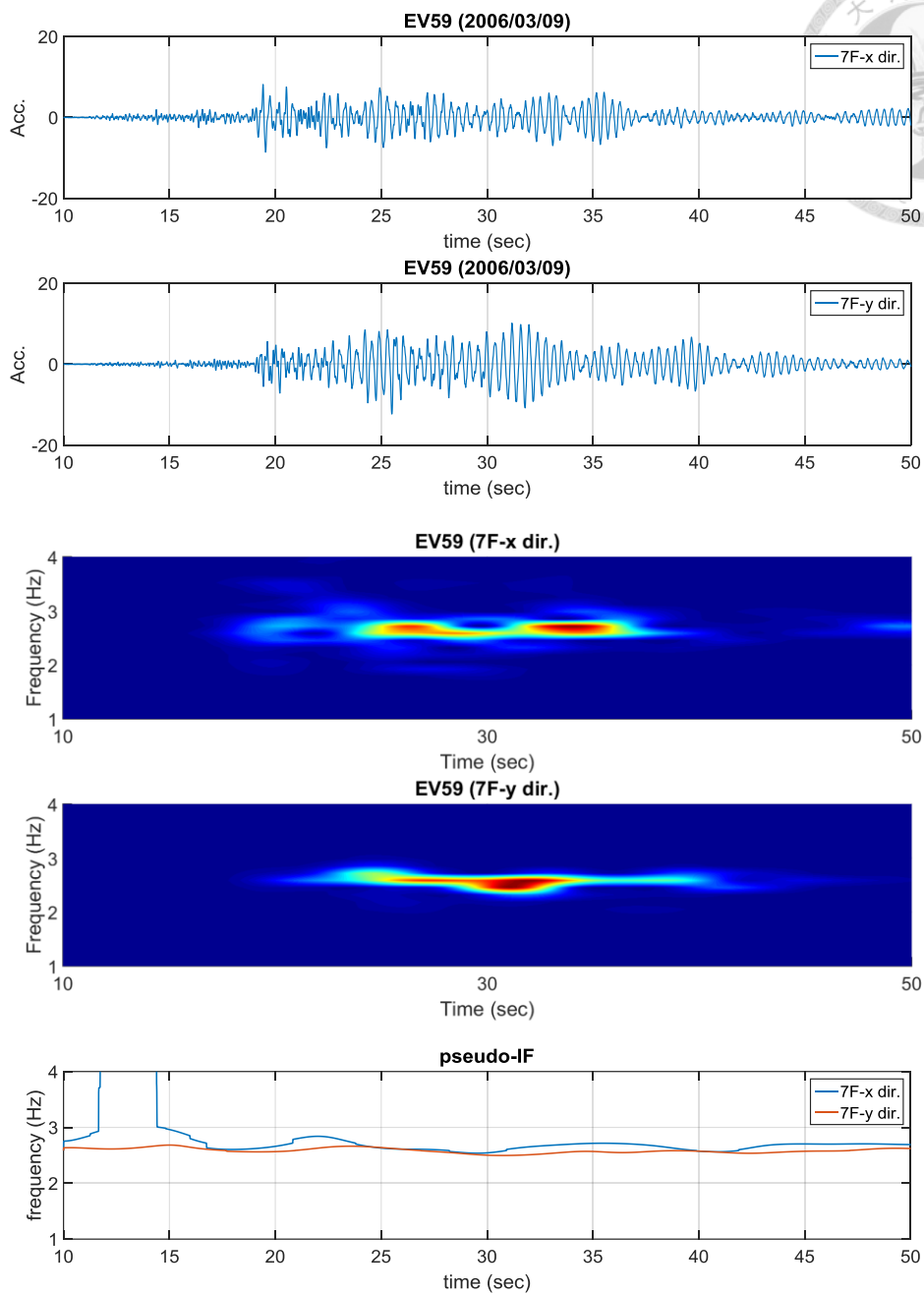


Figure 5-19 The pseudo-IF for EV59 (2006/03/09)
(w.r.t. frequency band: 0.5~6 Hz for both directions)

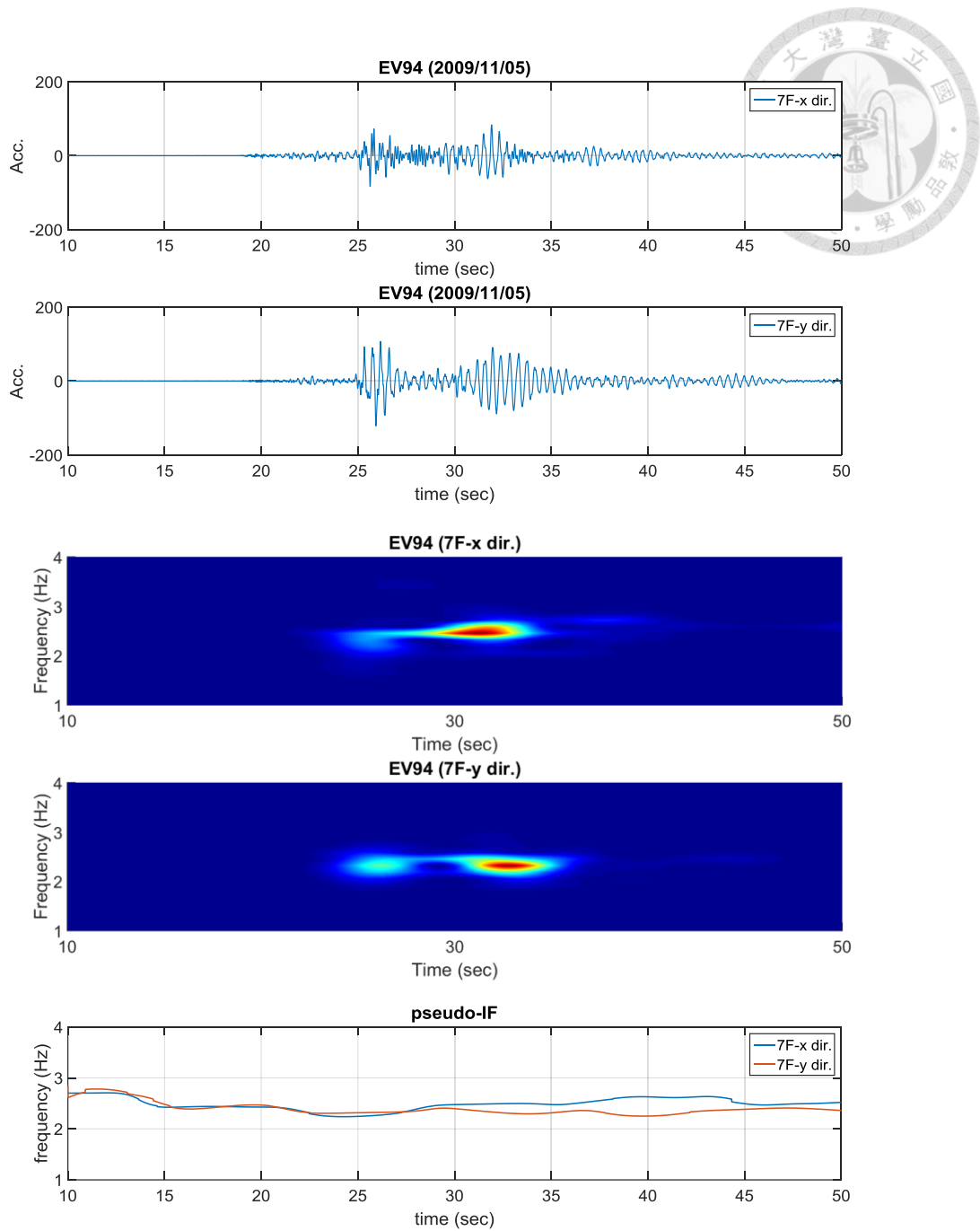


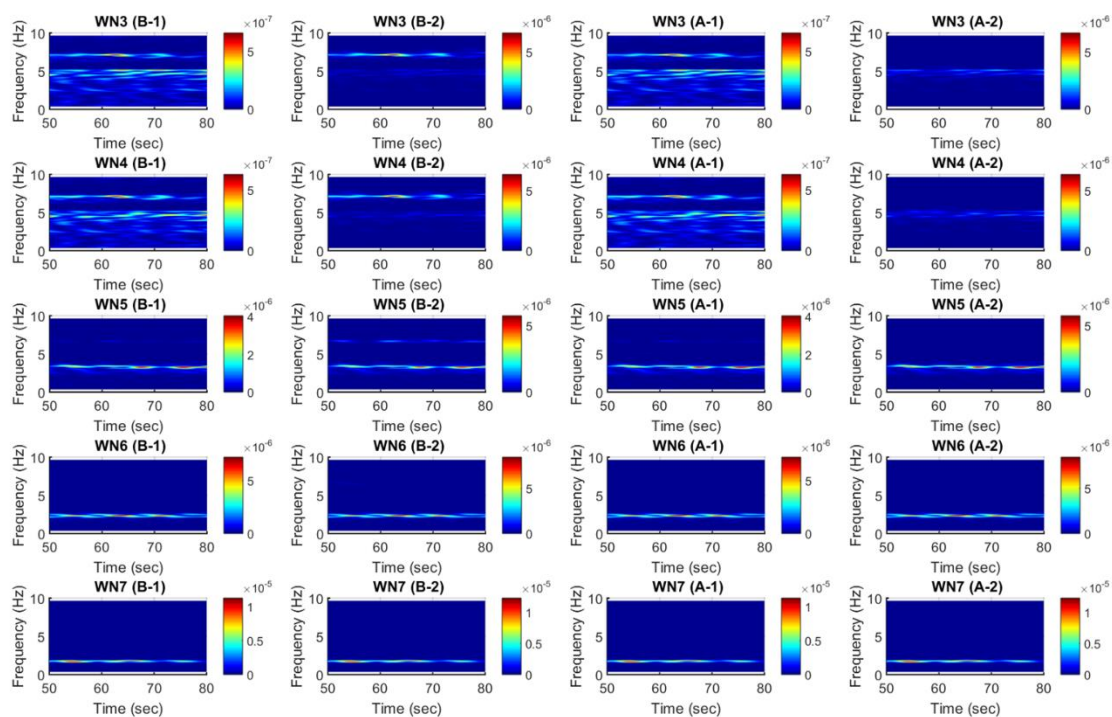
Figure 5-20 The pseudo-IF for EV94 (2009/11/05)
(w.r.t. frequency band: 0.5~6 Hz for both directions)

Appendix I

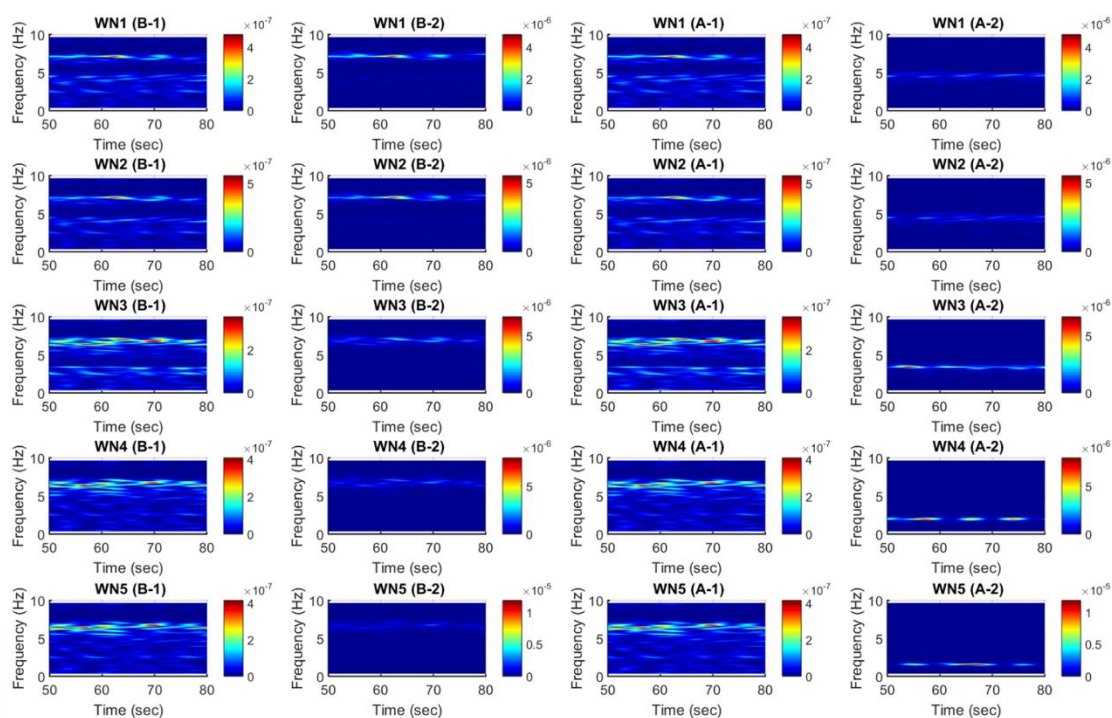


The scalograms of White Noise responses for twin-tower steel structure

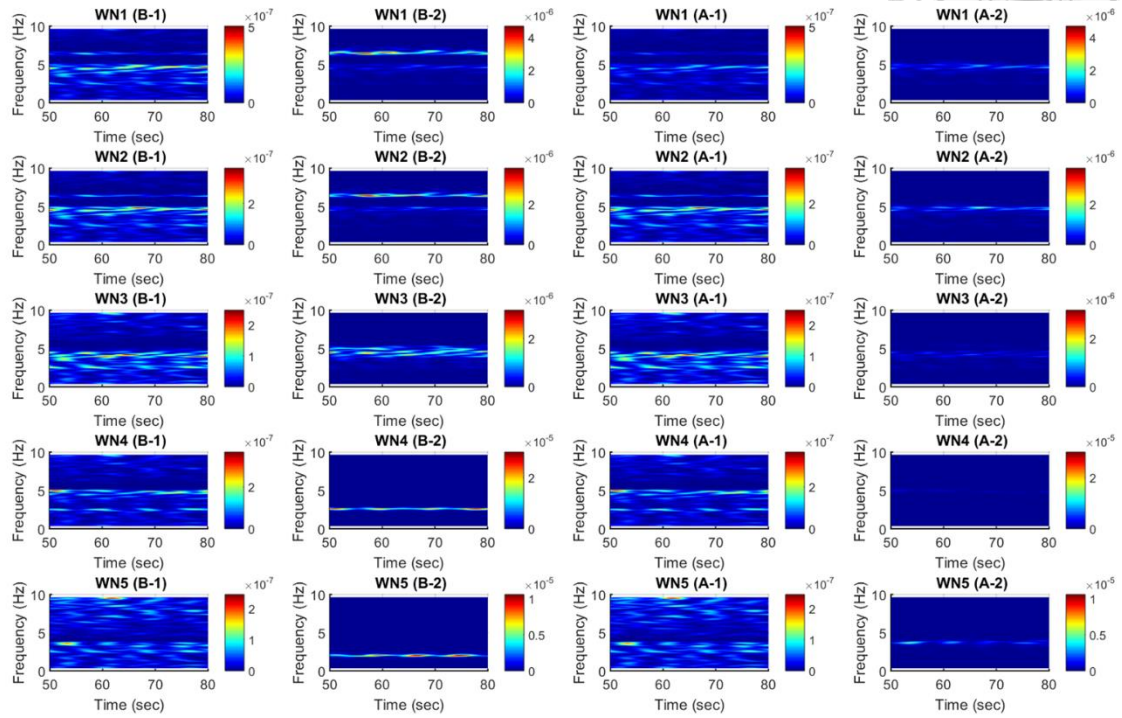
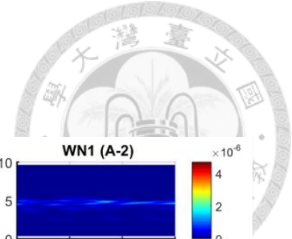
Damage scenario-1



Damage scenario-2

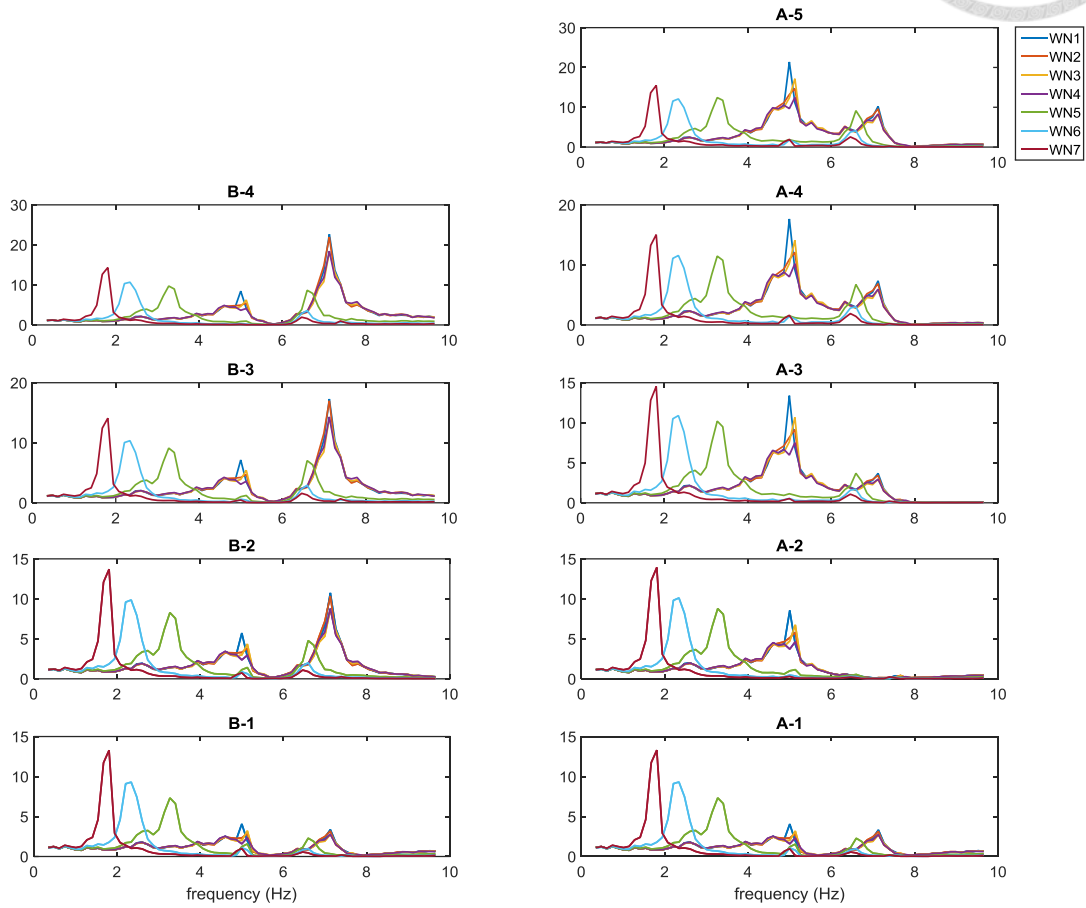


Damage scenario-3

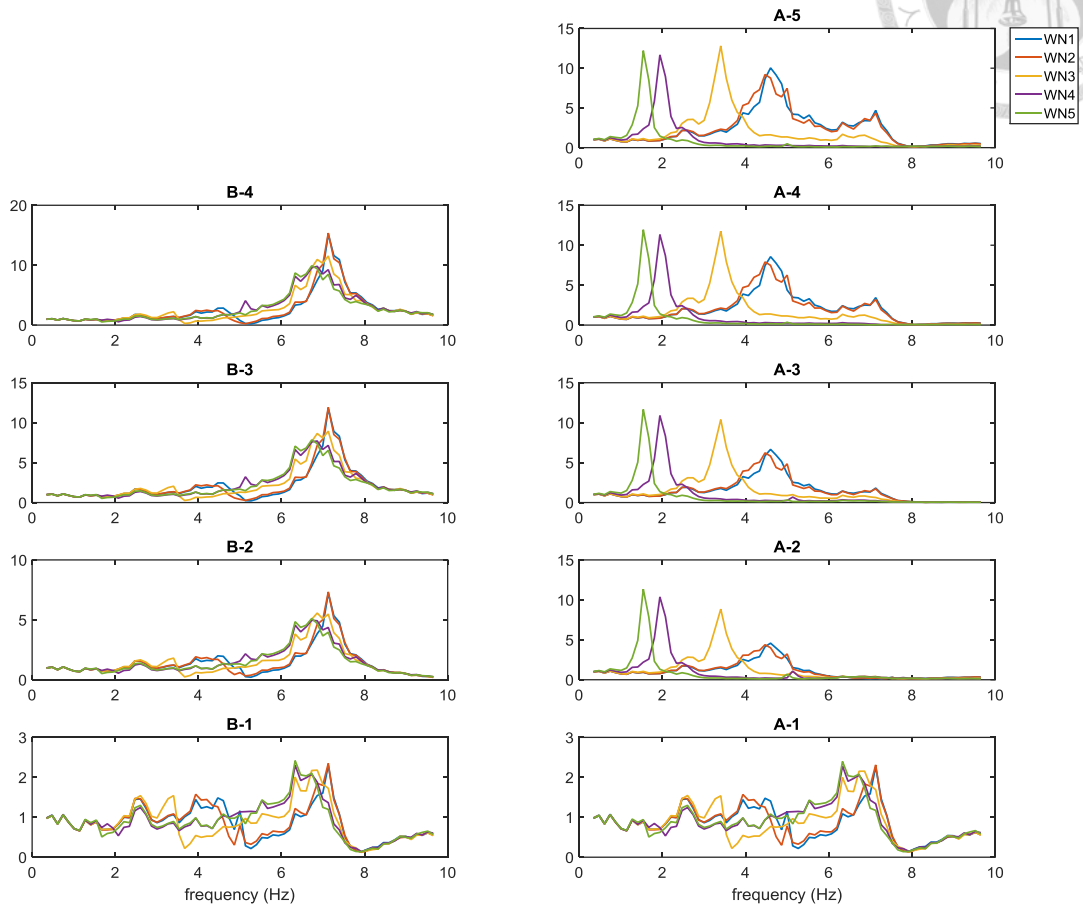
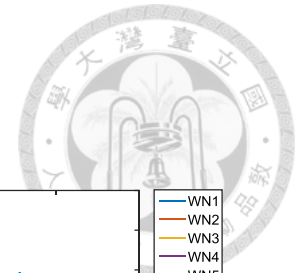


The marginal spectrum of White Noise responses for twin-tower steel structure

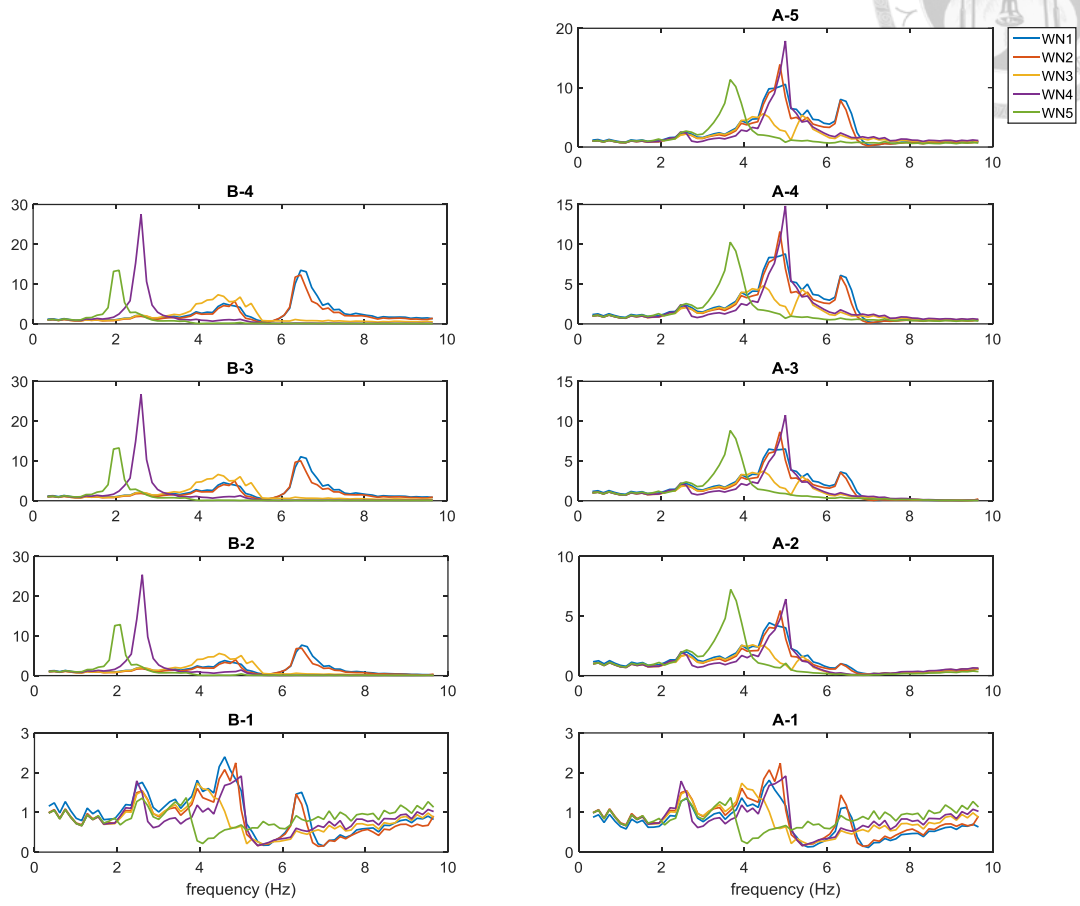
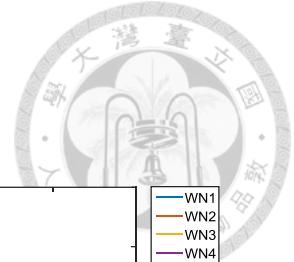
Damage scenario-1



Damage scenario-2



Damage scenario-3



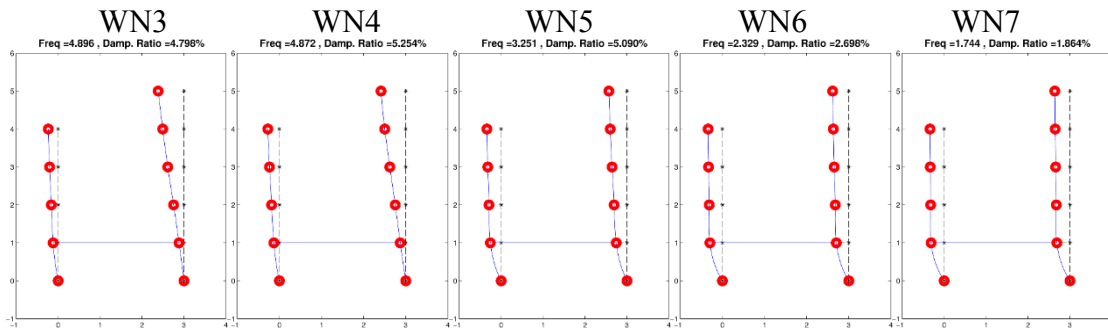
The mode shape of White Noise responses using Automated SSI-COV

for twin-tower steel structure

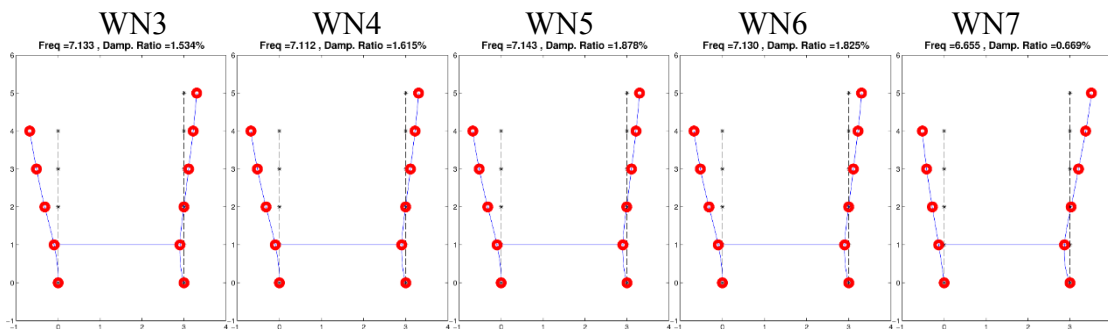


Damage scenario-1

Mode 1:

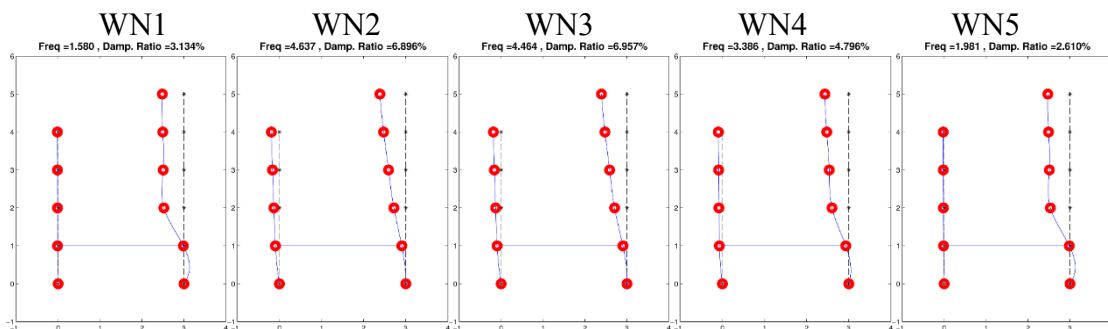


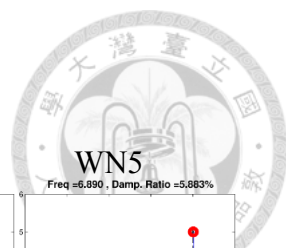
Mode 2:



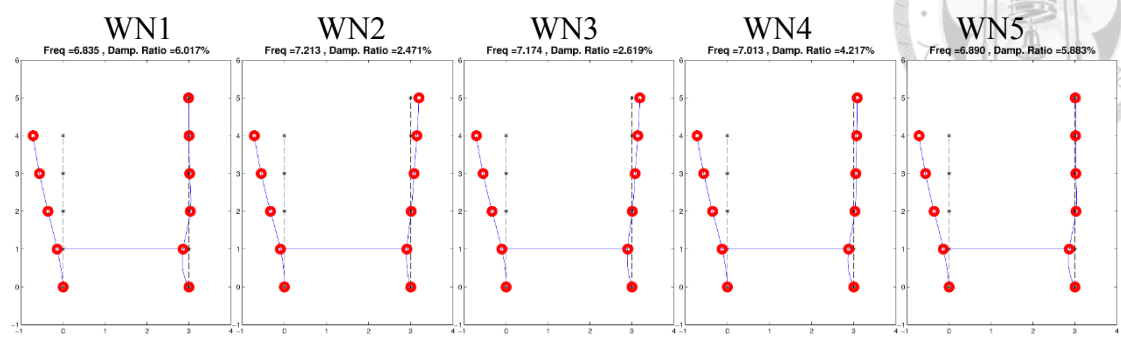
Damage scenario-2

Mode 1:



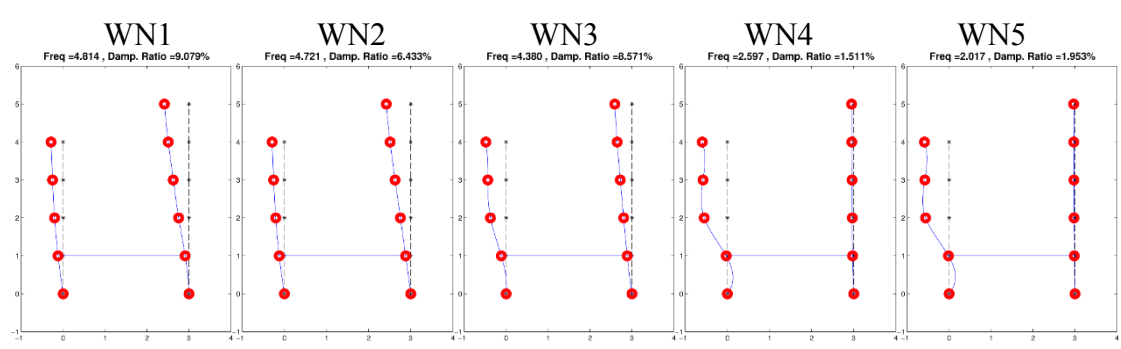


Mode 2:

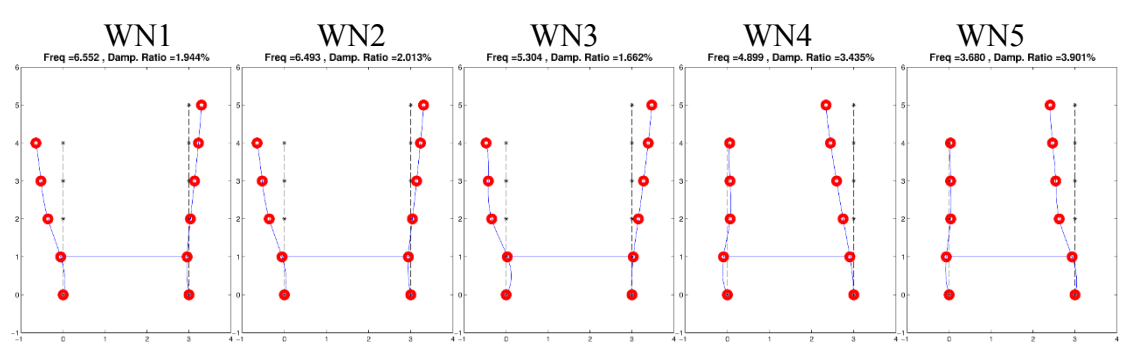


Damage scenario-3

Mode 1:



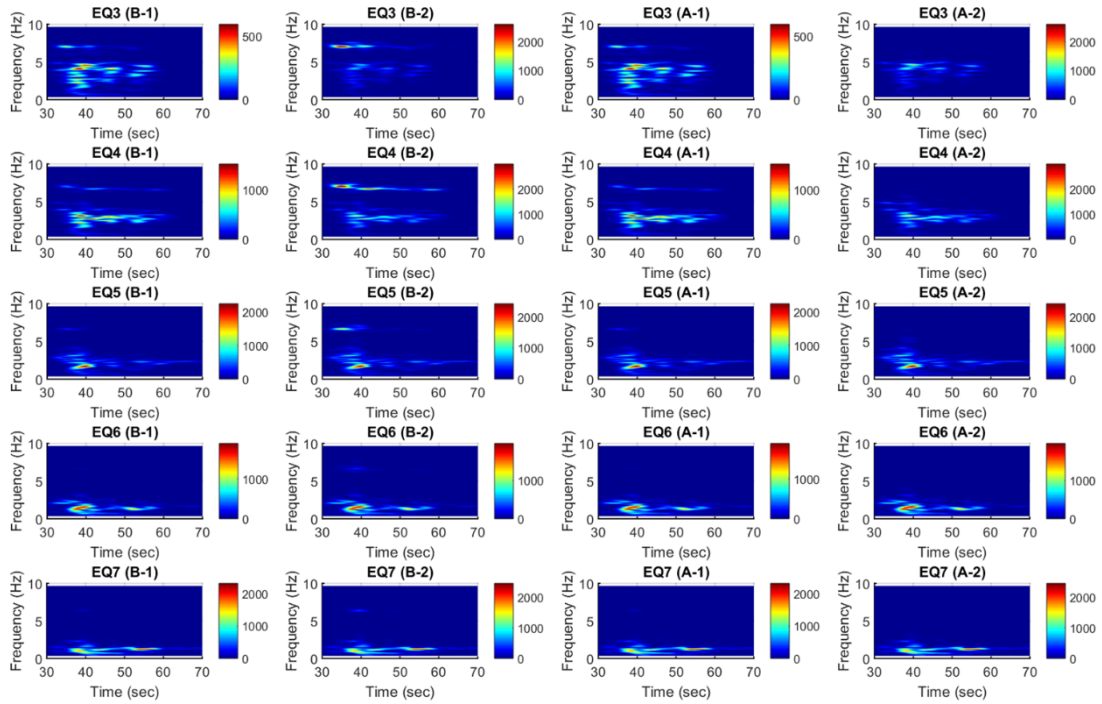
Mode 2:



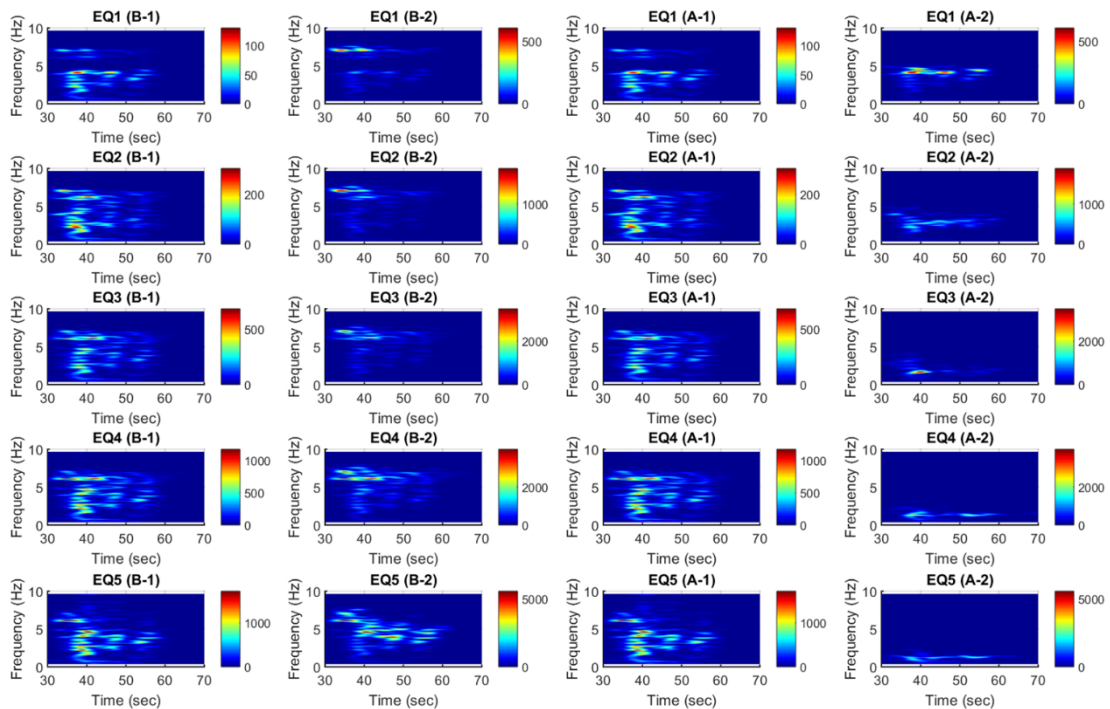
The scalograms of earthquake excitation responses for twin-tower steel structure



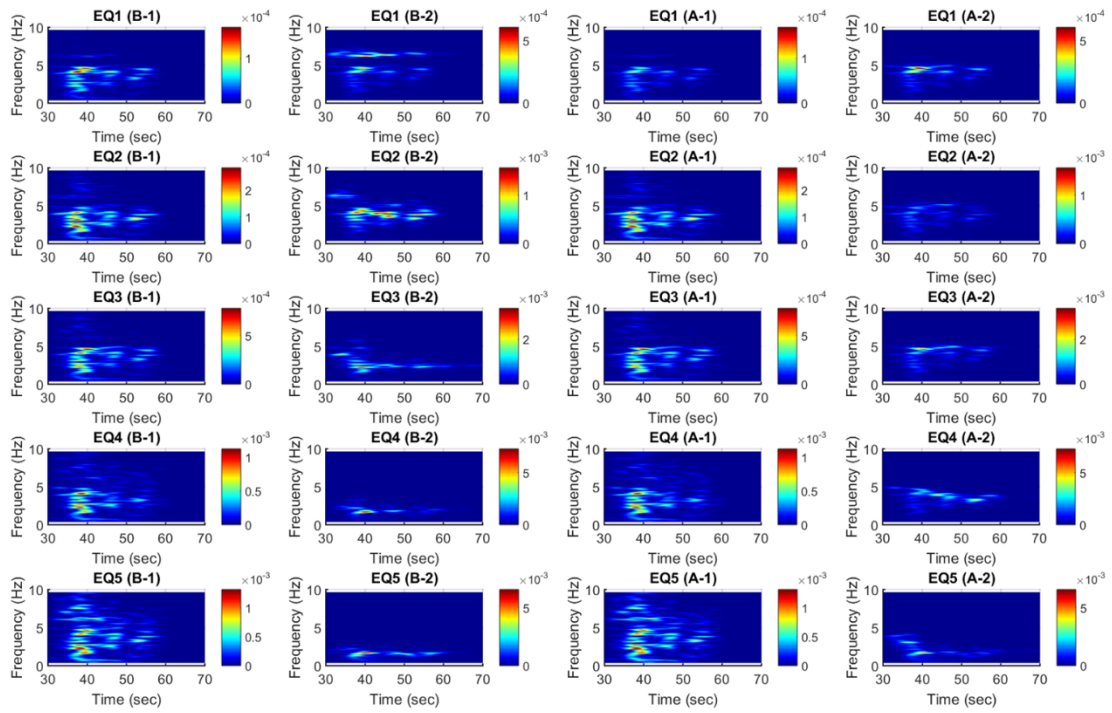
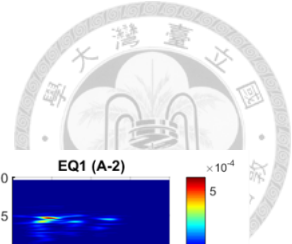
Damage scenario-1



Damage scenario-2



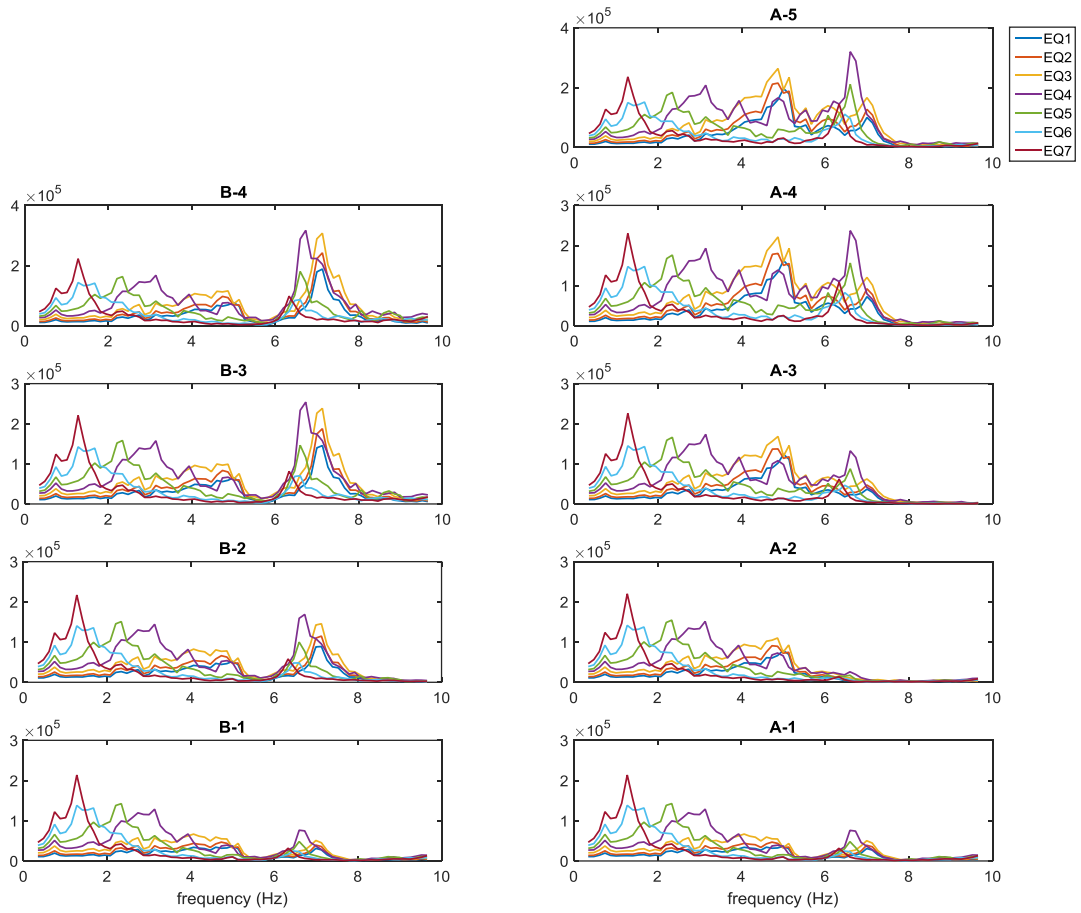
Damage scenario-3



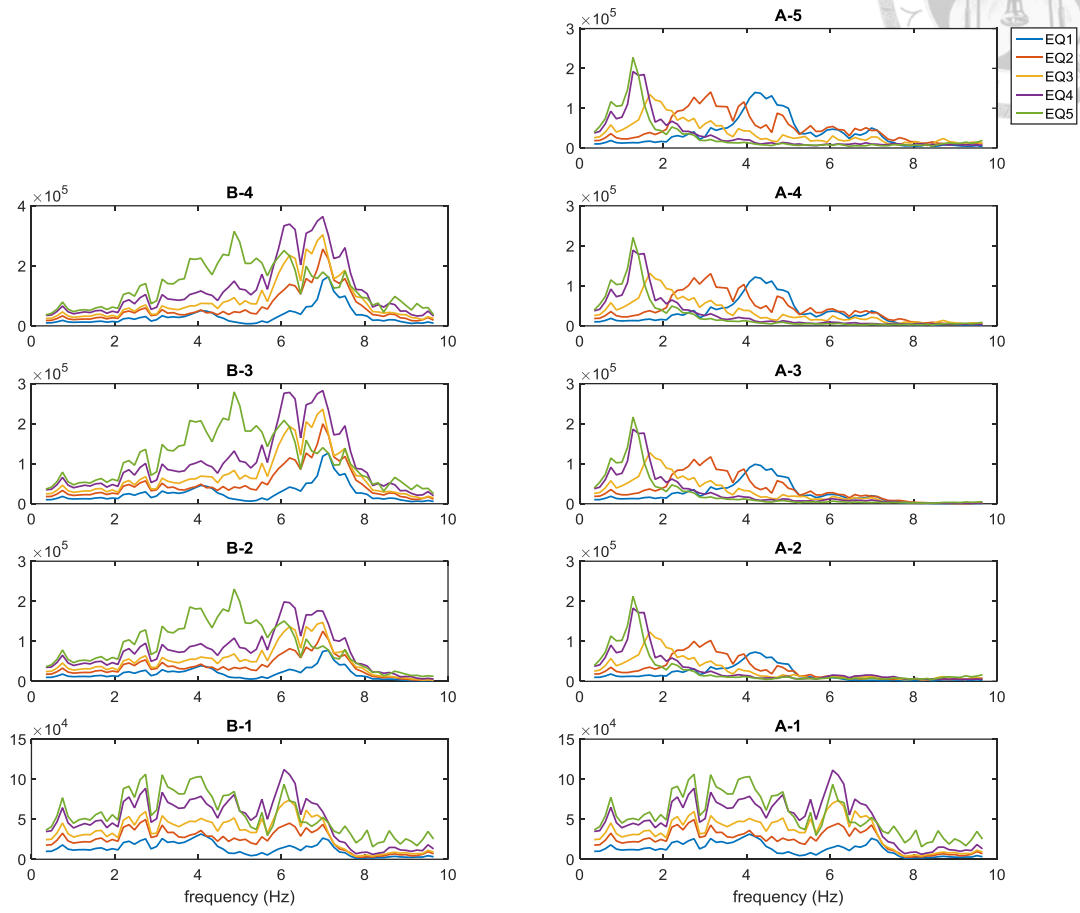
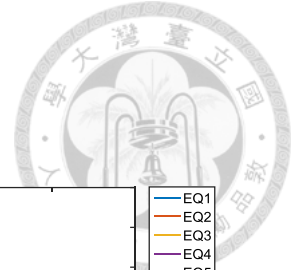
The marginal spectrum of earthquake excitation responses
for twin-tower steel structure



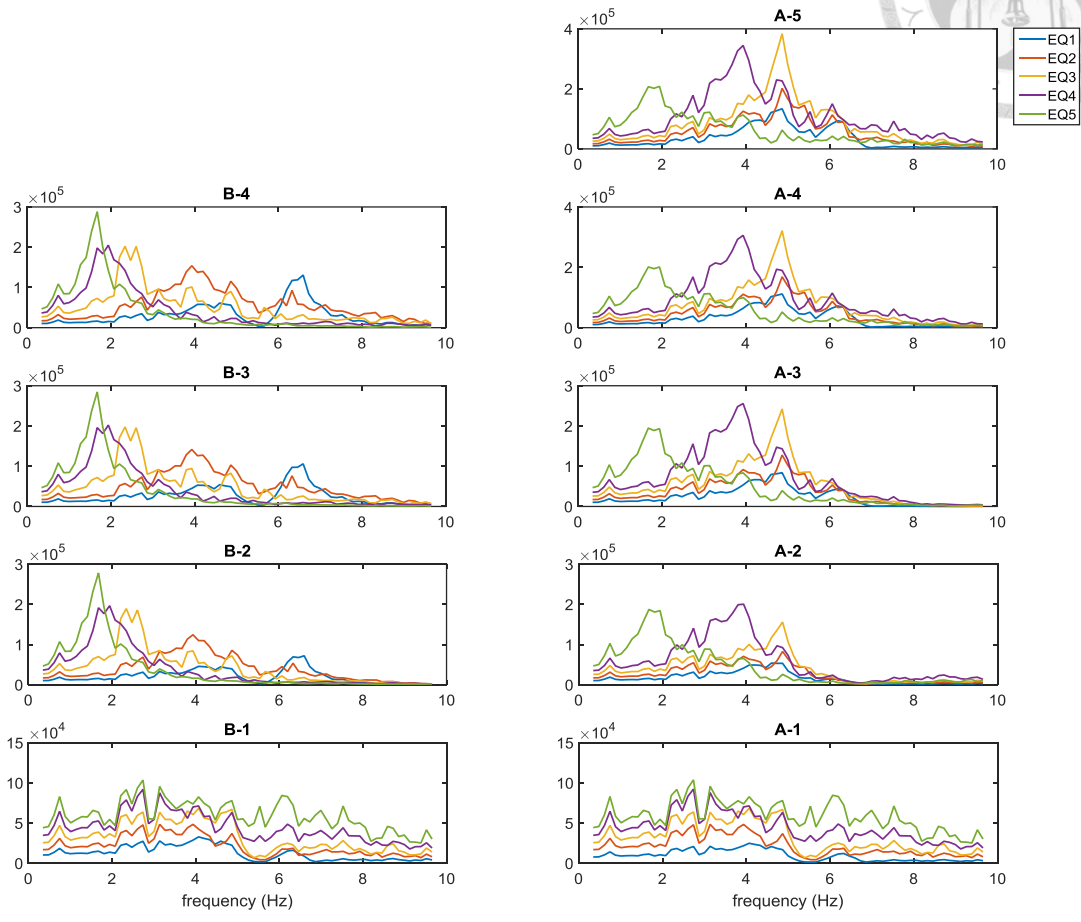
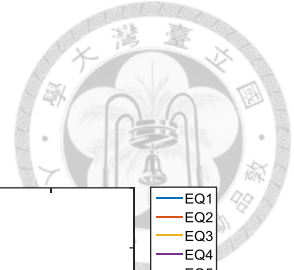
Damage scenario-1



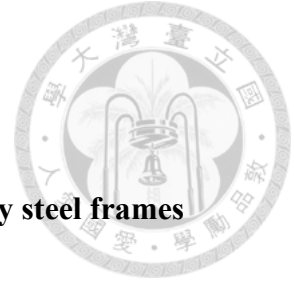
Damage scenario-2



Damage scenario-3

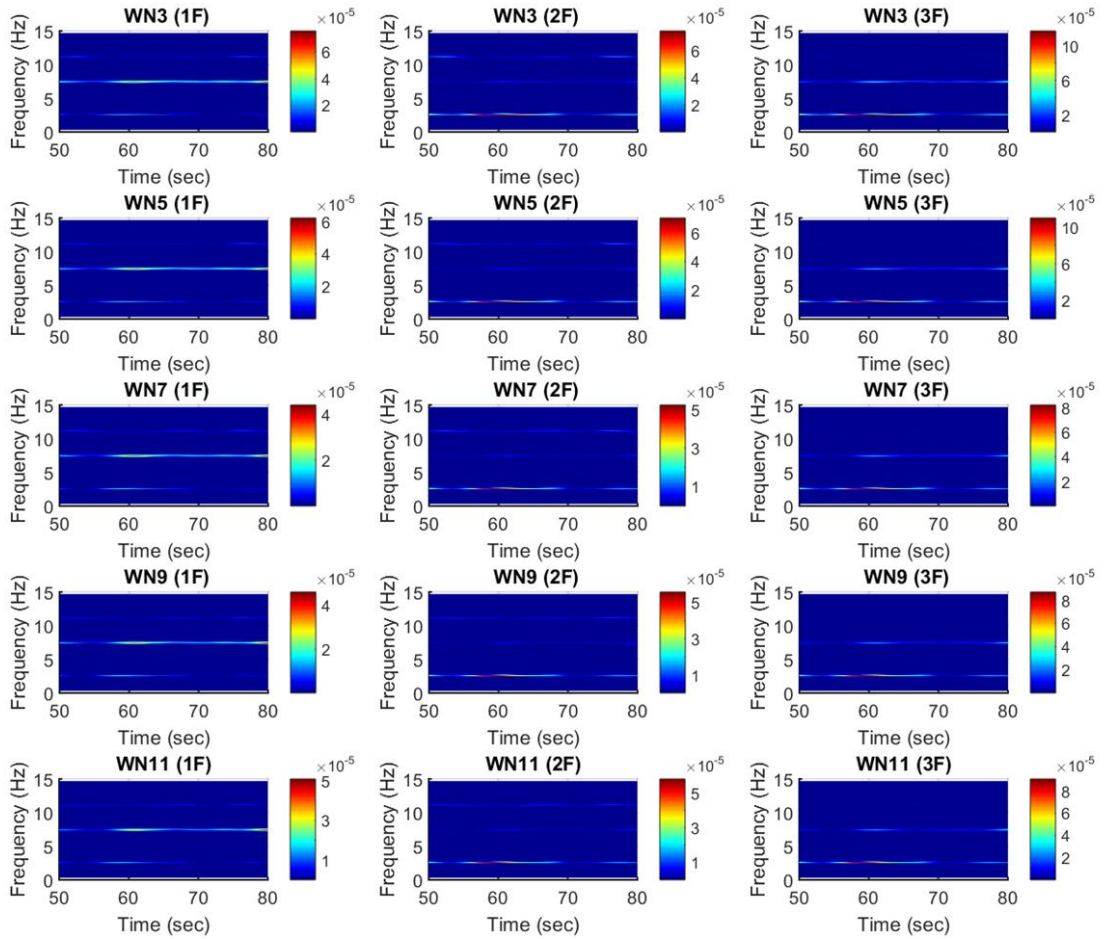


Appendix II

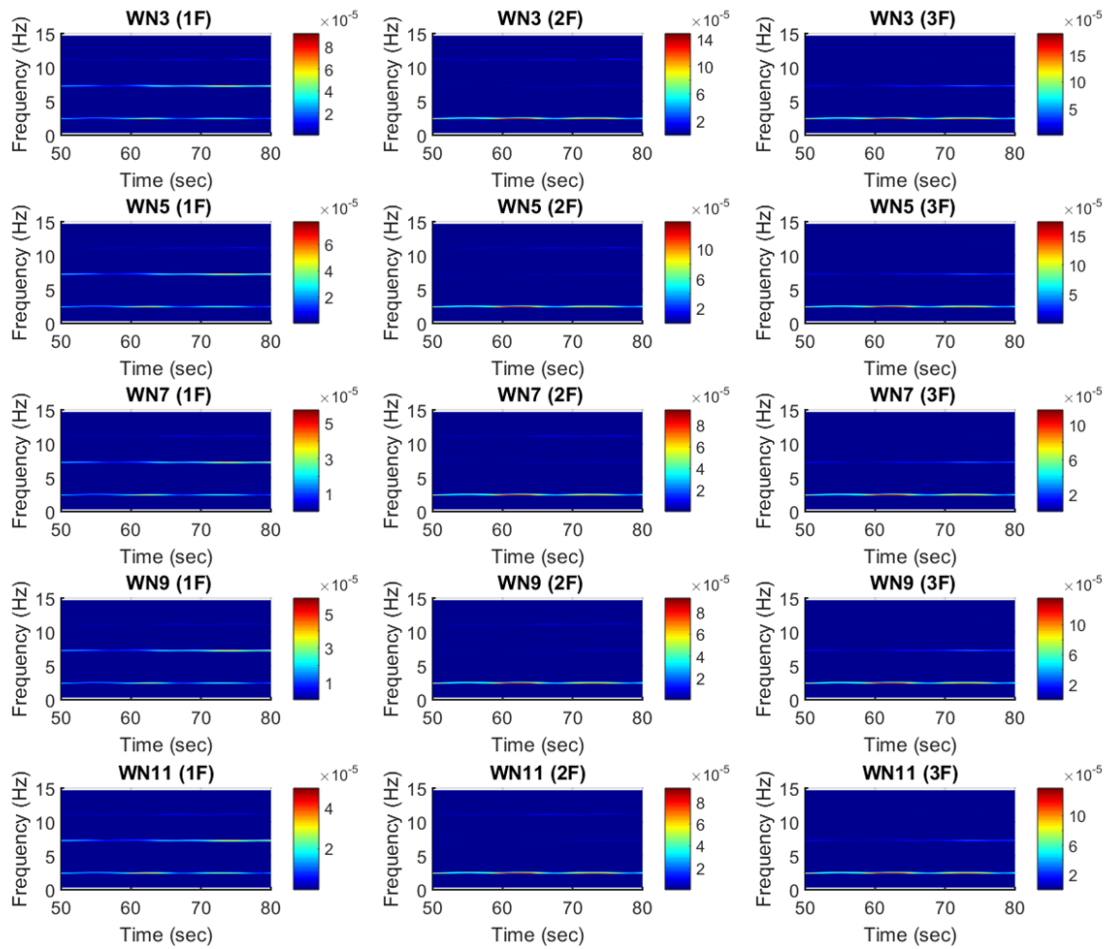
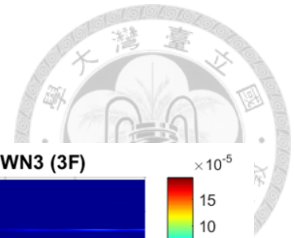


The scalograms of White Noise responses for two three-story steel frames

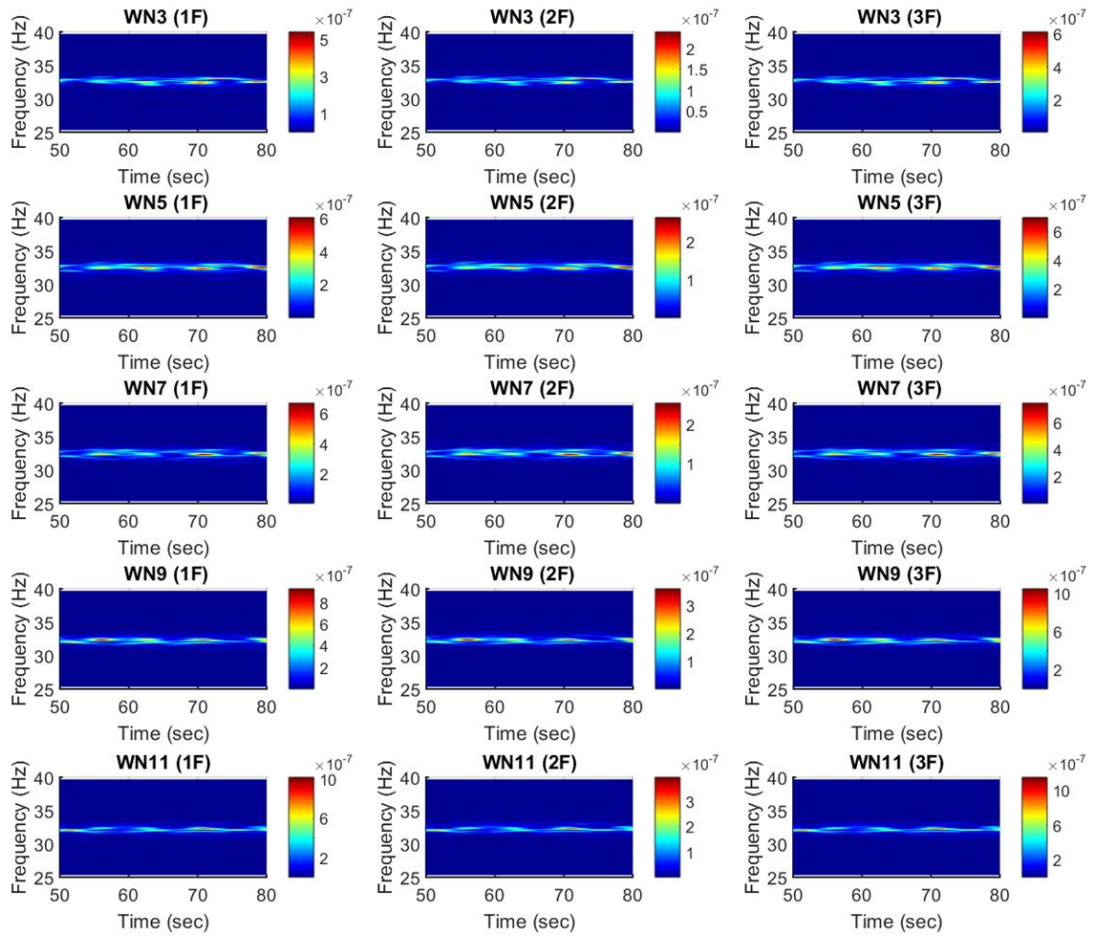
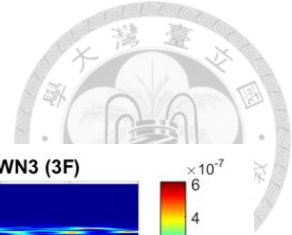
Specimen-1 (x-direction)

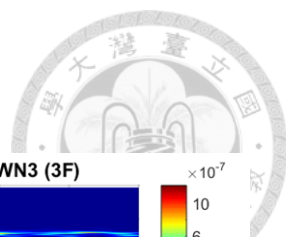


Specimen-2 (x-direction)

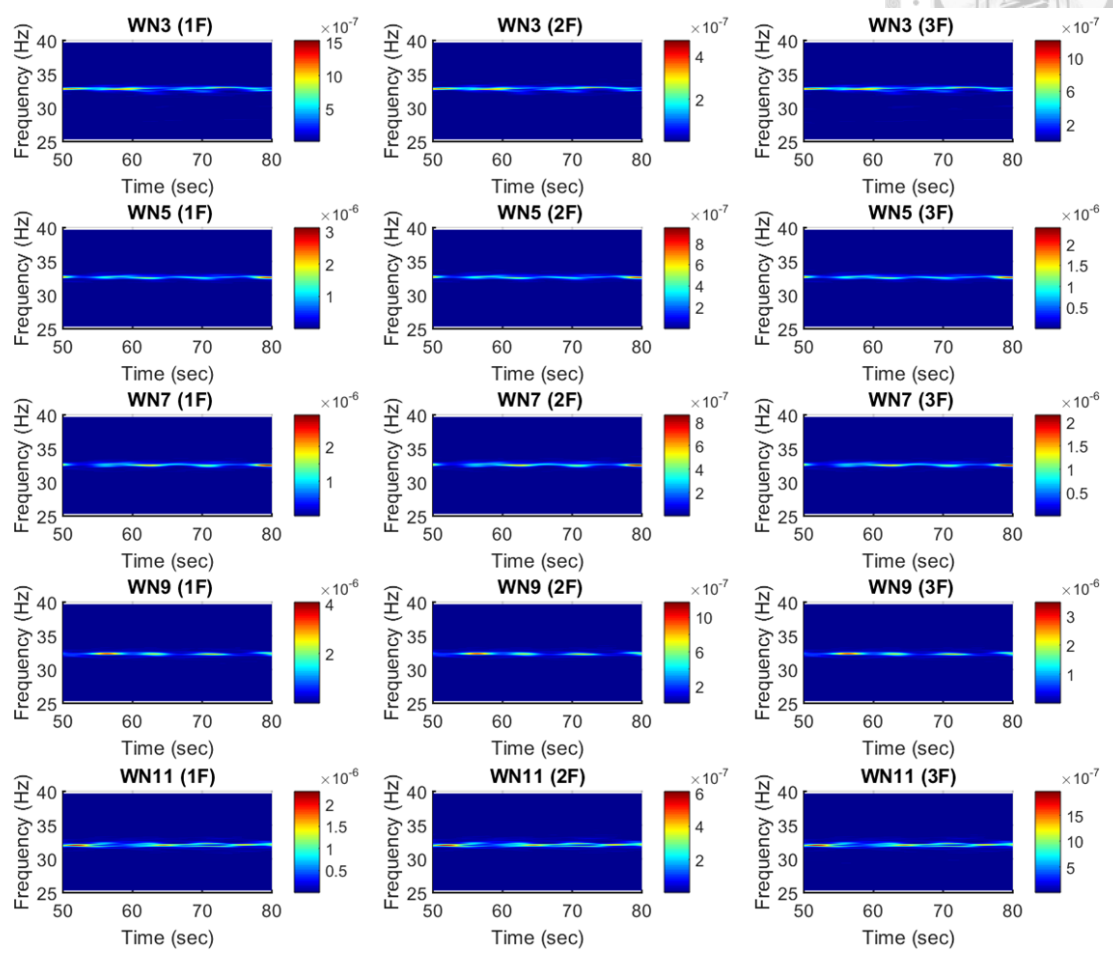


Specimen-1 (torsional direction)





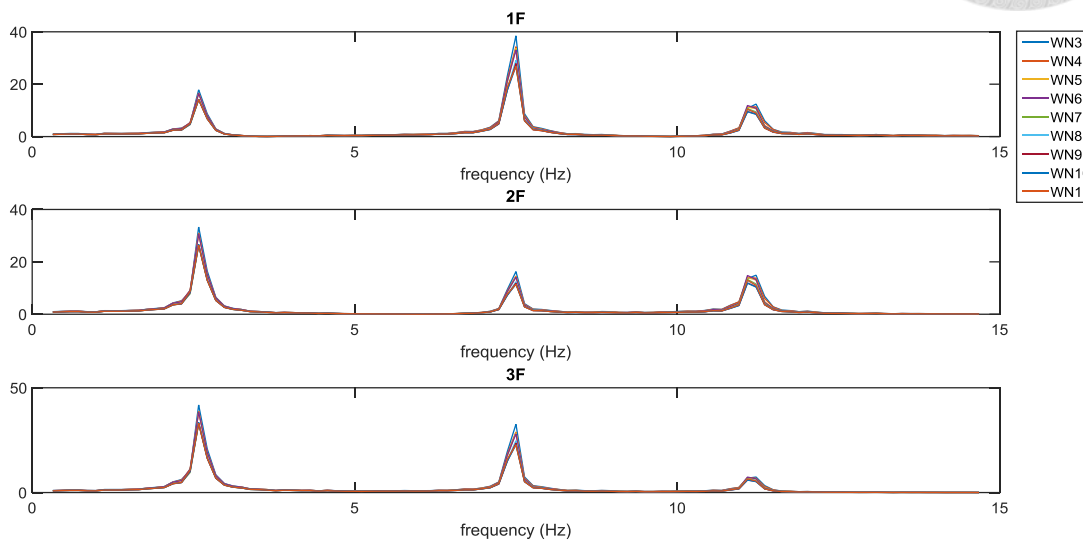
Specimen-2 (torsional direction)



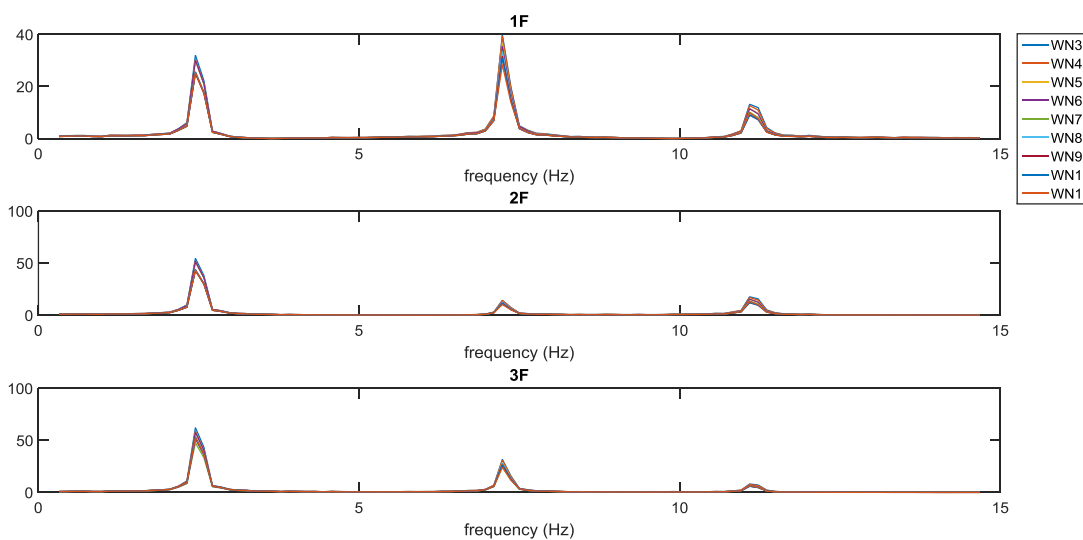


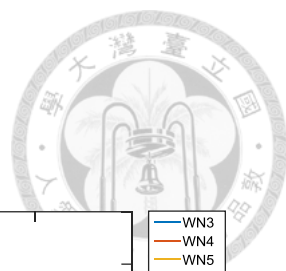
The marginal spectrum of White Noise responses for two three-story steel frames

Specimen-1 (x-direction)

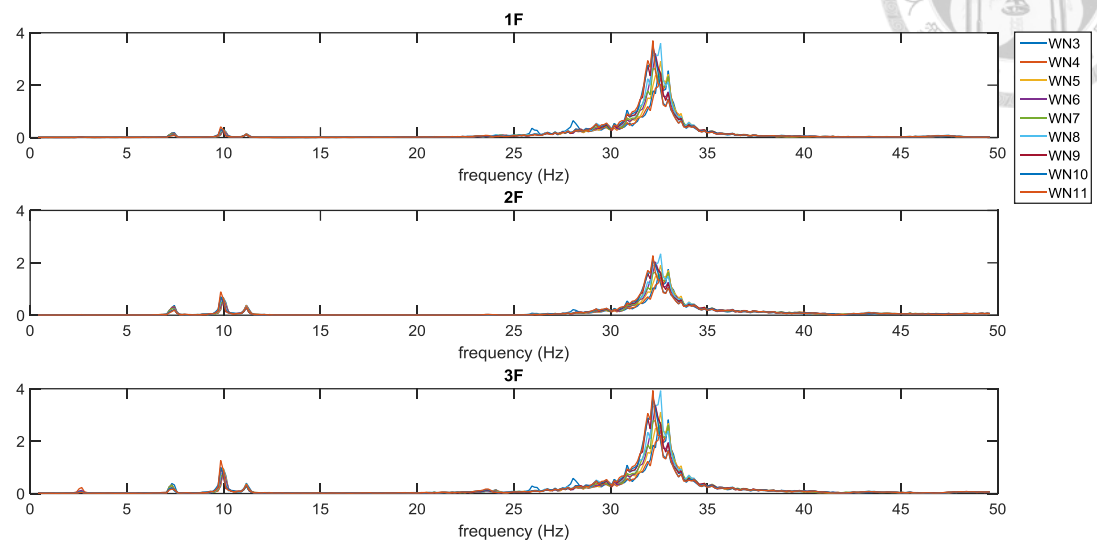


Specimen-2 (x-direction)

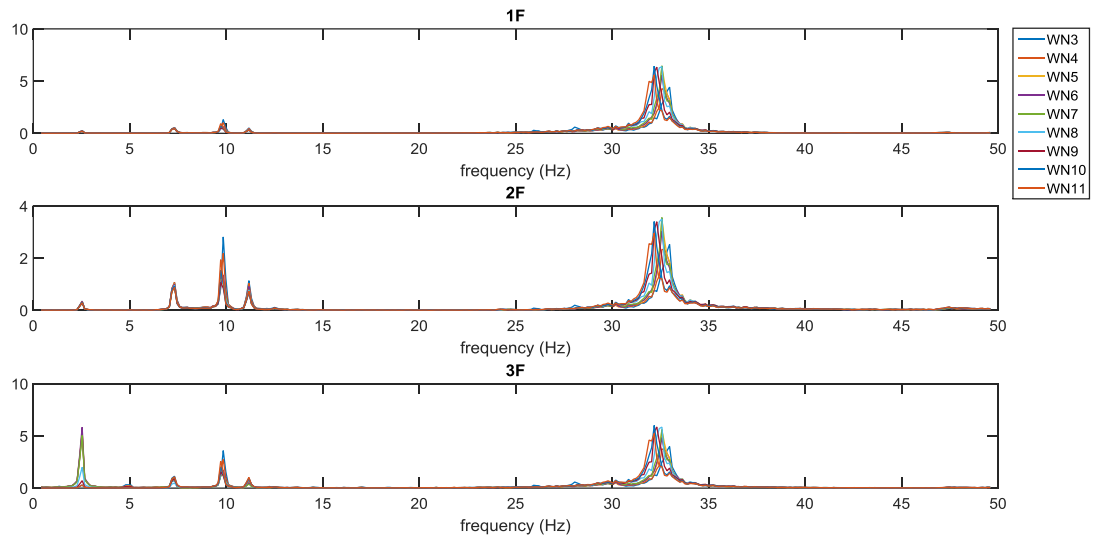


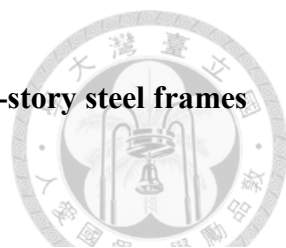


Specimen-1 (torsional direction)



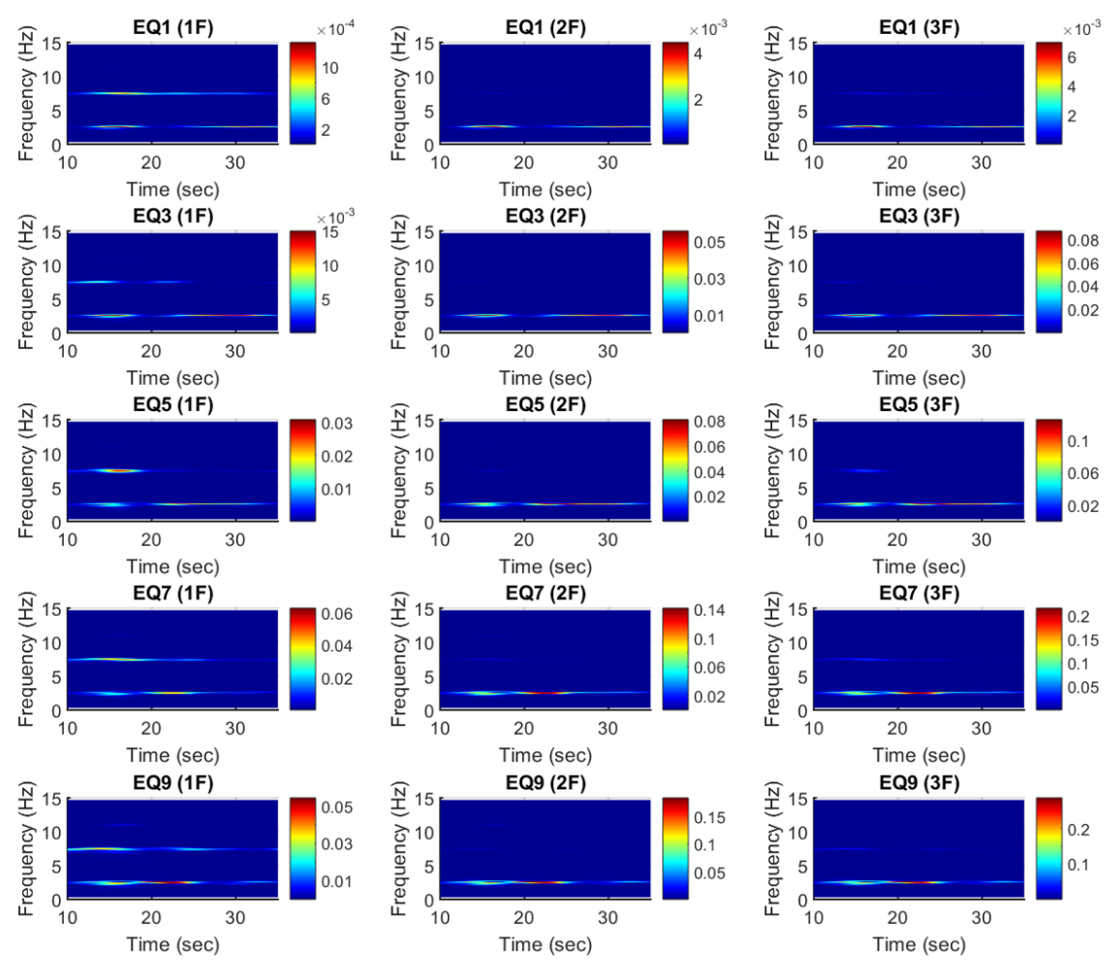
Specimen-2 (torsional direction)



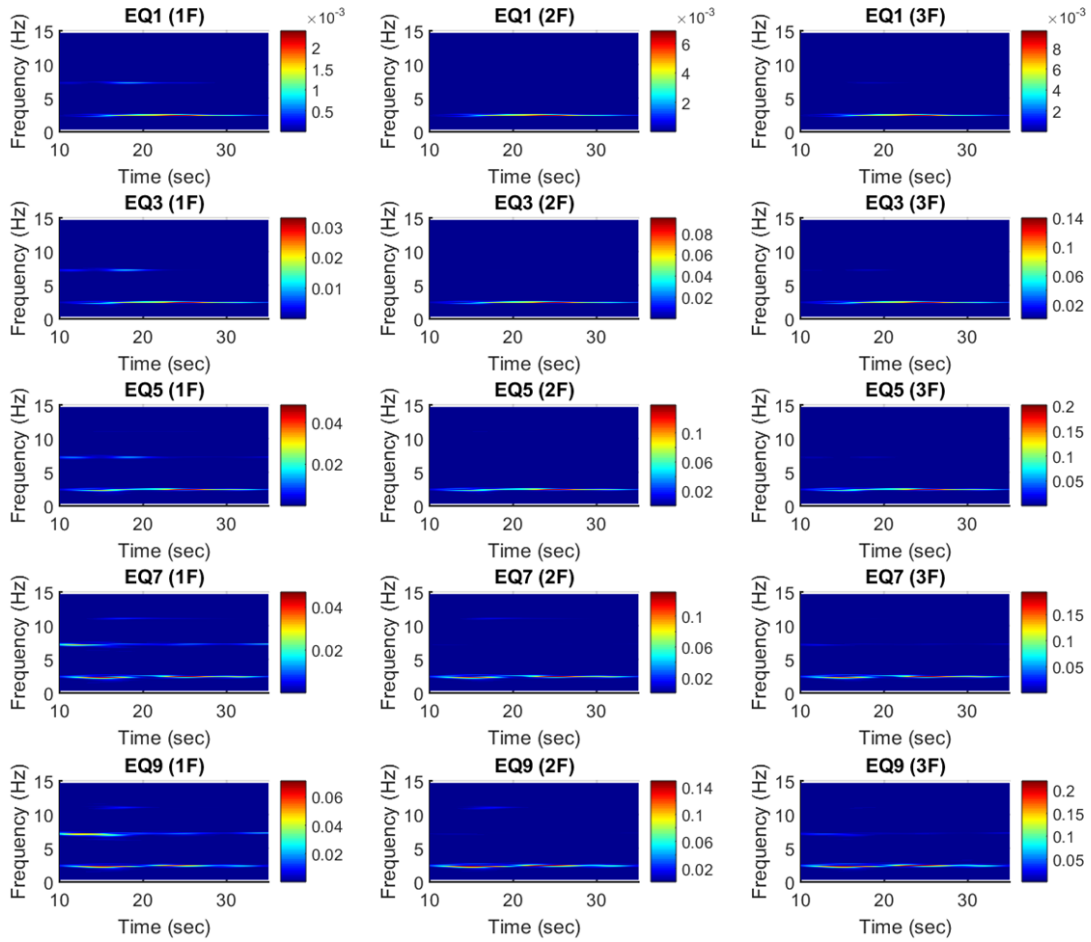
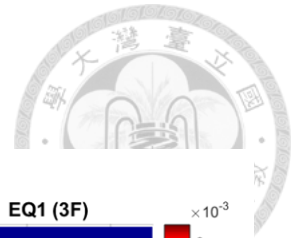


The scalograms of earthquake excitation responses for two three-story steel frames

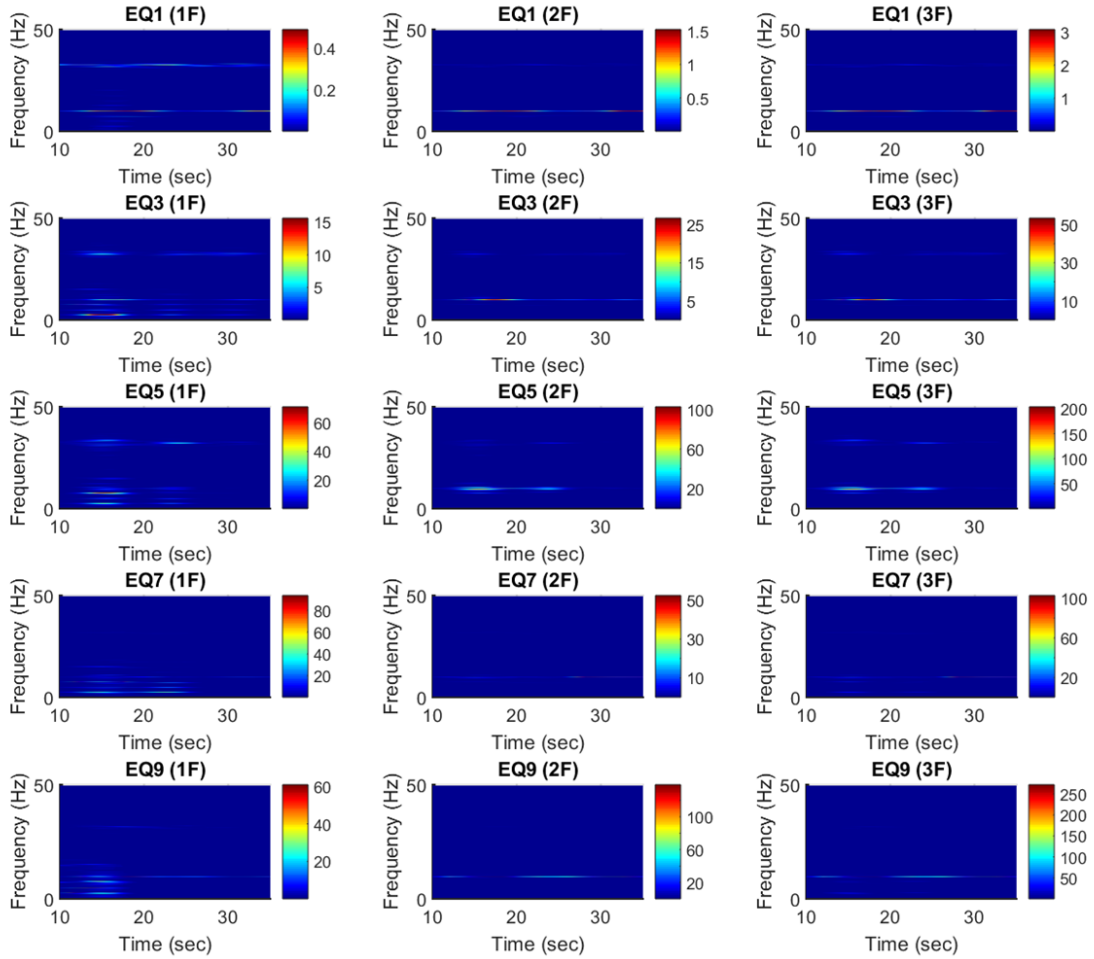
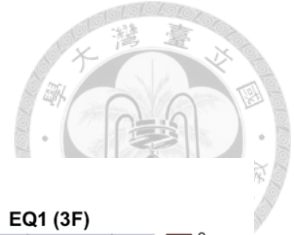
Specimen-1 (x-direction)



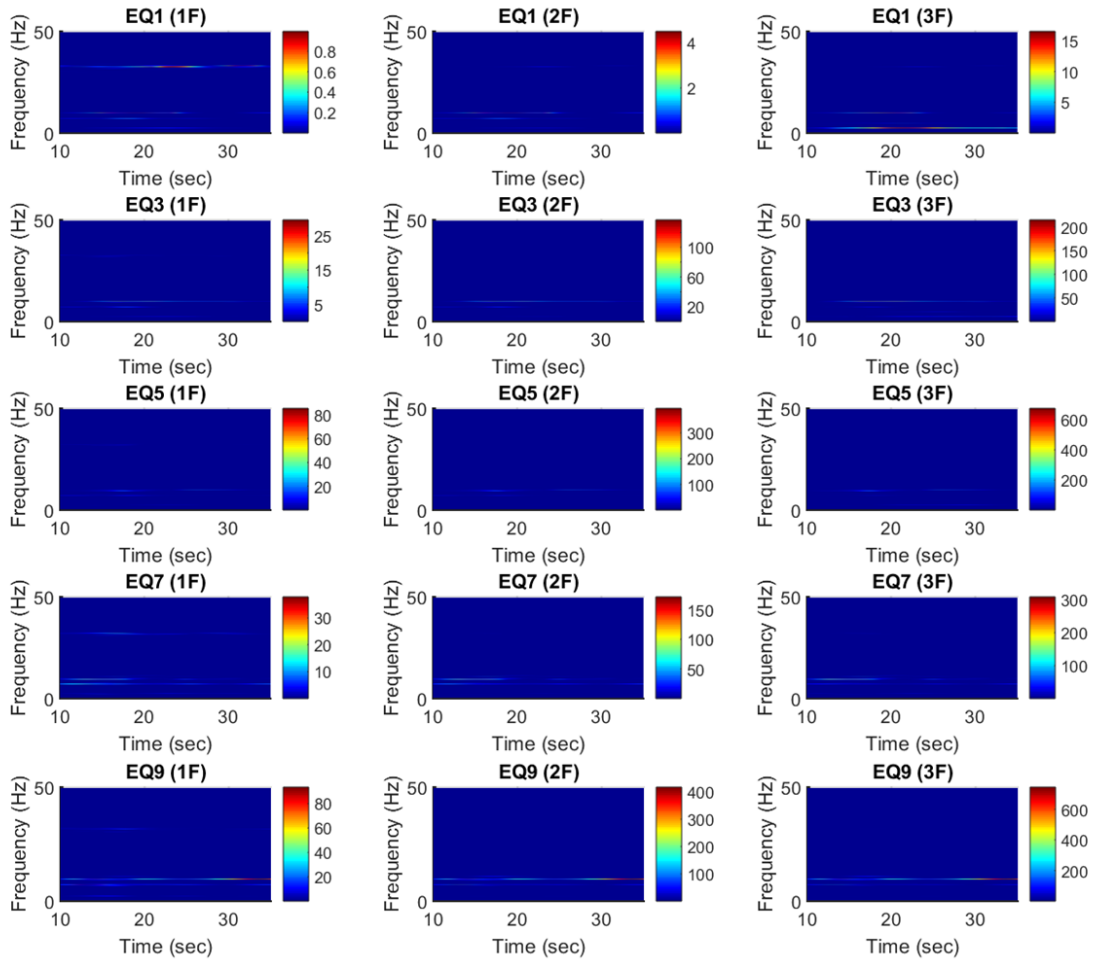
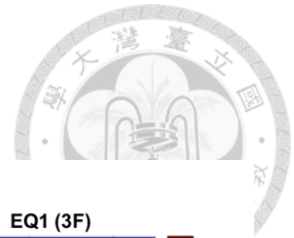
Specimen-2 (x-direction)



Specimen-1 (torsional direction)



Specimen-2 (torsional direction)

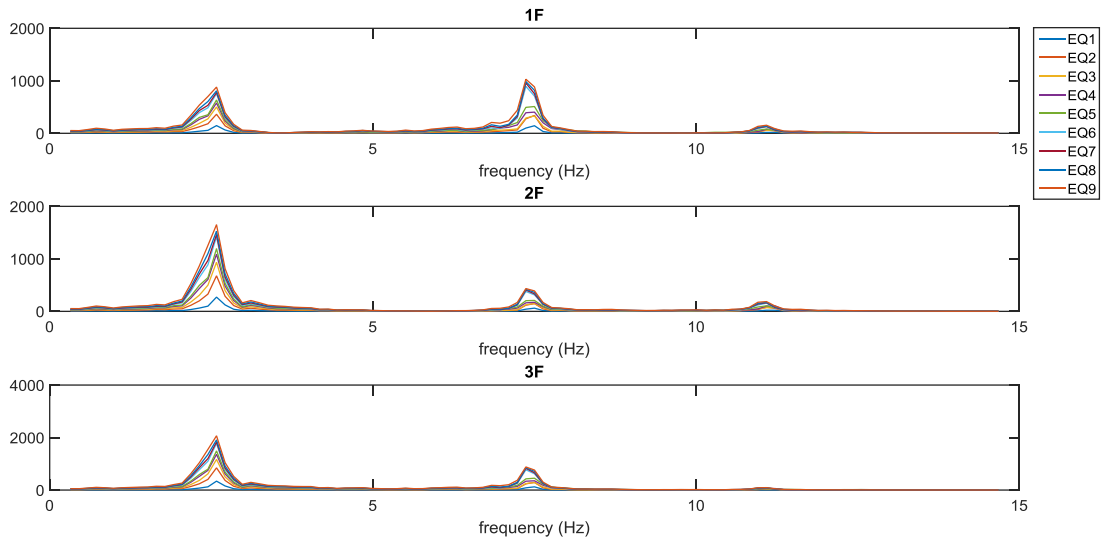


The marginal spectrum of earthquake excitation responses

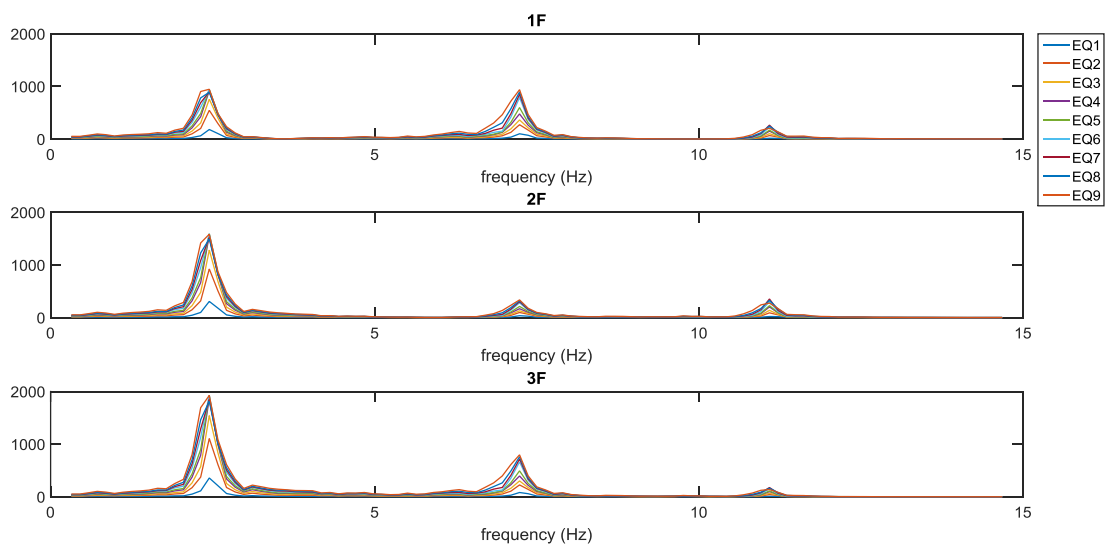
for two three-story steel frames

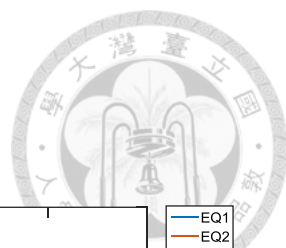


Specimen-1 (x-direction)

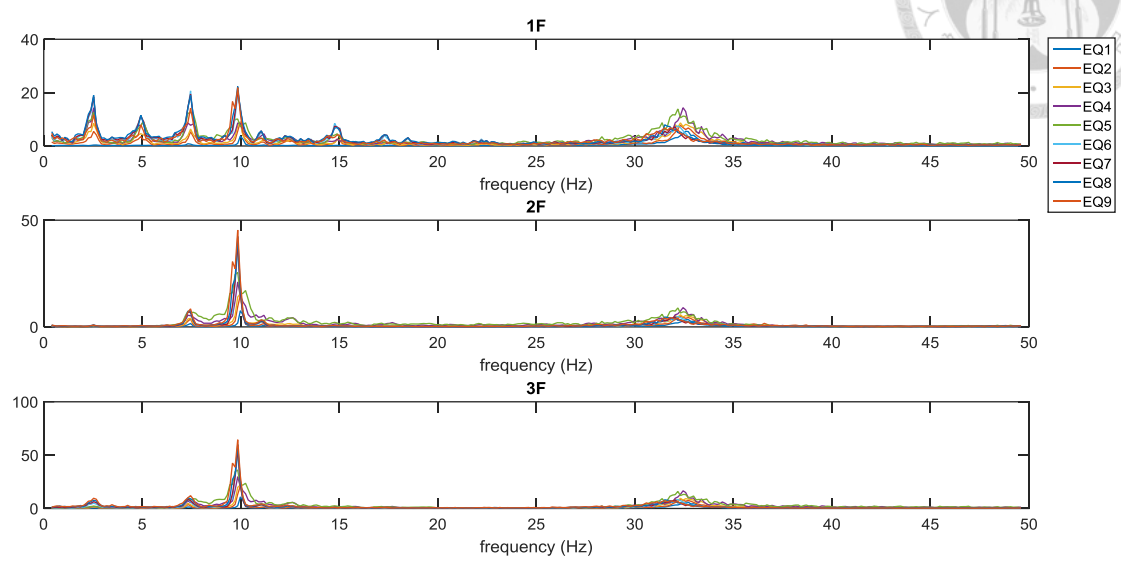


Specimen-2 (x-direction)

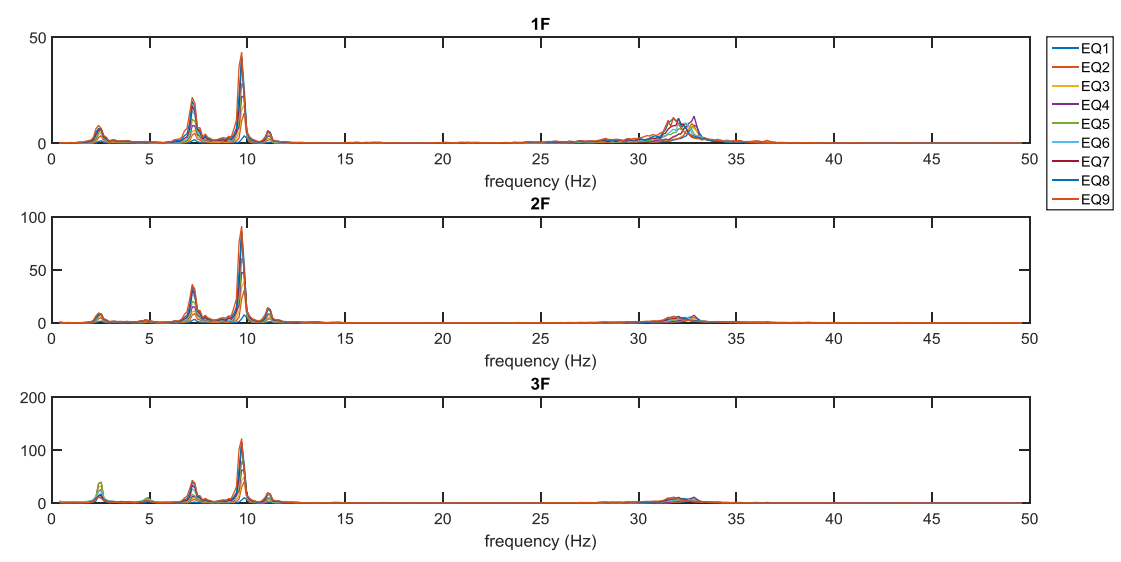




Specimen-1 (torsional direction)



Specimen-2 (torsional direction)

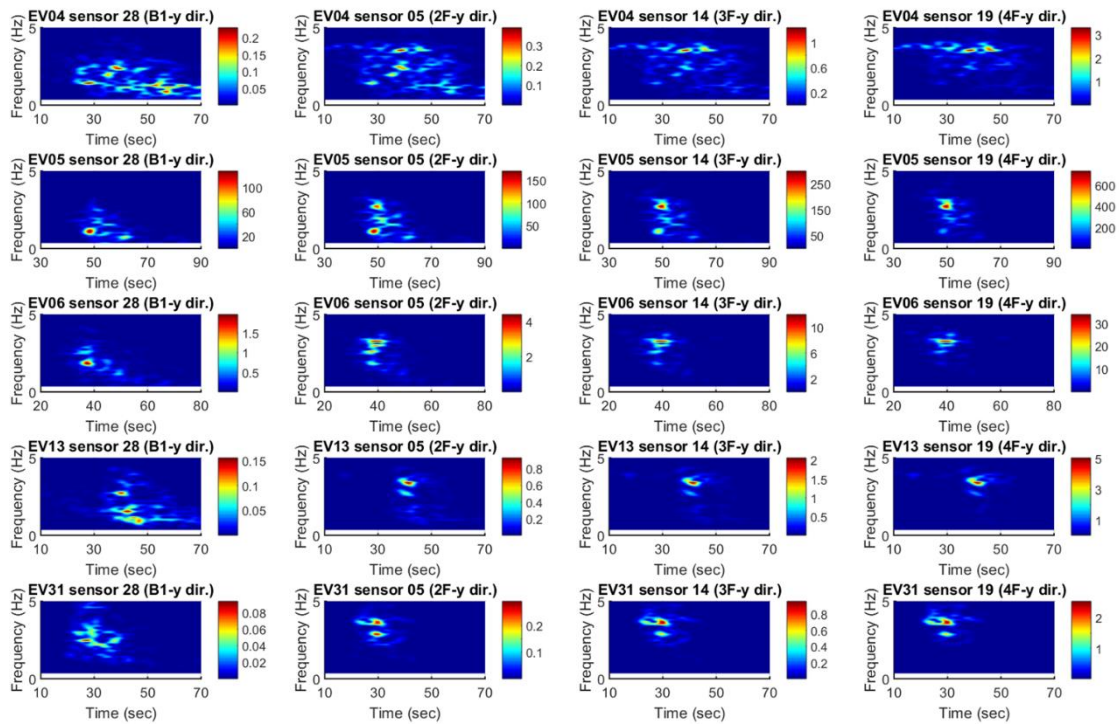


Appendix III

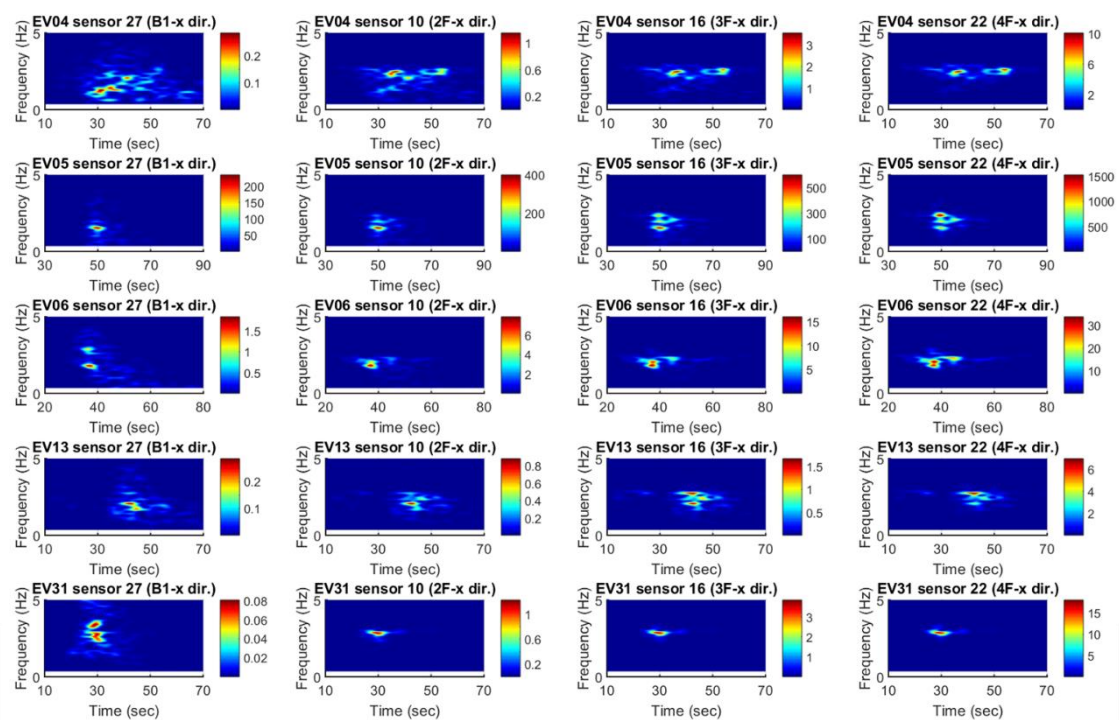


The scalograms of earthquake excitation responses for Mingli Elementary School

Y-direction



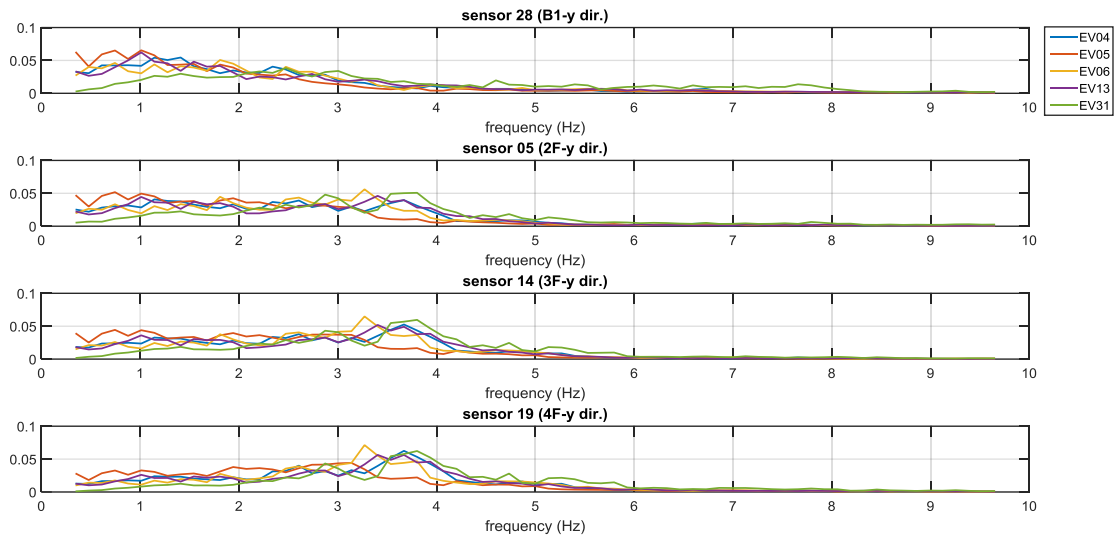
X-direction



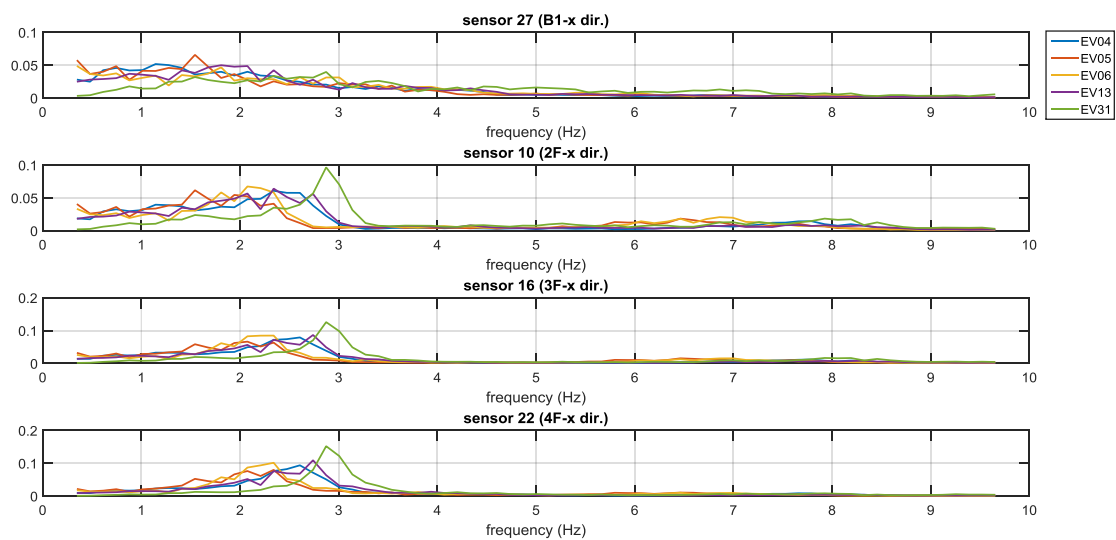
The marginal spectrum of earthquake excitation responses for Mingli Elementary School



Y-direction



X-direction



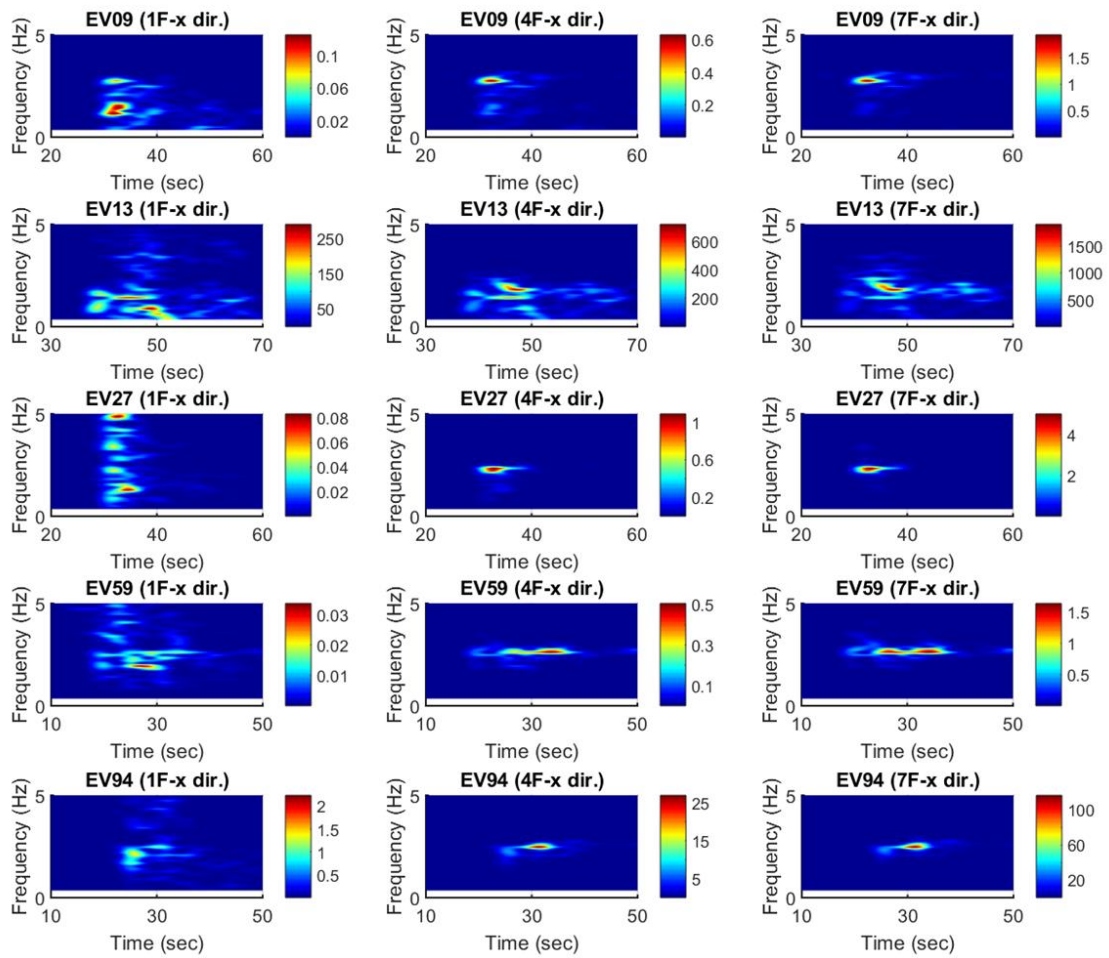
Appendix III



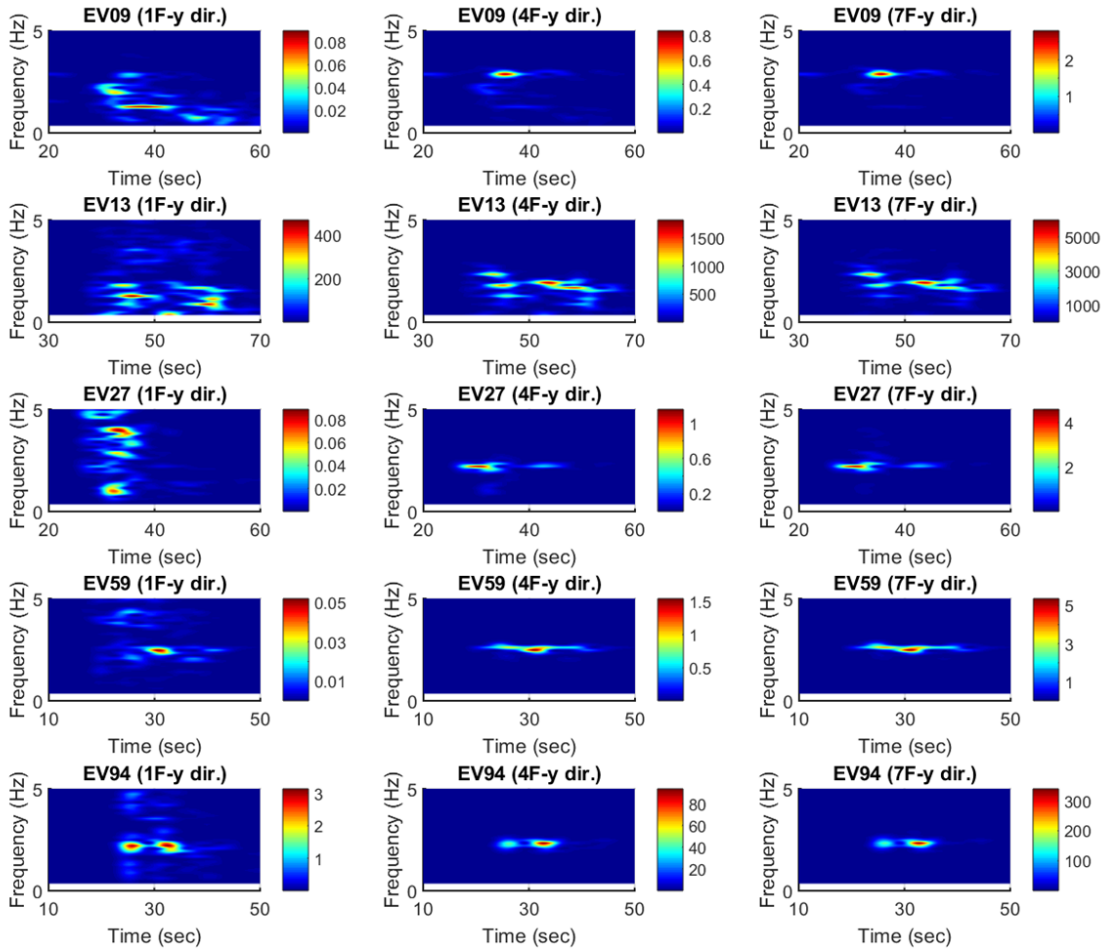
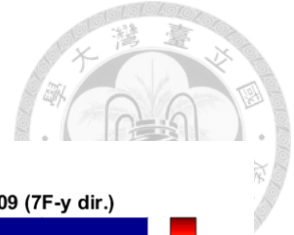
The scalograms of earthquake excitation responses

for NCHU Civil & Environmental Engineering Building

X-direction



Y-direction

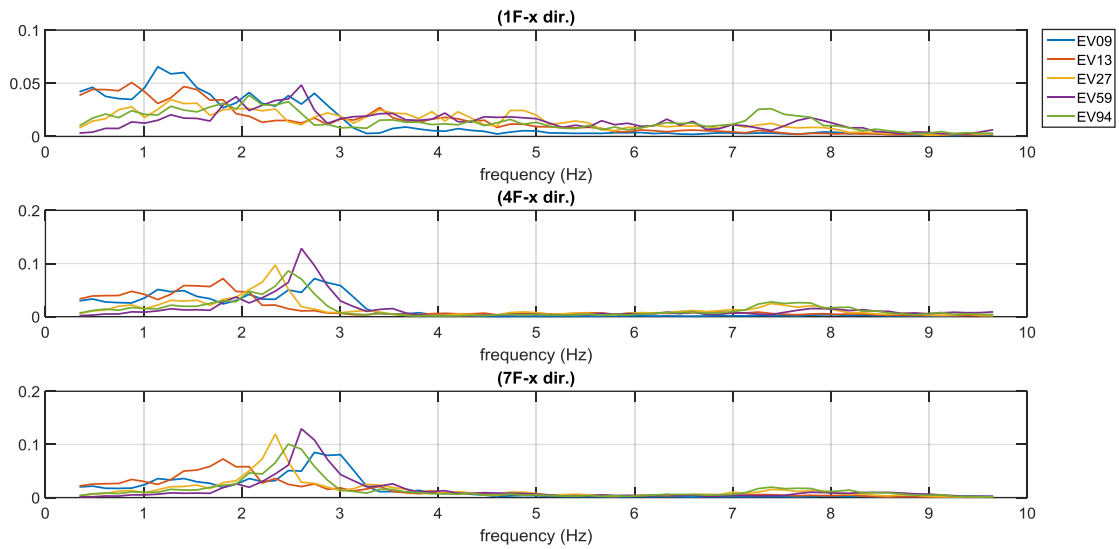


The marginal spectrum of earthquake excitation responses

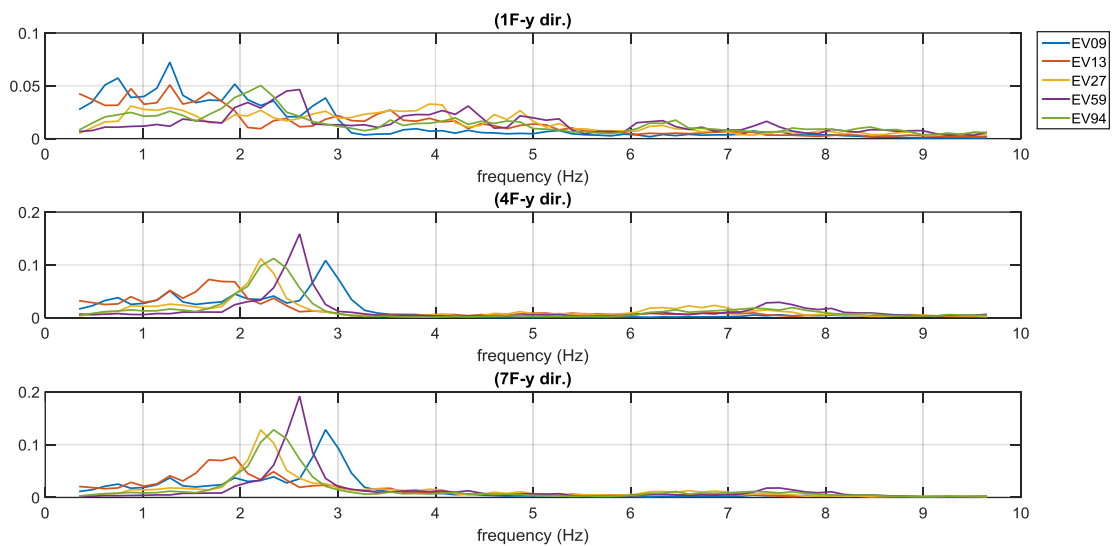
for NCHU Civil & Environmental Engineering Building



X-direction



Y-direction



簡 歷



姓名：薛 汶

籍貫：台灣 台北市

生日：1993/05/30

電子信箱：r04521225@ntu.edu.tw

學歷：

國立臺灣大學土木工程學系結構工程組 (2015.09~2017.06)

國立交通大學土木工程學系 (2011.09~2015.06)

台北市立松山高級中學 (2008.09~2011.06)

台北市立興雅國民中學 (2005.09~2008.06)

台北市立興雅國民小學 (1999.09~2005.06)